DEVELOPMENT OF A MONTE CARLO TREATMENT PLANNING AND DOSIMETRY SYSTEM FOR SMALL ANIMAL IRRADIATOR

APPROVED BY SUPERVISORY COMMITTEE

.

Timothy Solberg, PhD

Strahinja Stojadinovic, PhD

Jon Anderson, PhD

Ryan Foster, PhD

Paul Medin, PhD

DEDICATION

To my parents

(Dr.P.Rama Krishna Chowdary & P.Saileela)

DEVELOPMENT OF A MONTE CARLO TREATMENT PLANNING AND DOSIMETRY SYSTEM FOR SMALL ANIMAL IRRADIATOR

by

RAHESH PIDIKITI

DISSERTATION

Presented to the Faculty of the Graduate School of Biomedical Sciences

The University of Texas Southwestern Medical Center at Dallas

In Partial Fulfillment of the Requirements

For the Degree of

DOCTOR OF PHILOSOPHY
The University of Texas Southwestern Medical Center at Dallas

Dallas, Texas

December, 2012

DEVELOPMENT OF A MONTE CARLO TREATMENT PLANNING AND DOSIMETRY SYSTEM FOR SMALL ANIMAL IRRADIATOR

RAJESH PIDIKITI, Ph.D.

The University of Texas Southwestern Medical Center at Dallas, 2012

TIMOTHY SOLBERG, Ph.D.

ACKNOWLEDGEMENTS

The writing of this dissertation has been one of the most significant challenges I have faced during past six years of my life. Without the support, patience and guidance of the following people, this study would not have been completed. I would like to express my deepest gratitude to all of them.

Prof Timothy Solberg took me as a student despite his many professional and other commitments. He has given me a great support to gain knowledge to overcome ignorance during this training. I would also like to thank him, Dr. Strahinja Stojadinovic and Dr.Arnold Pompos for the special sessions during my radiation therapy qualifying exam that really helped me learn about therapy physics. I would like to thank Dr. Solberg and Dr.Stojadinovic, who let me experience the small animal irradiator research in therapeutic physics field, practical issues beyond the text books and guiding my research for the past several years. I thank Dee Hill for correcting my dissertation along with my mentors (Dr.Timothy Solberg & Dr. Strahinja Stojadinovic). I would also like to thank my committee members for valuable suggestions during my research.

I would like to thank Dr.Michael Speiser and Dr. Kwang Song, were always willing to help and give their best suggestions. I would like thank my program assistant Kay Emerson for valuable suggestions and helping me during my down times in my training program. Finally I would like to thank my family members. They were always supporting me and encouraging me during my training.

November 18, 2012

ABSTRACT

DEVELOPMENT OF MONTE CARLO TREATMENT PLANNING AND DOSIMETRY SYSTEM FOR SMALL ANIMAL IRRADIATOR

The University of Texas Southwestern Medical Center at Dallas, 2012

Supervising Professor: Timothy Solberg

This work utilizes Monte Carlo simulation techniques to build a model of an x-ray tube in order to develop Monte Carlo treatment planning system for a small animal irradiator.

To accomplish this, the absolute dose calibration of the irradiator was performed in accordance with the recommendations of AAPM TG-61 protocol. Both in-air and in-water calibrations were performed at a 30.5 cm source-to-surface distance (SSD) for the reference applicator 40x40 mm^2 square field size. The BEAM/EGS Monte Carlo was used to model 225 kV photon beams from a small animal irradiator (Precision XRAD225). The Monte Carlo model was extensively tuned to provide good agreement with measurements of the beam characteristics (e.g. PDD and off-axis ratios). Subsequently, output factors for various square and circular applicators were measured using different dosimeters (ionization chamber, radiochromic film) and compared with MC simulations. The standard gamma index method with AAPM TG 53 recommendations are used to benchmark the measurements (radio chromic film) against

planar dose (Monte Carlo simulation) along with isodose lines and profiles in both homogeneous and heterogeneous mediums. The statistical uncertainty on the MC-calculated results is between 0.5% and 2% for most points. The CBCT images obtained on the XRAD 225Cx irradiator were converted to a material /density matrix as an input to DOSXYZnrc a MC dose computation module. The measured and computed point doses and isodose distributions were compared using the gamma index method. The absolute dose measured for reference collimator at 30.5 cm SSD in water and in air is 3.42 and 3.45 Gy/min. The agreement between simulated and measured dosimetric characteristics was excellent. For all fields, a good agreement is observed between measurements and calculations. Finally, a Monte Carlo treatment planning system for heterogeneous media is developed and validated.

LIST OF PUBLICATIONS & CONFERENCE ABSTRACTS

CONFERENCE ABSTRACTS

Pidikiti R, Stojadinovic S, Song K, Seliounine S, Speiser M, Saha D, Solberg T. Small Animal Stereotactic Irradiator: Med. Phys. Volume 36, Issue 6, pp. 2798-2798 (June 2009) (Oral Presentation, AAPM Annual Meeting) http://dx.doi.org/10.1118/1.3182618

Speiser M, **Pidikiti R**, Stojadinovic S, Song K, Solberg T. A Monte Carlo Model for Small Animal Stereotactic Irradiation: Med. Phys. Volume 36, Issue 6, pp. 2513-2513 (June 2009) (Poster Presentation, AAPM Annual Meeting) http://dx.doi.org/10.1118/1.3181450

Solberg T, **Pidikiti R**, Song K, Speiser M, Stojadinovic S, Saha D, Seliounine S. Development and Application of a Pre-Clinical Stereotactic Irradiator: Med. Phys. Volume 36, Issue 6, pp. 2720-2720 (June 2009) (Oral Presentation, AAPM Annual Meeting) http://dx.doi.org/10.1118/1.3182322

Pidikiti, R., Stojadinovic, S., Song, K., Speiser, M., Seliounine, S., Saha, D. & Solberg, T. 2009a. Dosimetric Characterization of Stereotactic Small Animal Irradiator. International Journal of Radiation Oncology Biology Physics, 75, S671-S671.

Pidikiti R, Stojadinovic S, Song K, Speiser M, Saha D, Seliounine S. Image Guided Stereotactic Small Animal Irradiator: Medical Physics and Biomedical Engineering World Congress, 2009.

PUBLICATIONS

Song K H, **Pidikiti R**, Stojadinovic S, Speiser M, Seliounine S, Saha D and Solberg T D 2010 An x-ray image guidance system for small animal stereotactic irradiation Phys. Med. Biol. 55 7345-62

Pidikiti, R., S. Stojadinovic, et al. (2011). "Dosimetric characterization of an image-guided stereotactic small animal irradiator." Phys Med Biol **56**(8): 2585-2599.

Marquez Dela Plata, C. D., Graces, J., Shokri kojori , E., Grinnan, J.., Krishnan, K., **Pidikit, R**., Spenc, J., Devosu, M. D., SR, Moore, C., Mccoll, R., Madden, C. & Diaz Arrastia,, R. 2011. Deficits in Functional Connectivity of Hippocampal and Frontal Lobe Circuits After Traumatic Axonal Injury. Arch Neurol, 68, 74-84.

LIST OF DEFINITIONS

CM- Component Module

CPU- Central Processing Unit

CT- Computed Tomography

DBS- Directional Bremsstrahlung Splitting

DICOM- Digital Imaging and Communications in Medicine

D_{MAX}- Depth of Maximum Dose

ECUT -Electron Cutoff Energy

EGS- Electron Gamma Shower

FWHM -Full Width Half Maximum

MCTPS – Monte Carlo treatment planning system

MC– Monte Carlo

NRCYCL Number of Recyclings

NTCP- Normal Tissue Complication Probability

OAR- Organs at Risk

OF–Output factor

OAR –Off-axis ratio

PDD – Percent depth dose

PC Primary Collimator

PCUT- Photon Cutoff Energy

PDF-Probability Density Function

PSF-Phase Space File

RT- Radiation Therapy

SAD- Source to Axis Distance

SSD Source to Surface Distance

TCP Tumor Control Probability

TPS -Treatment Planning System

LIST OF FIGURES

LIST OF TABLES

TABLE OF CONTENTS

CHAPTER ONE

INTRODUCTION

1. 1 Introduction

Modern radiotherapy combines advanced imaging technologies, computerized treatment planning systems and high-energy medical accelerators to optimize radiation dose to a target volume while effectively sparing the healthy tissue. Technological advances are now producing quantifiable improvements in treatment outcomes of patients treated with radiation therapy. Moreover, technological progress in imaging modalities for patient treatment is enabling a fundamental paradigm shift in the practice of radiation therapy. The new paradigm is a departure from the small doses per fraction traditionally delivered over many weeks, i.e., conventionally fractionated radiotherapy (CFRT), in favor of large, ablative doses delivered in a few fractions in two weeks or less. This is commonly referred to as stereotactic ablative radiotherapy (SABR) or stereotactic body radiation therapy (SBRT). SBRT utilizes a hypo-fractionated dose regimen in which the total therapeutic dose is delivered in five fractions or less. The benefit of SBRT, particularly evident in early stage lung cancer patients unfit for surgery, has allowed an absolute reduction in the rate of in-field recurrence on the order of 50% compared to CFRT (Cheung et al., 2000, Qiao et al., 2003) . Additionally, 80-95% local control rates for stage I lung cancer have been reported in multiple prospective studies (Timmerman et al., 2010, Timmerman et al., 2007, Fakiris et al., 2009). In a national prospective trial, local control in excess of 97% was reported for patients with inoperable stage I lung cancer treated using SBRT. Similar success has been reported for SBRT of lung and liver

metastases (Ricardi et al., 2012, Maehata et al., 2011, Herfarth et al., 2001, Herfarth et al., 2004, Rusthoven et al., 2009, Onishi et al., 2004, Hof et al., 2007, Wulf et al., 2004). These rates rival the best surgical series.

1.1.1 Preclinical research

Cancer is a disease with high mortality and morbidity. Approximately half of all cancer patients in the USA undergo radiotherapy at some stage of their treatment (Siegel et al., 2012, Jemal et al., 2010). Technological innovation in the field of radiotherapy has allowed optimizing tumor control and normal tissue complication probability through the use of novel beam delivery techniques. While new technologies have been successfully clinically implemented, this has been done with little concurrent companion animal research or radiobiological studies. Significantly, there is a fundamental lag in understanding of the biological mechanisms in this SBRT technique. Thus far, only limited pre-clinical data exist in support of high dose irradiation. This presents an opportunity for the development of preclinical models for studying the impact of fractionated high doses in tumors and normal tissues. The essential technology for small animal irradiation would incorporate high resolution image guidance, high accuracy and precision in targeting, and robust treatment planning.

In the field of medical and molecular imaging, the trend of swift clinical implementation of technological innovation has been successfully followed by the development of small animal imaging systems. Each anatomical and functional imaging modality for humans is, at present, commercially available for small animal use as well. Small animal imaging systems provide new insights into cancer detection and characterization, and continue to have a noteworthy impact in the fundamental

understanding of tumor kinetics, the effects of tumor growth on the local environment, and tumor response to treatment (Wessels et al., 2007, Bahri et al., 2008, Bradbury et al., 2008, Lin et al., 2011, O'Neill et al., 2010).

In contrast to sophisticated small animal imaging systems available, conformal radiotherapy systems for small animals are uncommon and presently under development by only a few groups in North America. The approaches in design and implementation have been varied , a common theme is to incorporate image guidance with conformal, small field radiotherapy. Notable efforts in the development of small animal irradiation systems have been presented by research teams from Washington University School of Medicine (Stojadinovic et al., 2006, Kiehl et al., 2008, Stojadinovic et al., 2007), Johns Hopkins University (Deng et al., 2007, Matinfar et al., 2009, Matinfar et al., 2007, Wong et al., 2008), Stanford University (Zhou et al., 2010, Graves et al., 2007, Bazalova et al., 2009, Motomura et al., 2010), Princess Margaret Hospital (Lindsay et al., 2009, Chow, 2010, Chow and Leung, 2007, Chow and Leung, 2008, Chow et al., 2010, Lindsay et al., 2008), University of Arkansas Medical Sciences (Moros et al., 2009, Sharma et al., 2008) and University of Texas Southwestern Medical Center (Pidikiti et al., 2009a, Pidikiti et al., 2009b, Pidikiti et al., 2011, Pidikiti et al., 2010, Saha et al., 2010, Song and et al., 2010).

1.2 Importance of dosimetric accuracy in the field of radiotherapy

The success of radiotherapy depends on numerous factors such as appropriate diagnosis, target definition, planning treatment volume, identification of critical structures, selection of irradiation technique, combination of beam arrangements , dose/fractionation scheme and quality assurance. Uncertainties and errors in any of these steps can have great impact in the treatment outcome. Additionally, the steep dose response necessitates better than 5% dosimetric accuracy to ensure acceptable levels of tumor control probability (TCP) and normal tissue complication probability (NTCP) for favorable treatment outcomes (Brahme, 1984, Mijnheer et al., 1987, Overgaard and Bartelink, 1995, Dutreix, 1984). In the field of radiation therapy, small differences between toxic and therapeutic doses result in a narrow therapeutic window, defined as a ratio of TCP to NTCP. The central theme for novel radiotherapy protocols is to improve this therapeutic ratio. Radiation oncologists and medical physicists use both physical and biological means to influence the therapeutic ratio to achieve better results. For example, conforming the radiation beam precisely to the shape of a tumor in the "beam's eye view" may provide higher tumoricidal doses without increasing toxic effects. Research in the biology of radiotherapy shows that beam uniformity, treatment volume, shape of dose distribution, and absolute dose delivered dominate the biological effects (Emami et al., 1991, Overgaard and Bartelink, 1995).

1.2.1 Heterogeneity corrections

Radiation therapy dose-calculation algorithms determine the energy deposited within a volume of interest resulting from an incident x-ray beam. Dose calculation

algorithms work best in well-defined conditions such as a homogenous medium with large unmodified fields with normal incidence and where charged particle equilibrium has been established. Accurate dose calculation in a variety of other beam configurations such as with small field sizes, at beam boundaries, at curved surfaces or tissue interfaces, or combinations of these, is quite challenging. According to the TG-65 protocol (Papanikolaou et al., 2004), inhomogeneity correction methods can be categorized based on local energy deposition (no electron transport) and non-local energy deposition (electron transport). Algorithms such as effective linear attenuation, ratio of tissue-air ratios (RTAR), Batho power law and equivalent TAR, do not incorporate electron transport and don't account for the recoil electrons and scattered photons in the medium. In the presence of tissue heterogeneities, these simple methods provide adequate results with less than 5% error in regions far away from the inhomogeneity, but with complex heterogeneous medium dose calculations within or near the inhomogeneity the errors can be much higher than 5%. In contrast, algorithms that can incorporate electron transport include convolution, superposition/convolution and Monte Carlo. Convolution algorithms do not account for scattered photons and recoil electrons, whereas superposition/ convolution and Monte Carlo methods do (Mackie et al., 1985, Boyer and Mok, 1986, Papanikolaou and Mackie, 1992). Heterogeneous tissues pose a significant challenge to dose calculations in the orthovoltage energy range (150-500kVp), where neither category of algorithm provides a reliable calculation of dose (Sontag et al., 1977, Sontag and Cunningham, 1977, Fullerton et al., 1978, Parker et al., 1980, Van Dyk et al., 1982, Altschuler et al., 1983, Cunningham, 1983). A study evaluating a convolution/super position algorithm with 120 kV x-rays demonstrated dose differences of 47% at a

bone/solid water interface and an overall difference of 9% between measured and computed dose (Alaeia et al., 2000).

Photon transport is intrinsically probabilistic in an interacting medium, as it depends on the photon energy and medium composition and density. In the orthovoltage energy range, photon interactions are dominated by Compton and photoelectric interactions. The probability of Compton interactions is proportional to electron density, while the photoelectric interaction probability is proportional to the ratio of atomic number Z and energy E as Z^3/E^3 (Attix, 1986, Johns and Cunningham, 1983). Existing clinical treatment planning systems are not suitable for small animal irradiation at these energies, because the models are valid primarily for high (MV) energies and broad beams and do not account for photoelectric interactions within the dose calculations (Verhaegen et al., 2011). These interactions can contribute significant dose to the bone relative to the tissue, which is critical for small animal irradiation. One of the important tools for any biological studies is an accurate treatment planning system (TPS) for small animal irradiation, which is a main focus of this work.

The orthovoltage energies used for small animal irradiation also pose a serious challenge with regard to the physical measurement of dosimetric parameters. Photoelectron contamination, secondary scattered electrons and backscattered photons, in conjunction with small collimated beams make it difficult to measure that depth dose curves in homogeneous medium, especially near the surface. Tissue inhomogeneities, such as bone or tissue-air interfaces have a large effect on dose deposition. Accurate measurement is further challenged by the lack of lateral electronic equilibrium, steep dose gradients and finite size of physical detectors (Fan et al., 2009).

Small animal irradiators are equipped with small-field applicators projecting field sizes as small as1 to 5 mm in diameter; accurate ion chamber dosimetry is impossible with fields this small as the volume of the chamber is much larger than the beam diameter (McKerracher and Thwaites, 1999). Similarly use of a semiconductor diode detectors can produce ±15% error due to its energy dependence (Song et al., 2006). The high spatial resolution of film makes it a viable candidate for small field dosimetry. While EBT2 film is relatively energy independent, it does over respond by a few percent at energies below 50 keV. This over response can be corrected using an appropriate calibration technique (Butson et al., 2010).

1.2.2 Necessity for Monte Carlo

For reasons described above, a Monte Carlo model validation is an invaluable tool for overcoming the dosimetric difficulties associated with small animal irradiation at orthovoltage energies. The Monte Carlo technique simulates the transport of electrons and photons through various media by utilizing the probability distribution of their interactions with the materials in question, tracking the trajectories of each particle. It uses fundamental physics, i.e., the differential cross-sections for processes including Compton scattering, pair production in the field of the atom and nucleus and, photoelectric absorption and Rayleigh scattering of photons. As electrons traverse matter, they undergo a large number of elastic interactions and lose energy through inelastic collisions and radiative (Bremsstrahlung) interactions.

A Monte Carlo (MC) algorithm has the ability to accurately compute dose for arbitrarily complex geometric media involving small animals by simulating all types of ionizing interactions (Siebers and Ma, 2006). Monte Carlo makes no assumptions

regarding radiation equilibrium, so it can be used for small fields where lateral equilibrium is absent, and in heterogeneous media. MC technique simulates the radiation transport through various media by utilizing well established probability distributions governing the individual interactions of particles (photons and electrons). Each particle travels through the medium and give rise to energy deposition within the medium. Scoring physical quantities of interest requires a large number of particle simulations to obtain reasonable accuracy of the result. The focus of this research is to perform comprehensive dosimetry measurements for a preclinical small animal irradiator and to develop and commission a Monte Carlo treatment planning system. There are various Monte Carlo algorithms for dose calculation available. In this research, we use the EGSnrc (Kawrakow et al., 2011) radiation transport code. EGSnrc has low energy physics improvements compared to its previous version EGS4 (Nelson et al., 1985). It has sophisticated user codes such as BEAMnrc to build accelerators and DOSXYZnrc module for more flexibility of computing dose while still utilizing the main EGS Monte Carlo code.

1.2.3 Project Outline

The ultimate goal of this research project is to develop a Monte Carlo-based treatment planning system for the XRAD 225Cx small animal irradiator. To accomplish this, a geometric model was created based on manufacturer's specifications of the irradiator using the BEAMnrc application package of EGSnrc Monte Carlo particle transport code. This model was used to create a phase-space file, containing information on the particles' energy and momentum for dose calculation. The MC spectrum was validated against the spectrum obtained from an analytical modeling software package

called Spekcalc (Poludniowski et al., 2009) and by comparing measured and calculated half-value-layers (HVL).

Following the validation, absolute dose calibration was performed using the AAPM TG-61 (Ma et al., 2001) methodology for the XRAD 225Cx irradiator. For each collimator, dosimetric parameters such as percent depth dose (PDD), output factors (OF), off-axis ratios (OAR), and penumbra were measured in water and in solid water phantoms using various dosimeters including a pinpoint ionization chamber and radiochromic film. The beam profile measurements obtained with EBT2 film showed a field size dependent over-response beyond the penumbra region compared to MC data and ion chamber measurements. This observation was further investigated and explained. The gamma index method (Low et al., 1998) and AAPM TG 53 recommendations were used to compare planar radiochromic film measurements against Monte Carlo simulations.

Finally, a Monte Carlo treatment planning system designed to perform accurate radiation dose calculations in heterogeneous media was developed and validated. Cone beam CT (CBCT) images obtained on the XRAD 225Cx irradiator itself were converted to a material /density matrix for input to DOSXYZnrc for subsequent MC dose computations.

References

ALAEIA , P., GERBI, B. J. & GEISE, A. R. 2000. Evaluation of a model-based treatment planning system for dosecomputations in the kilovoltage energy range. *Med. Phys.,* 27**,** 2821-2826.

ALTSCHULER, M. D., SONTAG, M. R. & BLOCH, P. 1983. Three-dimensional dose calculations for photon beam therapy. *Med. Phys.,* 10**,** 529.

ATTIX, F. H. 1986. *Introduction to Radiological Physics and Radiation Dosimetry*.

BAHRI, S., CHEN, J. H., YU, H. J., KUZUCAN, A., NALCIOGLU, O. & SU, M. Y. 2008. Can dynamic contrast-enhanced MRI (DCE-MRI) predict tumor recurrence and lymph node status in patients with breast cancer? *Annals of Oncology,* 19**,** 822-4.

BAZALOVA, M., ZHOU, H., KEALL, J. P. & GRAVES, E. E. 2009. Kilovoltage beam Monte Carlo dose calculations in submillimeter voxels for small animal radiotherapy. *Medical Physics,* 36**,** 4991-4999.

BOYER, A. L. & MOK, E. C. 1986. *Calculation of photon dose distributions in an inhomogeneous medium using convolutions,* AAPM.

BRADBURY, M. S., HAMBARDZUMYAN, D., ZANZONICO, P. B., SCHWARTZ, J., CAI, S., BURNAZI, E. M., LONGO, V., LARSON, S. M. & HOLLAND, E. C. 2008. Dynamic Small-Animal PET Imaging of Tumor Proliferation with 3′-Deoxy-3′-18F-Fluorothymidine in a Genetically Engineered Mouse Model of High-Grade Gliomas. *Journal of Nuclear Medicine,* 49**,** 422-429.

BRAHME, A. 1984. Dosimetric precision requirements in radiation therapy. *Acta Radiol Oncology,* 23.

BUTSON, M. J., YU, P. K. N., CHEUNG, T. & ALNAWAF, H. 2010. Energy response of the new EBT2 radiochromic film to x-ray radiation. *Radiation Measurements,* 45**,** 836-839.

CHEUNG, P. C., MACKILLOP, W. J., DIXON, P., BRUNDAGE, M. D., YOUSSEF, Y. M. & ZHOU, S. 2000. Involved-field radiotherapy alone for early-stage non-small-cell lung cancer. *Int J Radiat Oncol Biol Phys,* 48**,** 703-10.

CHOW, J. C. L. 2010. Depth dose dependence of the mouse bone using kilovoltage photon beams: A Monte Carlo study for small-animal irradiation. *Radiation Physics and Chemistry,* 79**,** 567-574.

CHOW, J. C. L. & LEUNG, M. K. K. 2007. Treatment planning for a small animal using Monte Carlo simulation. *Medical Physics,* 34**,** 4810-4817.

CHOW, J. C. L. & LEUNG, M. K. K. 2008. A graphical user interface for calculation of 3D dose distribution using Monte Carlo simulations. *Journal of Physics: Conference Series,* 102**,** 012003.

CHOW, J. C. L., LEUNG, M. K. K., LINDSAY, P. E. & JAFFRAY, D. A. 2010. Dosimetric variation due to the photon beam energy in the small-animal irradiation: A Monte Carlo study. *Medical Physics,* 37**,** 5322-5329.

CUNNINGHAM, J. R. 1983. Current and future Development of Tissue Inhomogeneity Corrections for Photon Beam Clinical Dosimetry with the Use of CT. *J. Morton (eds.) (New York: Raven Press) pp. 209–18 (1983),* 209-18

DENG, H., KENNEDY, C. W., ARMOUR, E., TRYGGESTAD, E., FORD, E., MCNUTT, T., JIANG, L. & WONG, J. 2007. The small-animal radiation research platform (SARRP): dosimetry of a focused lens system. *Phys Med Biol,* 52**,** 2729-40.

DUTREIX, A. 1984. When and how can we improve precision in radiotherapy? *Radiotherapy and oncology,* 2**,** 275-292.

EMAMI, B., LYMAN, J., BROWN, A., COIA, L., GOITEIN, M., MUNZENRIDER, J. E., SHANK, B., SOLIN, L. J. & WESSON, M. 1991. Tolerance of normal tissue to therapeutic irradiation. *Int J Radiat Oncol Biol Phys,* 21**,** 109-22.

FAKIRIS, A. J., MCGARRY, R. C., YIANNOUTSOS, C. T., PAPIEZ, L., WILLIAMS, M., HENDERSON, M. A. & TIMMERMAN, R. 2009. Stereotactic Body Radiation Therapy for Early-Stage Non–Small-Cell Lung Carcinoma: Four-Year Results of a Prospective Phase II Study. *International Journal of Radiation Oncology*Biology*Physics,* 75**,** 677-682.

FAN, J., PASKALEV, K., WANG, L., JIN, L., LI, J., ELDEEB, A. & MA, C. 2009. *Determination of output factors for stereotactic radiosurgery beams,* AAPM.

FULLERTON, G. D., SEWCHAND, W., PAYNE, J. T. & LEVITT, S. H. 1978. CT determination of parameters for inhomogeneity corrections in radiation therapy of the esophagus. *Radiology,* 126**,** 167-71.

GRAVES, E. E., ZHOU, H., CHATTERJEE, R., KEALL, P. J., GAMBHIR, S. S., CONTAG, C. H. & BOYER, A. L. 2007. Design and evaluation of a variable aperture collimator for conformal radiotherapy of small animals using a microCT scanner. *Med Phys,* 34**,** 4359-67.

HERFARTH, K. K., DEBUS, J., LOHR, F., BAHNER, M. L., RHEIN, B., FRITZ, P., HOSS, A., SCHLEGEL, W. & WANNENMACHER, M. F. 2001. Stereotactic single-dose radiation therapy of liver tumors: results of a phase I/II trial. *Journal of clinical oncology : official journal of the American Society of Clinical Oncology,* 19**,** 164-70.

HERFARTH, K. K., DEBUS, J. & WANNENMACHER, M. 2004. Stereotactic radiation therapy of liver metastases: update of the initial phase-I/II trial. *Front Radiat Ther Oncol,* 38**,** 100-5.

HOF, H., HOESS, A., OETZEL, D., DEBUS, J. & HERFARTH, K. 2007. Stereotactic Single-Dose Radiotherapy of Lung Metastases. *Strahlentherapie und Onkologie,* 183**,** 673-678.

JEMAL, A., SIEGEL, R., XU, J. & WARD, E. 2010. Cancer Statistics, 2010. *CA: A Cancer Journal for Clinicians,* 60**,** 277-300.

JOHNS, H. E. & CUNNINGHAM, J. R. 1983. The Physics of Radiology,Fourth Edition *Charles C. Thomas, Springfield,IL* .

KAWRAKOW, I., MAINEGRA-HING, E., ROGERS, D. W. O., TESSIER, F. & WALTERS, B. R. B. 2011. The EGSnrc Code System: Monte Carlo Simulation of Electron and Photon Transport *NRCC Report PIRS-701*

KIEHL, E. L., STOJADINOVIC, S., MALINOWSKI, K. T., LIMBRICK, D., JOST, S. C., GARBOW, J. R., RUBIN, J. B., DEASY, J. O., KHULLAR, D., IZAGUIRRE, E. W., PARIKH, P. J., LOW, D. A. & HOPE, A. J. 2008. Feasibility of small animal cranial irradiation with the microRT system. *Medical Physics,* 35**,** 4735-4743.

LIN, Y., THAYER, D., NALCIOGLU, O. & GULSEN, G. 2011. Tumor characterization in small animals using magnetic resonance-guided dynamic contrast enhanced diffuse optical tomography. *Journal of Biomedical Optics,* 16**,** 106015.

LINDSAY, P., ANSELL, S., JELVEH, S., CLARKSON, R., WILSON, G., HILL, R. & JAFFRAY, D. 2009. Implementation of An Image-Guided System for Conformal Small Animal Irradiation: Characterization, QA, and Workflow. 36**,** 2799.

LINDSAY, P., ANSELL, S., MOSELEY, D., JELVEH, S., HILL, R. & JAFFRAY, D. 2008. Development of An Image-Guided Conformal Small Animal Irradiation Platform. 35**,** 2695.

LOW, D. A., HARMS, W., MUTIC, S. & PURDY, J. 1998. A technique for the quantitative evaluation of dose distributions. *Med. Phys.*, 25**,** 656.

MA, C. M., COFFEY, C. W., DEWERD, L. A., LIU, C., NATH, R., SELTZER, S. M. & SEUNTJENS, J. P. 2001. AAPM protocol for 40-300 kV x-ray beam dosimetry in radiotherapy and radiobiology. *Med Phys,* 28**,** 868-93.

MACKIE, T. R., SCRIMGER, J. W. & BATTISTA, J. J. 1985. *A convolution method of calculating dose for 15 MV x rays,* AAPM.

MAEHATA, Y., ONISHI, H., KURIYAMA, K., AOKI, S., ARAYA, M., SAITO, R., OGURI, M., MARINO, K., KOMIYAMA, T. & ARAKI, T. 2011. Stereotactic Body Radiotherapy for Stage I Non-small Cell Lung Cancer Causes Immune Suppression. *International journal of radiation oncology, biology, physics,* 81**,** S624.

MATINFAR, M., FORD, E., IORDACHITA, I., WONG, J. & KAZANZIDES, P. 2009. Image-guided small animal radiation research platform: calibration of treatment beam alignment. *Phys Med Biol,* 54**,** 891-905.

MATINFAR, M., GRAY, O., IORDACHITA, I., KENNEDY, C., FORD, E., WONG, J., TAYLOR, R. H. & KAZANZIDES, P. 2007. Small animal radiation research platform: imaging, mechanics, control and calibration. *Med Image Comput Comput Assist Interv,* 10**,** 926-34.

MCKERRACHER, C. & THWAITES, D. I. 1999. Assessment of new small-field detectors against standard-field detectors for practical stereotactic beam data acquisition. *Physics in Medicine and Biology,* 44**,** 2143.

MIJNHEER, B. J., BATTERMANN, J. J. & WAMBERSIE, A. 1987. What degree of accuracy is required and can be achieved in photon and neutron therapy? *Radiotherapy and Oncology,* 8**,** 237-252.

MOROS, E., SHARMA, S., CORRY, P., CHAO, M., GRIFFIN, R., MIHAYLOV, I. & PENAGARICANO, J. 2009. An Integrated Robotic-Based Irradiation System for Small Animal Research. 36**,** 2720.

MOTOMURA, A. R., BAZALOVA, M., HU, Z., KEALL, P. J. & GRAVES, E. E. 2010. Investigation of the effects of treatment planning variables in small animal radiotherapy dose distributions. *Medical Physics,* 37**,** 590-599.

NELSON, W. R., HIRAYAMA, H. & ROGERS, D. W. O. 1985. The EGS4 Code System. *SLAC-265,Stanford Linear Accelerator Center*.

O'NEILL, K., LYONS, S. K., GALLAGHER, W. M., CURRAN, K. M. & BYRNE, A. T. 2010. Bioluminescent imaging: a critical tool in pre-clinical oncology research. *The Journal of Pathology,* 220**,** 317-327.

ONISHI, H., ARAKI, T., SHIRATO, H., NAGATA, Y., HIRAOKA, M., GOMI, K., YAMASHITA, T., NIIBE, Y., KARASAWA, K., HAYAKAWA, K., TAKAI, Y., KIMURA, T., HIROKAWA, Y., TAKEDA, A., OUCHI, A., HAREYAMA, M., KOKUBO, M., HARA, R., ITAMI, J. & YAMADA, K. 2004. Stereotactic hypofractionated high-dose irradiation for stage I nonsmall cell lung carcinoma: clinical outcomes in 245 subjects in a Japanese multiinstitutional study. *Cancer,* 101**,** 1623-31.

OVERGAARD, J. & BARTELINK, H. 1995. About tolerance and quality. An important notice to all radiation oncologists. *Radiotherapy and oncology,* 35.

PAPANIKOLAOU, N., BATTISTA, J., BOYER, A. L., KAPPAS, C., KLEIN, E. E., MACKIE, T. R., SHARPE, M. & VANDYK, J. 2004. Tissue Inhomogeneity Corrections for Megavoltage Photon Beams; Report of Task Group No. 65 of the Radiation Therapy Committee of the American Association of Physicists in Medicine. *Medical Physics Publishing,Madison, Wisconsin,* 85**,** 1-135.

PAPANIKOLAOU, N. & MACKIE, T. R. 1992. A new convolution approach for the generation of polyenergetic photon beam dose distributions. *Med. Phys.,* 19**,** 821.

PARKER, R. P., CONTIER DE FREITAS, L., CASSELL, K. J., WEBB, S. & HOBDAY, P. A. 1980. A method of implementing inhomogeneity cor rections in radiotherapy treatment planning: Comparison with experiment and Monte Carlo calculations. *J. Eur. Radiother.,* 1**,** 93-100.

PIDIKITI, R., STOJADINOVIC, S., SONG, K., SPEISER, M., SELIOUNINE, S., SAHA, D. & SOLBERG, T. 2009a. Dosimetric Characterization of Stereotactic Small Animal Irradiator. *International Journal of Radiation Oncology Biology Physics,* 75**,** S671-S671.

PIDIKITI, R., STOJADINOVIC, S., SONG, K., SPEISER, M., SELIOUNINE, S., SAHA, D. & SOLBERG, T. D. 2009b. Image-Guided Stereotactic Small Animal Irradiator. *In:* DÖSSEL, O. & SCHLEGEL, W. C. (eds.) *World Congress on Medical Physics and Biomedical Engineering, September 7 - 12, 2009, Munich, Germany.* Springer Berlin Heidelberg.

PIDIKITI, R., STOJADINOVIC, S., SPEISER, M., SONG, K. H., HAGER, F., SAHA, D. & SOLBERG, T. D. 2011. Dosimetric characterization of an image-guided stereotactic small animal irradiator. *Phys Med Biol,* 56**,** 2585-99.

PIDIKITI, R., STOJADINOVIC, S., SPEISER, M., SONG, K. H. & SOLBERG, T. D. 2010. Energy Dependency and Dosimetric Modeling in Small Animal Stereotactic Irradiation. *Medical Physics,* 37**,** 3456.

POLUDNIOWSKI, G., LANDRY, G., DEBLOIS, F., EVANS, P. M. & VERHAEGEN, F. 2009. SpekCalc: a program to calculate photon spectra from tungsten anode x-ray tubes. *Phys Med Biol,* 54**,** N433-8.

QIAO, X., TULLGREN, O., LAX, I., SIRZEN, F. & LEWENSOHN, R. 2003. The role of radiotherapy in treatment of stage I non-small cell lung cancer. *Lung Cancer,* 41**,** 1-11.

RICARDI, U., FILIPPI, A. R., GUARNERI, A., RAGONA, R., MANTOVANI, C., GIGLIOLI, F., BOTTICELLA, A., CIAMMELLA, P., IFTODE, C., BUFFONI, L., RUFFINI, E. & SCAGLIOTTI, G. V. 2012. Stereotactic body radiation therapy for lung metastases. *Lung Cancer,* 75**,** 77-81.

RUSTHOVEN, K. E., KAVANAGH, B. D., CARDENES, H., STIEBER, V. W., BURRI, S. H., FEIGENBERG, S. J., CHIDEL, M. A., PUGH, T. J., FRANKLIN, W., KANE, M., GASPAR, L. E. & SCHEFTER, T. E. 2009. Multi-institutional phase I/II trial of stereotactic body radiation therapy for liver metastases. *J Clin Oncol,* 27**,** 1572-8.

SAHA, D., WATKINS, L., YIN, Y., THORPE, P., STORY, M. D., SONG, K., RAGHAVAN, P., TIMMERMAN, R., CHEN, B., MINNA, J. D. & SOLBERG, T. D. 2010. An orthotopic lung tumor model for image-guided microirradiation in rats. *Radiat Res,* 174**,** 62-71.

SHARMA, S., MOROS, E. & CORRY, P. 2008. Small Animal Conformal Radiation Therapy Device. 35**,** 2718-2718.

SIEBERS, J. V. & MA, C. 2006. Integrating new technologies into the clinc: Monte Carlo and Image-guided Radiotherapy *AAPM Medical Physicsits Monograph,* 32**,** 145-169.
SIEGEL, R., NAISHADHAM, D. & JEMAL, A. 2012. Cancer statistics, 2012. *CA: A Cancer Journal for Clinicians,* 62**,** 10-29.
SONG, H., AHMAD, M., DENG, J., CHEN, Z., YUE, N. J. & NATH, R. 2006. Limitations of silicon diodes for clinical electron dosimetry. *Radiat Prot Dosimetry,* 120**,** 56-9.
SONG, K. H. & ET AL. 2010. An x-ray image guidance system for small animal stereotactic irradiation. *Physics in Medicine and Biology,* 55**,** 7345.
SONTAG, M. R., BATTISTA, J. J., BRONSKILL, M. J. & CUNNINGHAM, J. R. 1977. Implications of computed tomography for inhomogeneity corrections in photon beam dose calculations. *Radiology,* 124**,** 143-9.
SONTAG, M. R. & CUNNINGHAM, J. R. 1977. *Corrections to absorbed dose calculations for tissue inhomogeneities,* AAPM.
STOJADINOVIC, S., LOW, D. A., HOPE, A. J., VICIC, M., DEASY, J. O., CUI, J., KHULLAR, D., PARIKH, P. J., MALINOWSKI, K. T., IZAGUIRRE, E. W., MUTIC, S. & GRIGSBY, P. W. 2007. MicroRT-small animal conformal irradiator. *Med Phys,* 34**,** 4706-16.
STOJADINOVIC, S., LOW, D. A., VICIC, M., MUTIC, S., DEASY, J. O., HOPE, A. J., PARIKH, P. J. & GRIGSBY, P. W. 2006. Progress toward a microradiation therapy small animal conformal irradiator. *Med Phys,* 33**,** 3834-45.
TIMMERMAN, R., PAULUS, R., GALVIN, J., MICHALSKI, J., STRAUBE, W., BRADLEY, J., FAKIRIS, A., BEZJAK, A., VIDETIC, G., JOHNSTONE, D., FOWLER, J., GORE, E. & CHOY, H. 2010. Stereotactic body radiation therapy for inoperable early stage lung cancer. *JAMA,* 303**,** 1070-6.
TIMMERMAN, R. D., PARK, C. & KAVANAGH, B. D. 2007. The North American experience with stereotactic body radiation therapy in non-small cell lung cancer. *J Thorac Oncol,* 2**,** S101-12.
VAN DYK, J., KEANE, T. J. & RIDER, W. D. 1982. Lung density as measured by computerized tomography: implications for radiotherapy. *Int J Radiat Oncol Biol Phys,* 8**,** 1363-72.
VERHAEGEN, F., GRANTON, P. & TRYGGESTAD, E. 2011. Small animal radiotherapy research platforms. *Phys Med Biol,* 56**,** R55-83.
WESSELS, J. T., BUSSE, A. C., MAHRT, J., DULLIN, C., GRABBE, E. & MUELLER, G. A. 2007. In vivo imaging in experimental preclinical tumor research. *A review Cytometry- Part A,* 71A**,** 524-9.
WONG, J., ARMOUR, E., KAZANZIDES, P., IORDACHITA, I., TRYGGESTAD, E., DENG, H., MATINFAR, M., KENNEDY, C., LIU,

Z., CHAN, T., GRAY, O., VERHAEGEN, F., MCNUTT, T., FORD, E. & DEWEESE, T. L. 2008. High-resolution, small animal radiation research platform with x-ray tomographic guidance capabilities. *Int J Radiat Oncol Biol Phys*, 71**,** 1591-9.

WULF, J., HAEDINGER, U., OPPITZ, U., THIELE, W., MUELLER, G. & FLENTJE, M. 2004. Stereotactic radiotherapy for primary lung cancer and pulmonary metastases: A noninvasive treatment approach in medically inoperable patients. *International Journal of Radiation Oncology*Biology*Physics*, 60**,** 186-196.

ZHOU, H., RODRIGUEZ, M., VAN DEN HAAK, F., NELSON, G., JOGANI, R., XU, J., ZHU, X., XIAN, Y., TRAN, P. T., FELSHER, D. W., KEALL, P. J. & GRAVES, E. E. 2010. Development of a Micro-Computed Tomography-Based Image-Guided Conformal Radiotherapy System for Small Animals. *Int J Radiat Oncol Biol Phys*.

CHAPTER TWO

Dosimetric characterization of small animal irradiator

2.1 Introduction

Animal irradiation systems can facilitate scientific testing of biomedical hypotheses in a variety of tumor models and normal tissues with the ultimate aim of both promoting translational research and providing novel protocols for human cancer treatments. A small animal irradiator that can mimic clinical stereotactic ablative delivery is an essential tool for quantitative experiments to assess tumor and healthy tissue response to focused, high dose radiation. For successful pre-clinical SBRT studies, it is important to localize the intended target(s) with high precision, to verify localization using image guidance, and to rapidly administer radiation. High dose rates in conjunction with small-aperture collimators are crucial for high volume throughput and for minimizing the likelihood of animal death due to prolonged exposure to anesthesia. A commercial x-ray device (XRAD 225Cx, Precision X-Ray, Inc., North Branford, and CT) meets the requirements for preclinical small animal platform by offering a high-precision three-dimensional (3D) translation stage integrated with CBCT x-ray image guidance. The x-ray source used for both image and treatment is mounted on a rotational gantry, facilitating multi-beam delivery needed to ensure compact dose distributions. Dosimetric characterization of the radiation parameters of this device is the focus of this chapter.

2.2 Small animal irradiator

The XRAD 225Cx irradiator consists of four main components: an industrial x-ray unit, a small field collimating system, a c-arm rotating gantry and an image guidance system (Figure 2.1). All components all enclosed in a self-shielding cabinet, and therefore the irradiator can be operated in an environment without the need for special shielding. The irradiator is computer controlled (Dell Precision T7500, Intel Xeon six core 2.93 GHz processor, 12 GB of RAM, Windows 7 Professional) utilizing *Pilot* software provided by the manufacturer. The software controls the animal stage, gantry motion, image acquisition and reconstruction, and the x-ray beam. Alternatively, the beam can be generated using only the x-ray console, with all other parameters fixed.

2.2.1 X-ray source

The radiation source is a commercial MXR-225 x-ray tube (Comet AG, Liebefeld-Berne, Switzerland) which produces both imaging (utilizing a small, 1.0 mm focal spot) and treatment beams (utilizing either small or large, 3.0 mm focal spot). The x-ray target consists of a tungsten anode with a target angle of 20º. The tube has an inherent filtration of 0.8 mm beryllium. The x-ray source specifications for the XRAD 225Cx irradiator are given in Table 2.1 and shown in Figure 2.2. The nominal x-ray tube potential ranges continuously from 5 to 225 kVp, while the tube current ranges from 1 to 13 mA. This capability allows both diagnostic (~30-70 kVp) and therapeutic (225 kVp) applications. 225 kVp provides adequate penetration for small animal radiotherapy. Exposure times can be set from 1 to 100 minutes in 1 sec increments. An integrated filter holder allows the user to add beam- conditioning filters to achieve a desired beam quality (typically specified by the half-value layer).

Typically, a 1.65 mm aluminum filter is used for imaging, while therapeutic beams are filtered with 0.3 mm of copper.

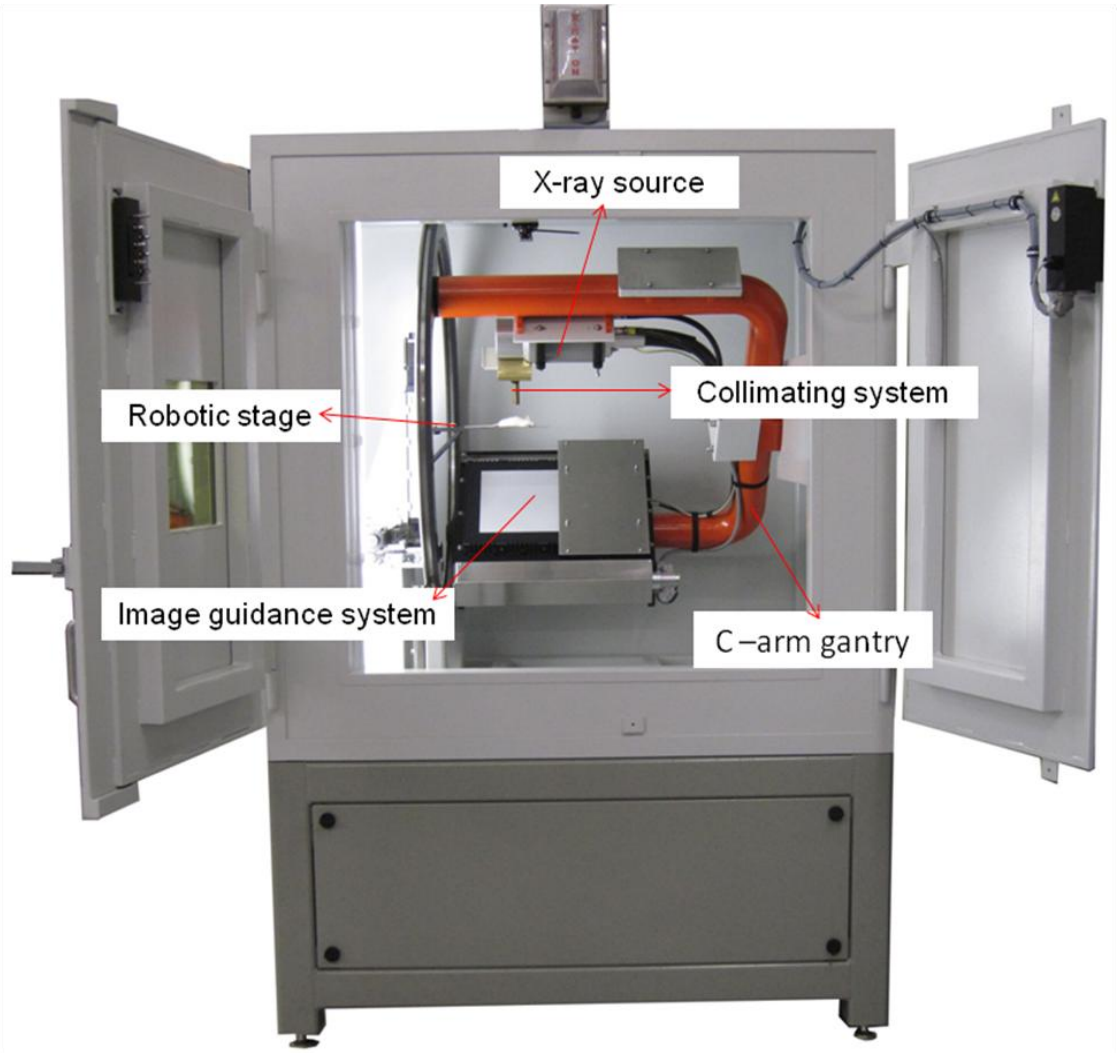

Figure 2.1**:** XRAD 225Cx irradiator

X-ray source specifications for XRAD 225Cx	
Manufacturer	Comet
Model	MXR 225/22
Target angle	20º
Dual focal spot size (EN 12543)	1 mm and 3.0 mm diameter
Power (small focal spot)	640W
Power (large focal spot)	3000W
Inherent filtration	0.8 mm Be
Additional filtration	1.65 mm Al and 0.3 mm Cu
Generator	GE TITAN 225 kV

Table 2.1: The specifications for the x-ray tube for XRAD 225Cx irradiator

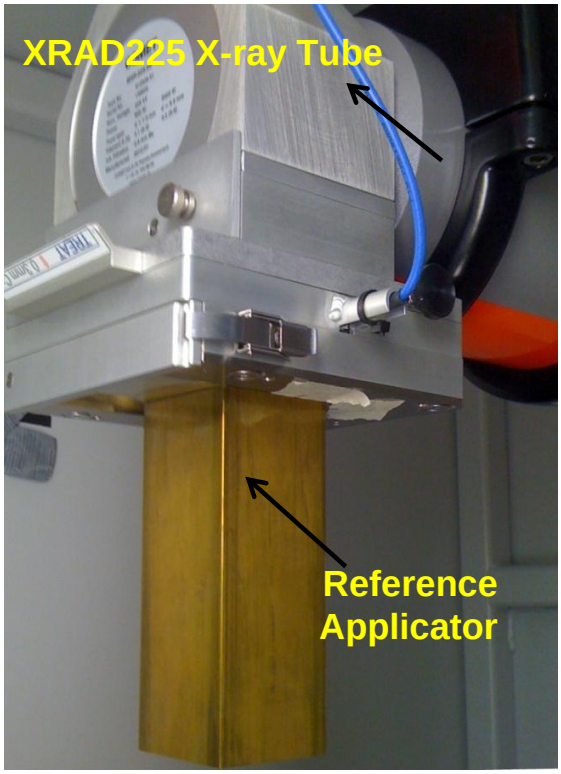

Figure 2.2: The MXR 225/22 x-ray tube inside the XRAD 225Cx irradiator enclosure

2.2.2 Collimation system

The collimation assembly, shown in Figure 2.1, consists of interchangeable applicators of various dimensions. The applicators ensure sharp penumbra and minimize out of field radiation transmission. The applicators are made of a high density (8.7 g/cm^3) brass and lead-bismuth alloy and feature seven standard circular field sizes (Figure 2.3) and four standard square field sizes (Figure 2.4) with specifications given in Table 2.2. The collimation system is mounted onto a bracket just beneath the x-ray tube.

XRAD 225Cx Collimating System	
Applicator Shape	Nominal Field Size Diameter at 30.5 cm SSD
Circular	1.0 mm 2.5 mm 3.5 mm 5.0 mm 10.0 mm 15.0 mm 20.0 mm
Applicator Shape	Nominal Field Size at 30.5 cm SSD
Square	10x10 mm^2 15x15 mm^2 20x20 mm^2 40x40 mm^2

Table 2.2: The XRAD 225Cx collimating systems specifications

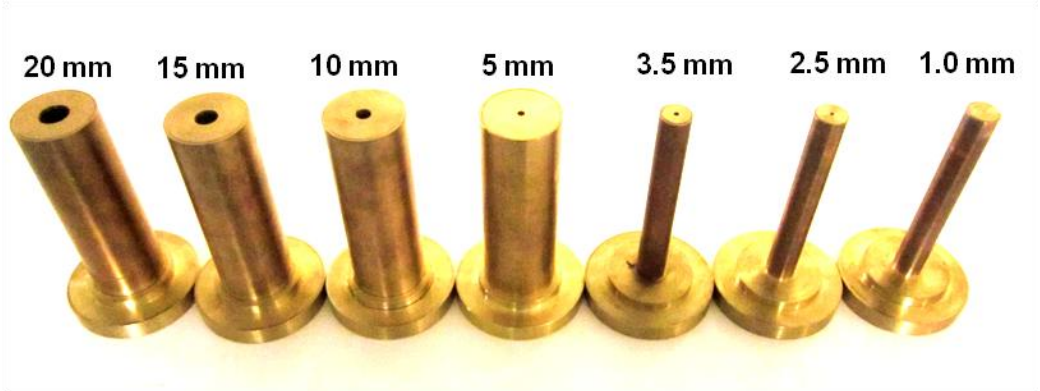

Figure 2.3: Circular field size applicators: left to right 20.0, 15.0, 10.0, 5.0, 3.5, 2.5 and 1.0 mm diameter.

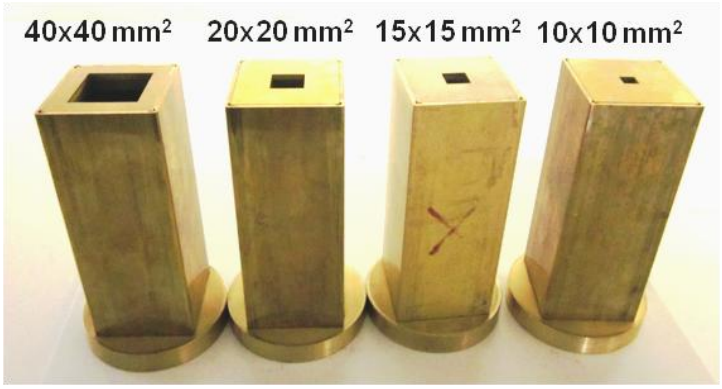

Figure 2.4: Square field size applicators: left to right 40x40, 20x20, 15x15 and 10x10 mm^2.

2.2.3 Gantry system and robotic couch

The XRAD 225Cx features a rotating c-arm gantry, fixed at the front by a stabilizing ring, which rotates about a motorized x-y-z (3D) translational stage, (Parker 404XE, Parker–Hannifin Corporation, Irwin, PA). The gantry provides the ability to image and treat over 360^o. The Parker HV23-02010 stepper motors are used to drive all three couch translational axes and the gantry.

The 3D stage and gantry are controlled by a 6k6 Parker Daedal multi-axis motion controller with position encoders on each translational axis and on the gantry system. The couch table top is composed of carbon fiber. The x-ray source is mounted on the C-arm inside the shielded enclosure. All sub-systems are enclosed within a self-shielded cabinet, and each stage is computer-driven utilizing the *Pilot* software provided by the manufacturer. The enclosure is equipped with two HD cameras, a 15x 20 cm^2 lead glass viewing window, and a duct for accessory cables, including a gas anesthesia tube. The gantry technical specifications are given Table 2.3.

Gantry and 3D Robotic Couch	
Stage and gantry manufacturer	Parker-Hannifin Corporation (Irwin, PA)
Controller	Parker Daedal 6k6 controller
x-y-z translational stage	404 XE
Motors for gantry and stage	HV 233-02-10 stepper motors
Range of rotation	360º
Stage positional accuracy	0.082 mm (Q)
Stage positional accuracy repeatability	0.020 mm (Q)

Table 2.3: The XRAD 225Cx gantry and x, y, z robotic couch specifications.
Q = specified by manufacturer

2.2.4 Image guidance system

The image guidance system (see Figure 2.1) consists of a digital imaging panel capable of radiography, fluoroscopy, and cone-beam CT (CBCT) by imaging while rotating the gantry. Image acquisition and animal positioning are performed under computer control. The imaging panel is mounted parallel to the x-ray source on the opposite side of c-arm. The imaging panel consists of an amorphous silicon flat panel detector (Perkin-Elmer, Wiesbaden, Germany). Imaging procedures are typically performed between 30 and 70 kVp with tube currents from 0.1 to 2.5 mA. Typical scan

times are 60 seconds for CBCT and 5 seconds for fluoroscopy. Compensation for gravitational gantry flex associated with c-arm 360º rotation is required for high resolution image and precise radiation delivery (Jaffray et al., 2002). This is achieved by first acquiring the x,y,z offsets between the imaging isocenter and center of the collimated beam for all gantry fields using a Winston-Lutz type-test (Lutz et al., 1988). Next, the offsets are recorded and uploaded to the stage controller so that the gantry flex is dynamically compensated during rotation. This procedure ensures the center of the treatment beam coincides with the desired targeted point for irradiation. These offsets are applied during treatment delivery and imaging. This methodology ensures precise dynamic radiation delivery while permitting both static and arc treatments (Clarkson et al., 2011).

The Pilot software controls the motorized x-y-z linear translation stage and gantry motion through the 6K6 controller, the x-ray beam and generator, and image acquisition and reconstruction. The raw CBCT projections are reconstructed using a Feldkamp-Davis-Kress (FDK) algorithm (Feldkamp et al., 1984). After acquiring a scout or high resolution CBCT scan, targeting is performed by selecting a point in the volumetric image set, i.e, the software will determine coordinates of target location relative to the isocenter. The stage is subsequently translated in three dimensions according to calculated shift. Once the desired location is attained, with the target centered on the isocenter, an appropriate irradiation protocol can be initiated with the controller moving the stage dynamically to irradiate to the target for all gantry positions. Image system characteristics, with typical image guidance parameters, are shown in Table 2.4.

Flat panel x-ray detector Manufacturer: Perkin Elmer (Wiesbaden, Germany)	
Model	Perkin Elmer XRD 0820 AN3 ES
Detector size	20x20 cm^2
Pixel matrix	1024x1024
Scintillation	CsI:TI
Maximum frame rate	15fps (30 fps @ 2x2 binning)
Pixel pitch	200 µm
Imaging parameters	
SAD, SDD	30.5 cm, 64.5 cm
CBCT acquisition parameters	
Tube potentials and currents	40 kVp, 2.5 mAs and 80 kVp, 0.3 mAs
Scan time	60 s
Angular range of projected views	360º
Frame rate used	7 fps
Number of projections per scan	438
CBCT reconstruction parameters	
Flood-field processing	Gain/offset correction
Reconstruction filter	Hamming
Voxel dimensions	(0.1x0.1x0.1) mm^3 to (1x1x1) mm^3

Table 2.4: The XRAD 225Cx image guidance system specifications

2.3 Characterization of beam quality and collimator transmission

As outlined by the TG-61 protocol, the determination of beam quality for orthovoltage energies is performed in two primary steps. The first is to obtain the air-kerma calibration factor N_K, as a function of tube potential and half-value layer (HVL), from a national standards lab. HVL is the thickness of copper attenuating material required to reduce the initial intensity by a factor of two. The second step is to measure the absorbed dose in the user's beam (Ma et al., 2001).

The air-kerma calibration coefficient for a PTW N31010 (0.125 cm^3) ionization chamber (PTW-New York Corporation, Hicksville, NY) was obtained for beam qualities M200 and M250 from the Accredited Dosimetry Calibration Laboratory (ADCL) at University of Wisconsin. The calibration certificate and an Excel spread sheet for absolute dose calibration is provided in appendix A.

The HVL measurement was performed in-air using a 20 mm diameter circular field size applicator with a pinpoint (N31014) ionization chamber placed 50 cm from the source. As the source is enclosed within a shielded housing, with an imaging panel opposite from the source at 64.5 cm SSD, the detector was placed at a distance of 58 cm, the maximum distance possible for narrow beam geometry. Thin sheets of copper were used to attenuate the beam to determine the HVL. The resulting HVL, at a tube potential of 225 kVp and tube current of 13 mAs, was measured to be 0.985 mm Cu (Figure 2.5-exponential fit). Transmission through the collimator was measured in air, at 30.5 cm SSD, using a pinpoint N31014 ionization chamber (PTW-New York Corporation, Hicksville, NY) by comparing the central axis readings for a 40x40 mm^2 square field size

to readings of a totally blocked field. The result was less than 0.1%.Treatment parameters for absolute dose calibration were given in Table 2.5

Treatment parameters	
Tube potentials and current	225 kVp,13 mAs
Source-to-Collimator Distance (SCD)	23.5 cm
Source-to-Surface Distance (SSD)	30.5 cm
Reference applicator	40x40 mm^2 square field size

Table 2.5 The treatment parameters used during absolute dose calibration

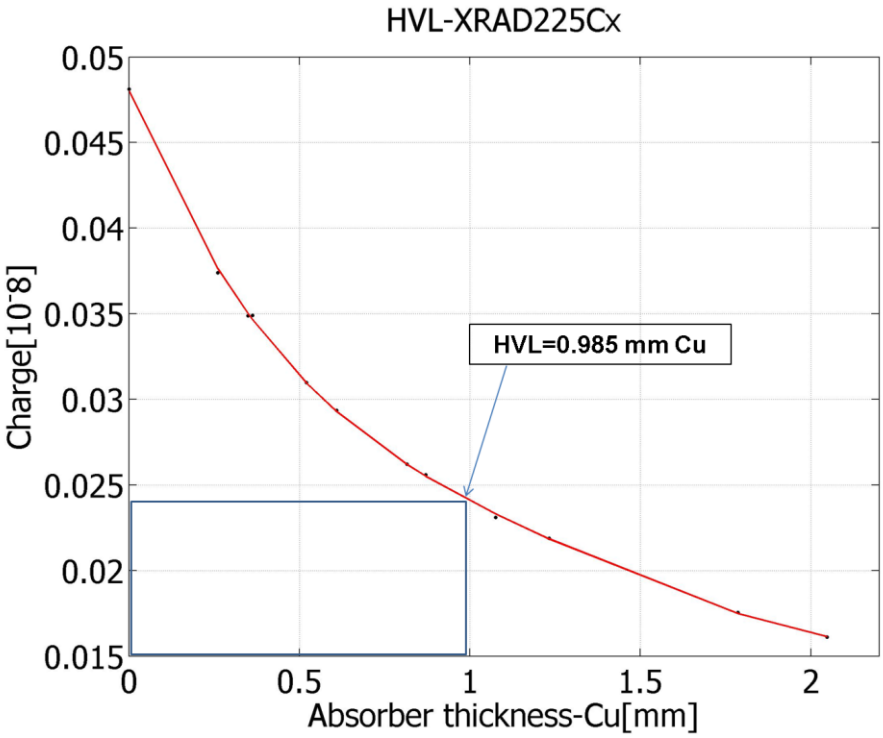

Figure 2.5: HVL measured using pinpoint chamber

2.4 Absolute dose calibration

Absolute dose calibration was performed in accordance with the recommendations specified in the AAPM TG-61 protocol (Ma et al., 2001). Both in-air and in-water calibrations were performed at a distance of 30.5 cm from the source, using the reference applicator (40x40 mm^2 square field size). For in-water measurements, the source-to-surface distance was set to 30.5 cm. The calibration setup is shown in Figure 2.6. A PTW N31014 pinpoint ionization chamber was used to measure the percent depth dose (PDD) in a water phantom, as the in-water calibration requires the PDD value at a reference depth of 2 cm. PDD data were measured for 30 s exposures at depths from 0 to 150 mm, using 1 mm increments for the first 10 mm and 5 mm steps for the remaining depths; the resulting PDD for the reference collimator are shown in Figure 2.7. The in-air method resulted in a dose rate of 3.454 Gy/min, while the in-water calibration measured at a 2 cm depth, projected back at the surface, yielded a dose rate of 3.420 Gy/min using PTW N31010 (0.125 cm^3) ionization chamber. The agreement between in-air and in-water calibration of 0.97% is excellent, particularly given the methodology is very dependent on an accurate PDD measurement.

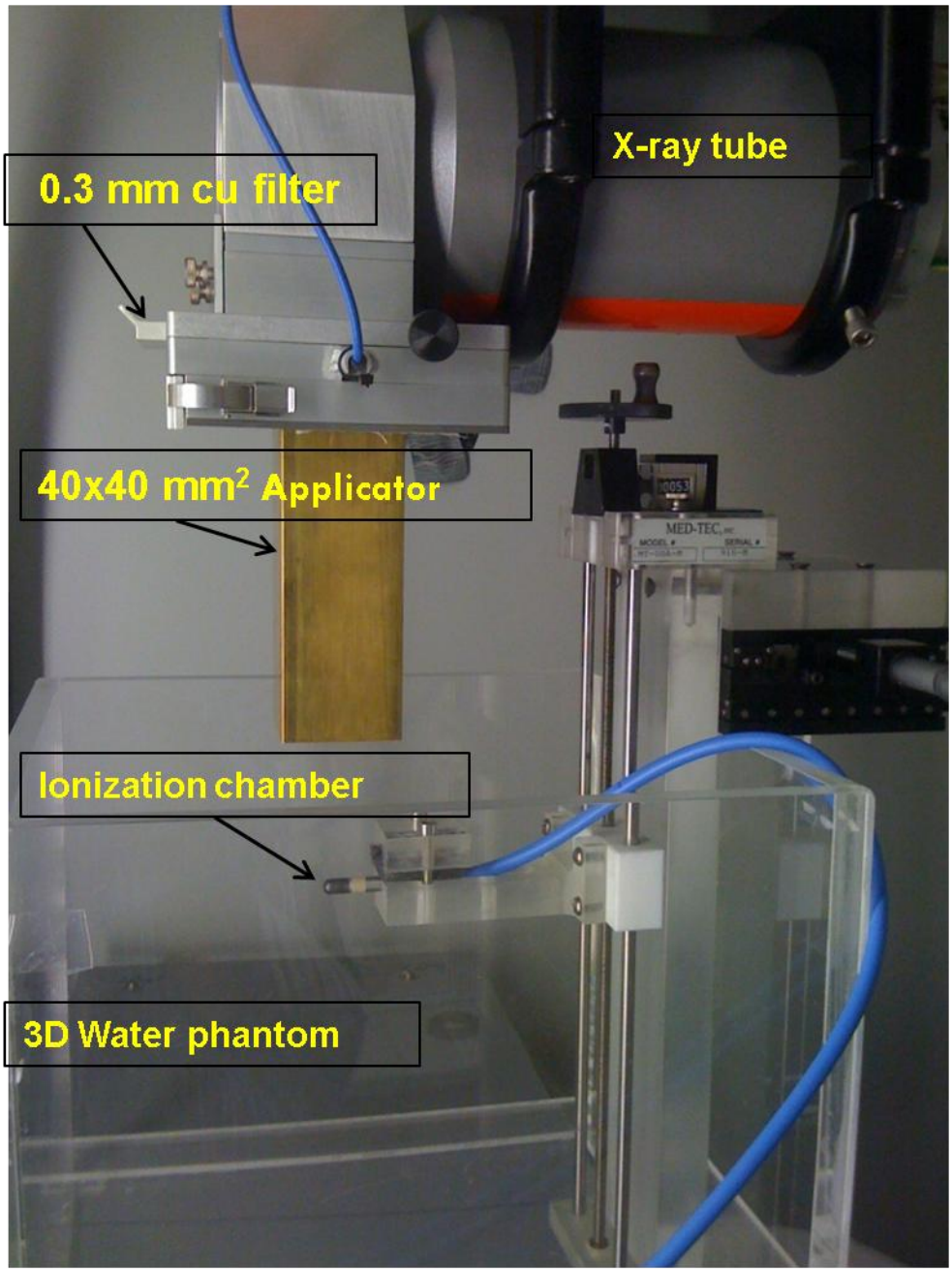

Figure 2.6: The XRAD 225Cx absolute dose calibration setup.

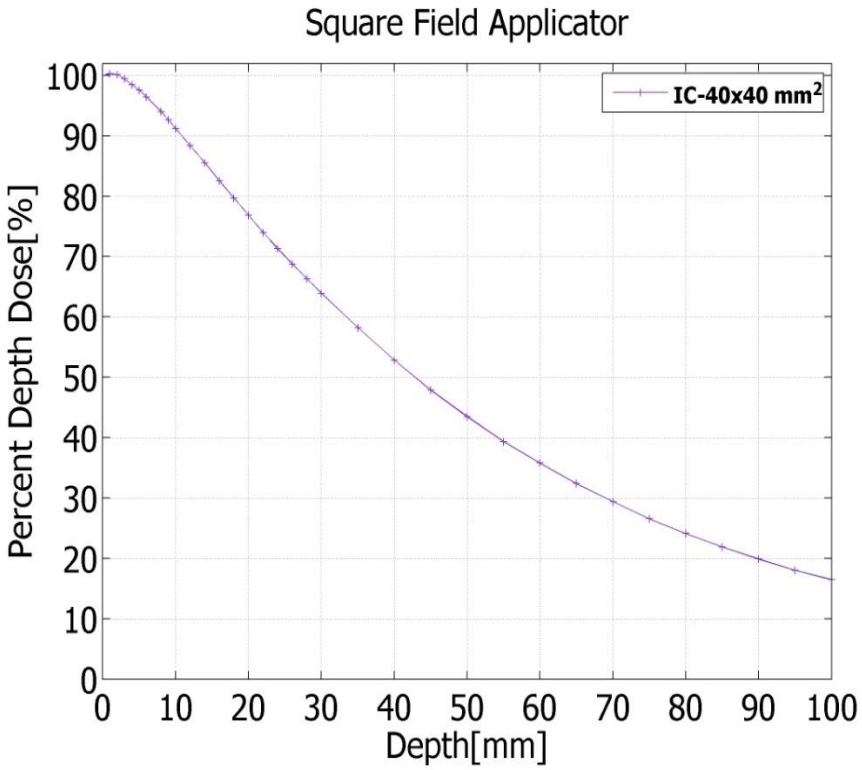

Figure 2.7: The percent depth dose (PDD) for the reference applicator (40x40 mm^2 square field size) measured using an ionization chamber (IC) at SSD of 30.5 cm.

2.5 Determination of film calibration curve

The sensitometric calibration curve was established by exposing EBT2 films to a known dose using the reference applicator and at 2 cm depth in solid water phantom (Gammex RMI, Middleton, WI). Each film was positioned perpendicular to the beam at 30.5 cm SSD and irradiated in dose increments of 5 s at 225kV,13mAs; a total of 32 calibration films were exposed. In turn, this HD calibration curve was used for all collimators to convert the measured optical densities to dose, in order to establish the PDD behavior relative to field size.

All Gafchromic EBT2 film analysis was performed 24 hours following exposure. The films were scanned using an Epson 1000XL scanner (Epson America Inc., Long Beach, CA) in 48-bit red-green-blue (RGB) mode, 16 bits per color, at 150 dpi resolution, and saved as tagged image file format (tiff) files. The EBT2 film manufacturer recommends using the red channel within the 0 to 8 Gy dose range. The scanned films were analyzed using a MatLab R2012a (Math Works, Natick, MA) code written specifically for this project. Only the red channel data was used in the analysis. Regions of interest selected in the central portion of each exposed film ranged from 40 x 40 pixels for the 20 mm diameter applicator, to 2 x 2 pixels for the smallest 1 mm diameter applicator. The net optical density was computed as:

$$netOD(D) = -\log_{10}\left(\frac{I_{exp}(D) - I_{bckg}}{I_{unexp} - I_{bckg}}\right) \qquad (2.1)$$

where $I_{exp}(D)$ and I_{unexp} are the readings for the exposed and unexposed film, and I_{bckg} is the reading for an opaque film, that is, the zero light transmitted intensity value. Standard deviations in the net optical density were computed following (Devic et al., 2005):

$$\sigma_{netOD} = \frac{1}{\ln 10}\sqrt{\frac{\sigma_{unexp}^2 + \sigma_{bckg}^2}{(I_{unexp} - I_{bckg})^2} + \frac{\sigma_{exp}^2 + \sigma_{bckg}^2}{(I_{exp} - I_{bckg})^2}} \tag{2.2}$$

The sensitometric orthovoltage calibration curve at 225kVp established by utilizing the reference collimator and exposing EBT2 films to a known dose at a depth of 2 cm in a 10 cm thick solid water block is shown in Figure 2.8. The error bars correspond to the uncertainty associated with the film scans and represent two standard deviations or 95.4% confidence level.

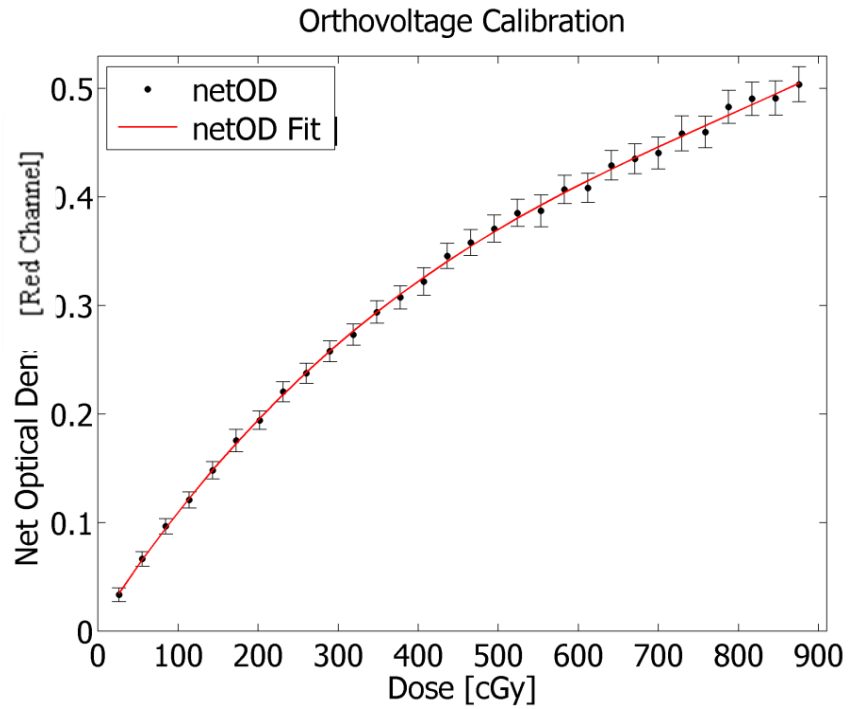

Figure 2.8: The sensitometric orthovoltage calibration curve; the error bars show 95.4% confidence level.

2.6 Dosimetric characteristics

2.6.1 Percent depth dose

Depth dose characteristics were measured using a pinpoint ionization chamber with dimensions (5mm horizontal length, 2mm vertical length) in water, and using Gafchromic EBT2 films in a solid water phantom. For all square and "larger" circular field sizes, i.e., greater than or equal to 10 mm diameter, a pinpoint ionization chamber was utilized using the same setup as described for absolute dose calibration, using an exposure time of 30 seconds at each depth between the water surface and a depth of 100 mm. For circular field sizes less than 10 mm in diameter, Gafchromic EBT2 films placed between thin solid water slabs and exposed for 60 seconds. Starting from top to bottom, the solid water phantom consists of eight 1 mm slabs, six 2 mm slabs, eight 3 mm slab, and eight 5 mm slabs. This setup results in a total of 31 films. The measurement depths were corrected for the average film thickness of 0.270 mm.

PDD data show the familiar relationship of increasing PDD value with increasing field size as shown in Figures 2.9 and 2.10 for square and circular applicators, respectively. For field sizes less than or equal to 10 mm, PDDs measured with EBT2 film are shown in Figure 2.11 - 2.14. Figure 15 shows PDD for a 10 mm diameter field size measured using both film and ionization chamber. The uncertainty in film measurement is shown in red error bars in Figure 2.15.

The film and ionization chamber PDD data agree within 2.3±1.4% on average. Depth dose characteristics, for example, 67.5% and 33.6% at depths of 20 and 50 mm, respectively, for the 10 mm diameter collimator at 30.5 cm SSD, provide more than adequate penetration for targeting deep-seated targets in small animals, particularly when

using multiple beam directions. As expected for orthovoltage energies, the maximum dose point occurs at the surface.

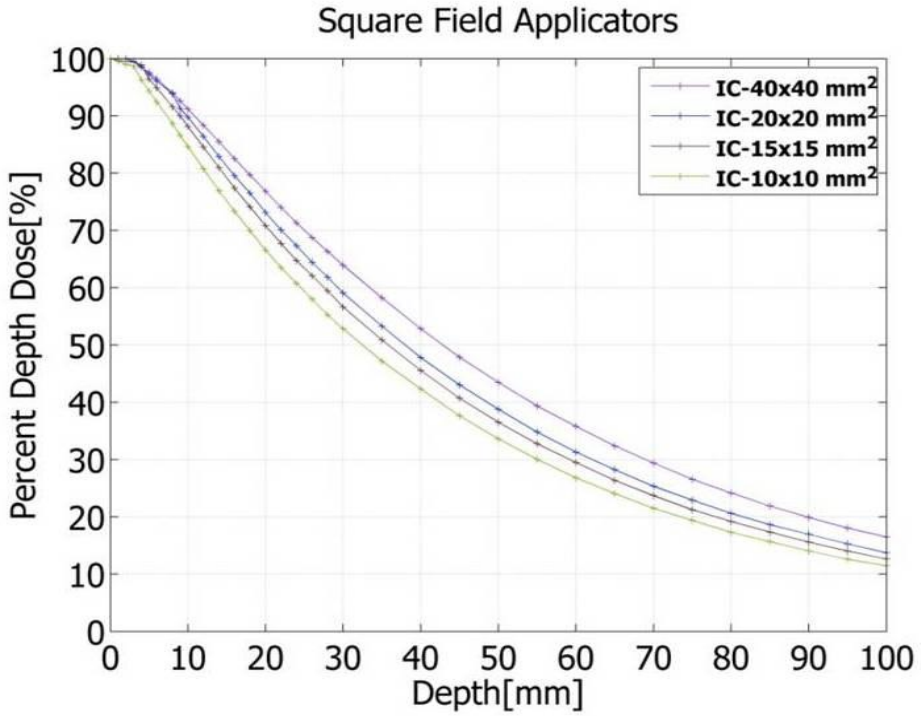

Figure 2.9: Percent depth dose at 30.5 cm SSD shown for 10x10, 15x15, 20x20 and 40x40 mm^2 square applicators measured using a pinpoint ionization chamber (IC).

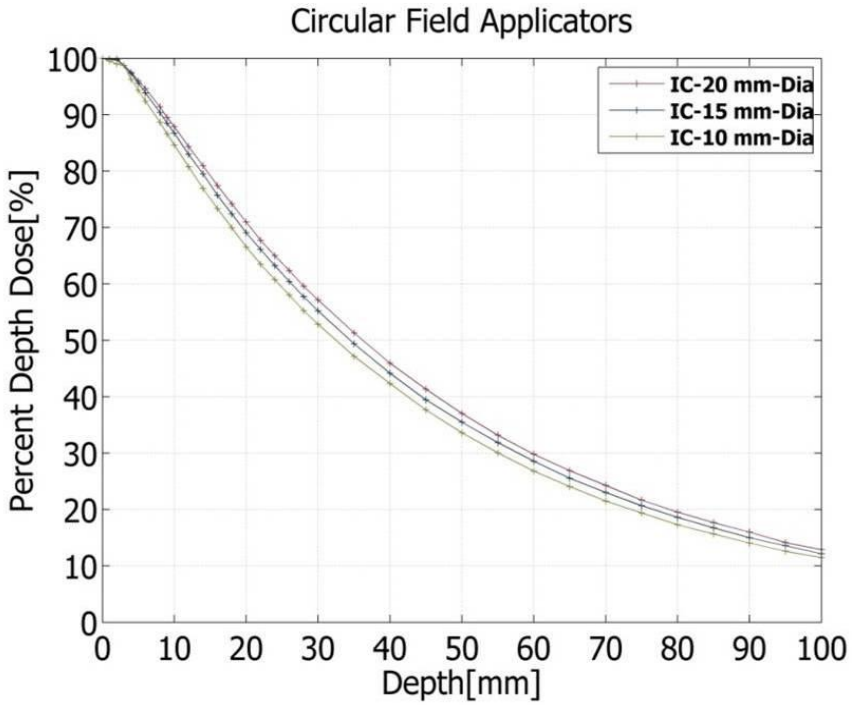

Figure 2.10: Percent depth dose at 30.5 cm SSD shown for 20, 15 and 10 mm diameter circular applicators measured using a pinpoint ionization chamber (IC).

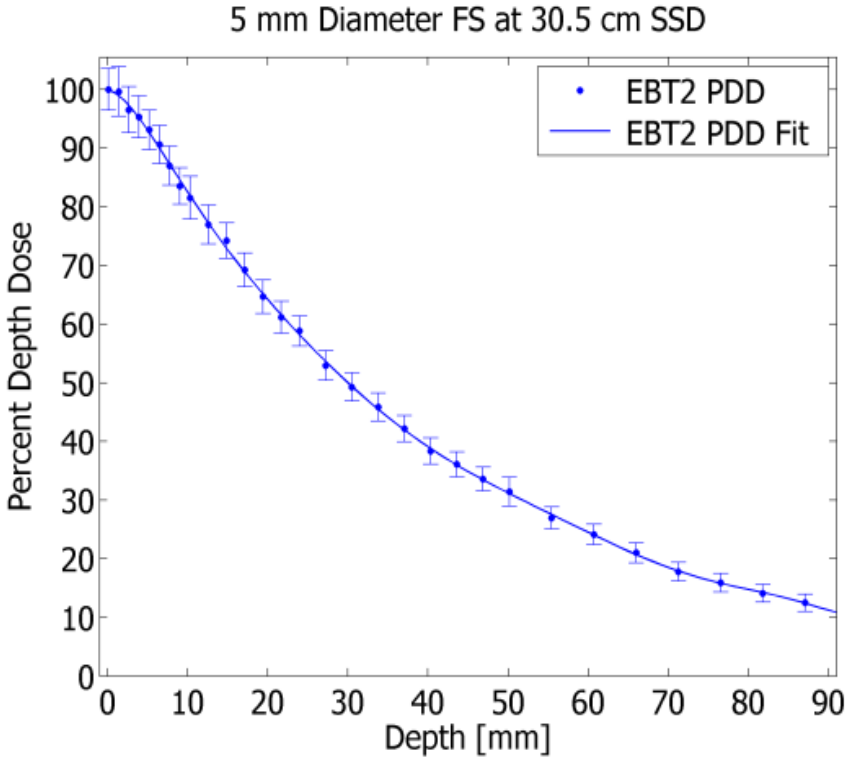

Figure 2.11: Percent depth dose at 30.5 cm SSD shown for 5.0 mm diameter circular field size applicator measured using Gafchromic EBT2 film.

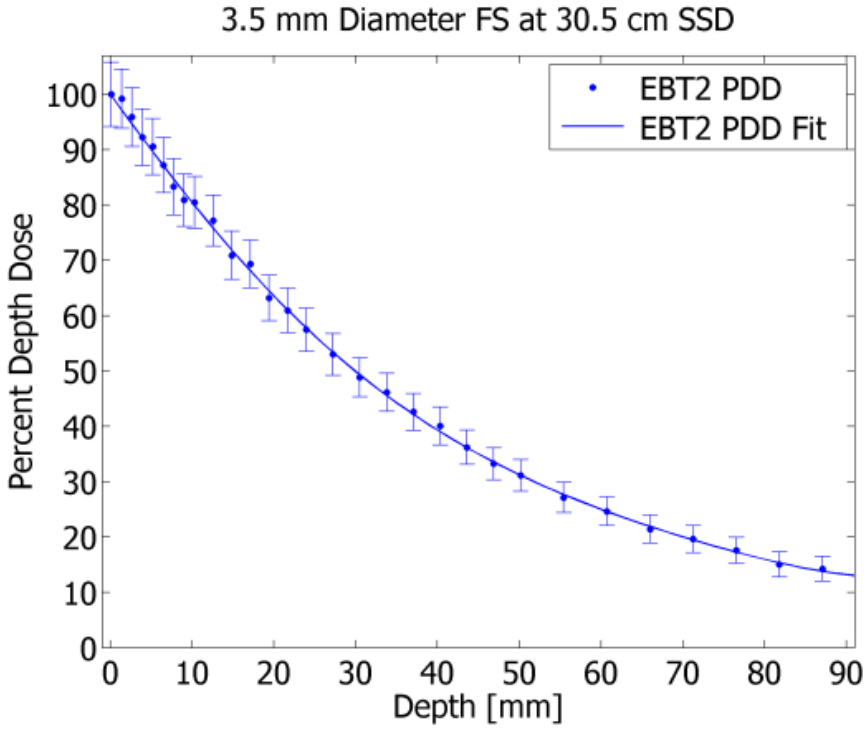

Figure 2.12: Percent depth dose at 30.5 cm SSD shown for 3.5 mm diameter circular field size applicator measured using Gafchromic EBT2 film.

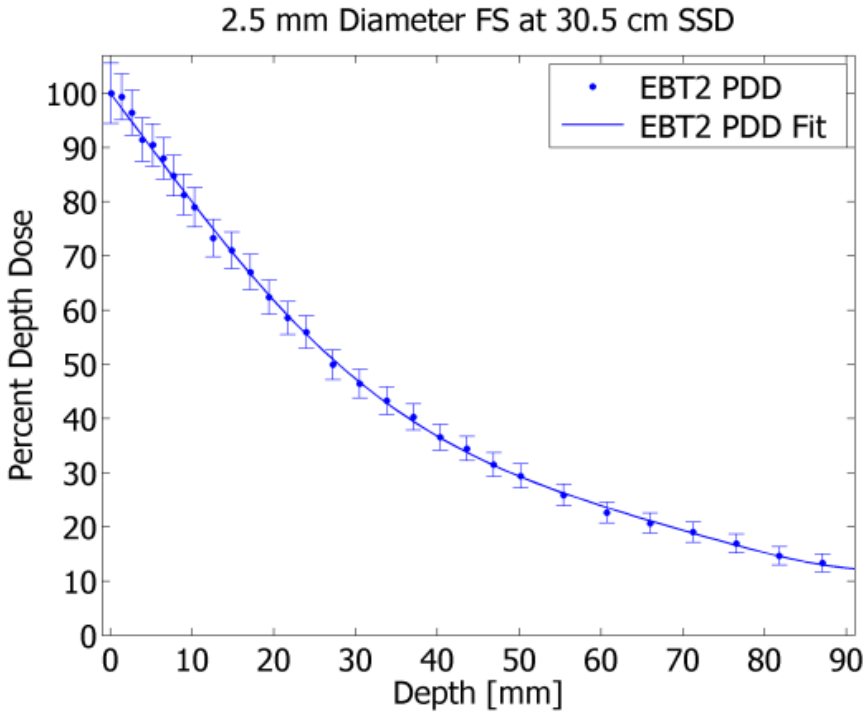

Figure 2.13: Percent depth dose at 30.5 cm SSD shown for 2.5 mm diameter circular field size applicator measured using Gafchromic EBT2 film.

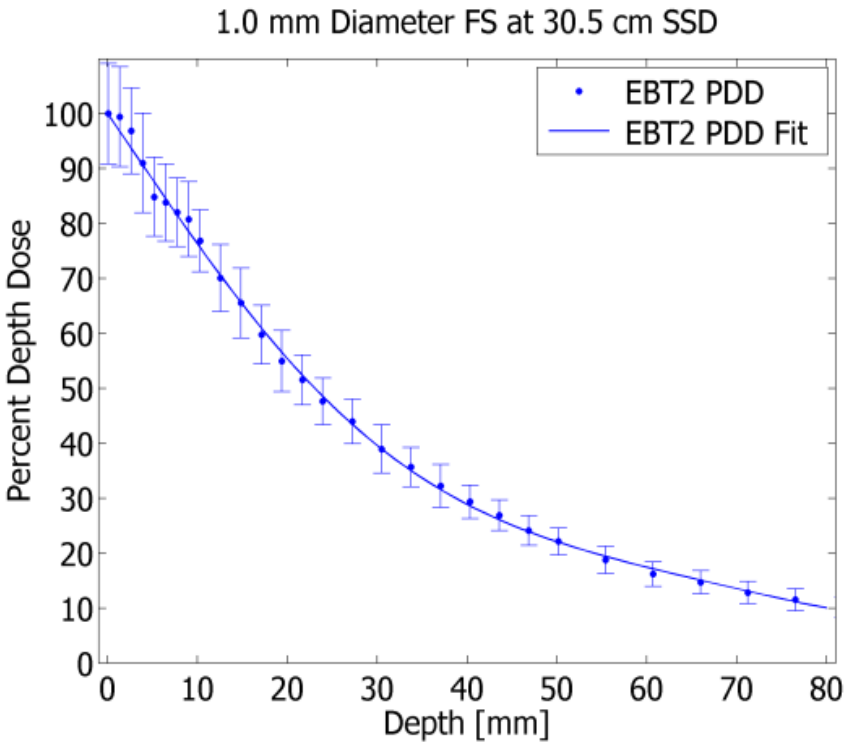

Figure 2.14: Percent depth dose at 30.5 cm SSD shown for 1.0 mm diameter circular field size applicator measured using Gafchromic EBT2 film.

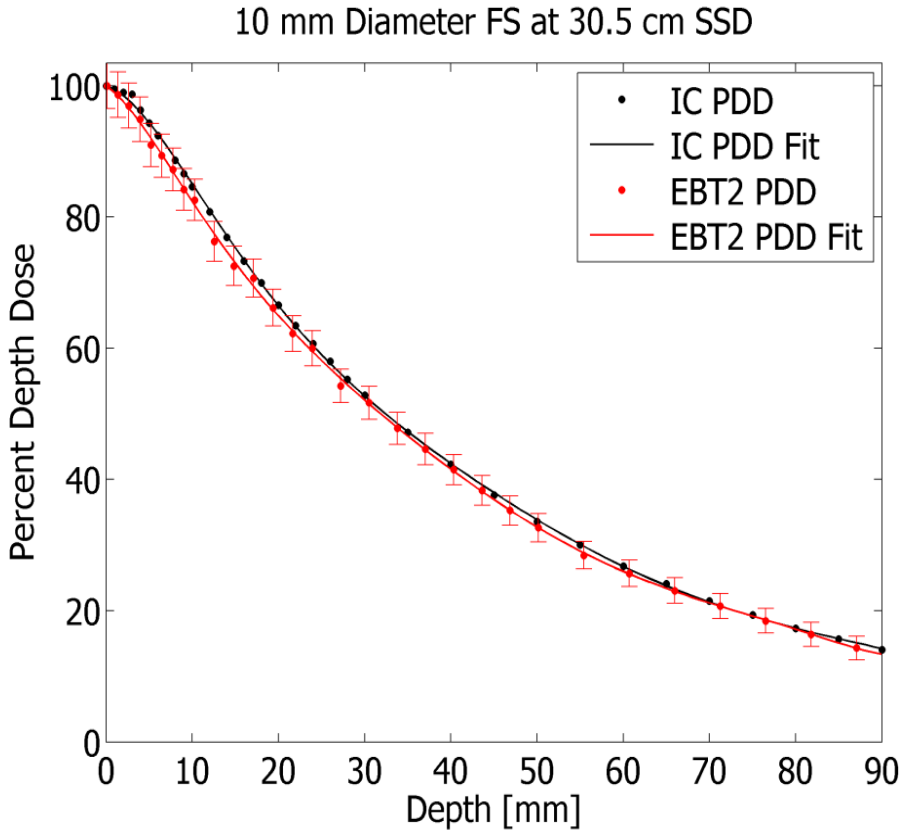

Figure 2.15: Percent depth dose at 30.5 cm SSD shown for the 10 mm circular applicator measured using Gafchromic EBT2 film and a pinpoint ionization chamber.

2.6.2 Total scatter factors

Total scatter factor, i.e, output factors, were determined relative to the 40 x40 mm^2 square field size collimator. For field sizes ≥ 10 mm, measurements were performed using a pinpoint PTW N31014 ionization chamber in a water phantom. For smaller collimators, the pinpoint detector size is comparable or larger than the collimator diameter, rendering the measurements unreliable for these field sizes. Therefore measurements were repeated using EBT2 film in a solid water phantom for all field sizes. Output factors were measured at depths of 2 cm and at the surface of the water or solid water phantom. Output factors are calculated from measurement using the following formula:

$$OF(fs,d) = \frac{D(fs,d)}{D(fs_{ref},d)} \tag{2.4}$$

where *fs* is the diameter [mm] of a circular field or side [mm] of a square field, d_{max} [cm] indicates the measurement depth in water with maximum dose, *D* is the dose [Gy], and fs_{ref} is 40x40 mm^2 field size applicator used as a reference field size. The results are shown in Tables 2.6, and 2.7. For each field size, output factors were compared between the two detectors and at two different depths. For a given depth, agreement is excellent between the two detectors. Due to uncertainties associated with surface measurements, better agreement is observed between film and ion chambers at 2 cm depth. Additionally, all measurement geometries were simulated using EGS Monte Carlo code; details of simulations are described in Chapter 3.

Total scatter factor (S_{cp}) with electron contamination							
Circular field applicators							
Dosimeter	20 mm	15 mm	10 mm	5 mm	3.5 mm	2.5 mm	1 mm
IC	0.924	0.910	0.887	----------NA----------			
Film	0.926	0.901	0.881	0.865	0.819	0.816	0.516
Difference (%)							
Film vs IC	0.27	-1.00	-0.59	----------NA----------			
Square field applicators							
Dosimeter	40x40 mm^2		20x20 mm^2		15x15 mm^2		10x10 mm^2
IC	1.00		0.944		0.924		0.896
Film	1.00		0.939		0.921		0.899
Difference (%)							
Film vs IC			-0.60		-0.31		0.37

Table 2.6: The total scatter factors relative to the 40x40 mm^2 square field size measured with a Gafchromic EBT2 film compared to pinpoint N31014 ionization chamber. Measurements were performed at a surface.

Total scatter factor (S_{cp}) without electron contamination							
Circular field applicators							
Dosimeter	20 mm	15 mm	10 mm	5 mm	3.5 mm	2.5 mm	1 mm
IC	0.833	0.793	0.742	----------NA----------			
Film	0.835	0.802	0.742	0.677	0.654	0.640	0.398
Difference (%)							
Film vs IC	0.26	1.10	-0.05	----------NA----------			
Square field applicators							
Dosimeter	40x40 mm^2		20x20 mm^2		15x15 mm^2		10x10 mm^2
IC	1.00		0.857		0.810		0.755
Film	1.00		0.864		0.817		0.754
Difference (%)							
Film vs IC			0.79		0.80		-0.13

Table 2.7: The total scatter factors relative to the 40x40 mm^2 square field size measured with a Gafchromic EBT2 film compared to pinpoint N31014 ionization chamber. Measurements were performed at a depth of 2 cm.

2.6.3 Off-axis ratios

Off-axis ratios (OARs) were measured using Gafchromic EBT2 film in solid water at a depth of 2 cm. OAR is calculated from the measurement using the following equation:

$$OAR = \left[\left[\frac{\text{dose (at off-axis distance)}}{\text{dose (at central axis)}} \right]_{\text{at given SSD}} \right] * 100 \qquad (2.5)$$

Penumbra, defined as a distance between 80% to 20 % dose, was determined from the resulting off axis profiles. Penumbra measured at 2 cm depth for a 30.5 cm SSD is shown in Table 2.9 as a function of field size. The corresponding off-axis ratios are plotted as function of distance in both in-plane and cross-plane directions in Figures 2.16 - 2.21.

The angled anode of the XRAD 225Cx produces an asymmetric beam in one direction (i.e., heel effect). Consequently, in contrast to linear accelerators used in radiotherapy, the beams produced are neither flat nor symmetric. Moreover, our smallest field size is 1 mm in diameter, for which typical flatness and symmetry specifications arguably do not apply.

Penumbra [mm] at 30.5 cm SSD		
Field size diameter [mm]	In-plane (y-axis)	Cross-plane (x-axis)
1.0	0.20	0.30
2.5	0.75	0.81
5.0	1.12	1.21
10.0	1.07	1.23
15.0	1.17	1.20
20.0	1.46	1.45
Square field size [mm^2]	In-plane (y-axis)	Cross-plane (x-axis)
40x40	2.18	2.14
20x20	1.77	1.80
15x15	1.64	1.20
10x10	1.09	1.40

Table 2.9: The 80%−20% beam penumbra along in-plane axis and cross-plane axis at 2 cm depth at 30.5 cm SSD.

For fields larger than 10 mm an intriguing discrepancy in IC and EBT2 film profile measurements was observed. As shown in Figure 2.22., the film profile beyond penumbra region is greater compared to that of pinpoint ionization chamber, with an average disagreement of 2.4%. In contrast, the inner beam region of the profile agrees on average within 0.1%. We hypothesize that the low energy scattered photons cause an increased response of the film relative to the open field response in the dose in the tails of the profiles. To validate this argument, Monte Carlo simulations were performed and compared against measurement with IC and film. The detailed analysis of simulation and comparisons is described in chapter 3. The average dose error is within +/-3% for 10 mm dose profile across 3.5 mm from the central axis.

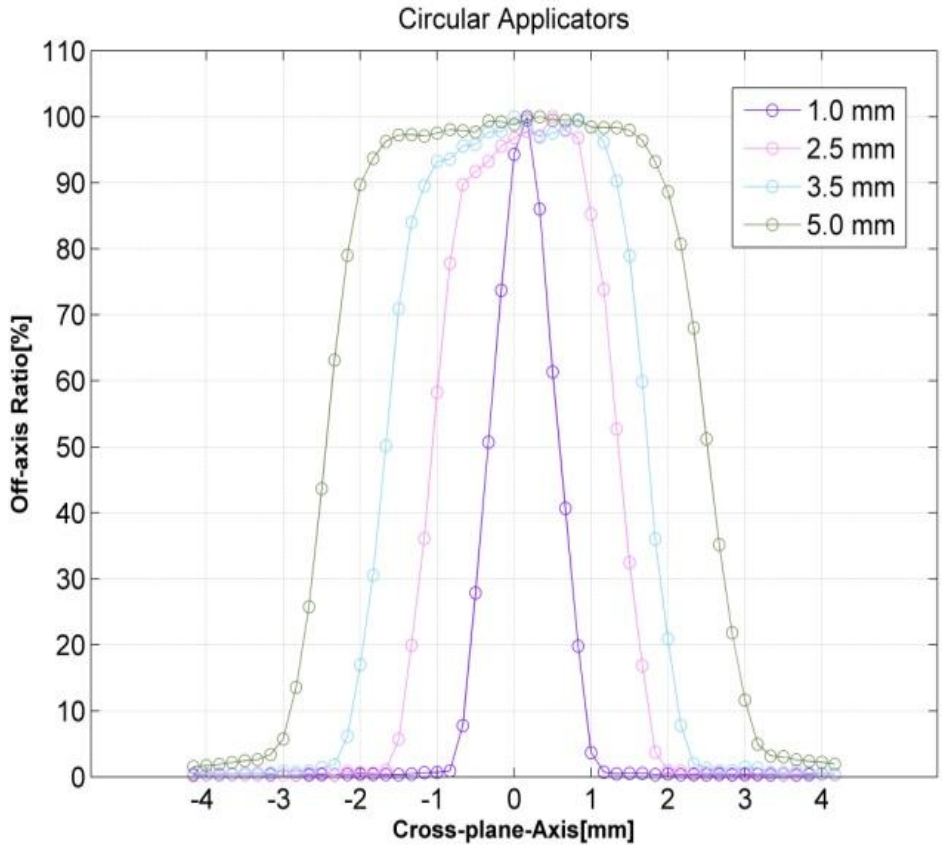

Figure 2.16: Off-axis ratio as a function of the distance along the Cross-plane axis for 1.0, 2.5, 3.5 and 5.0 mm diameter circular field sizes measured with EBT2 film at a 2 cm depth.

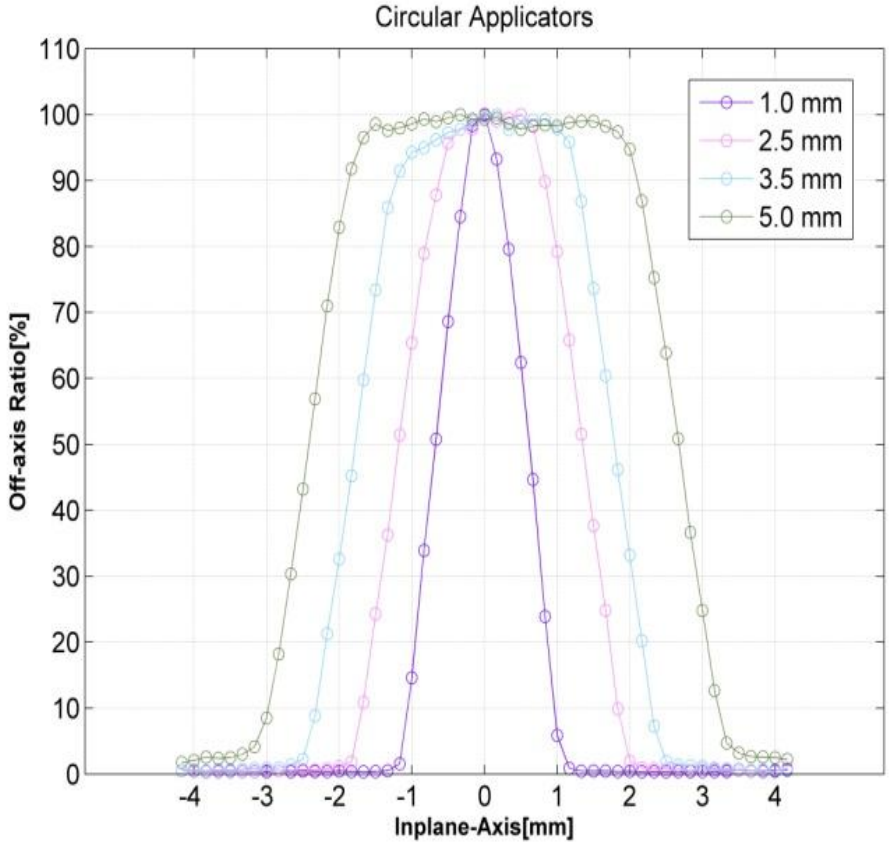

Figure 2.17: Off-axis ratio as a function of the distance along the In-plane axis for 1.0, 2.5, 3.5 and 5.0 mm diameter circular field sizes measured with EBT2 film at 2 cm depth.

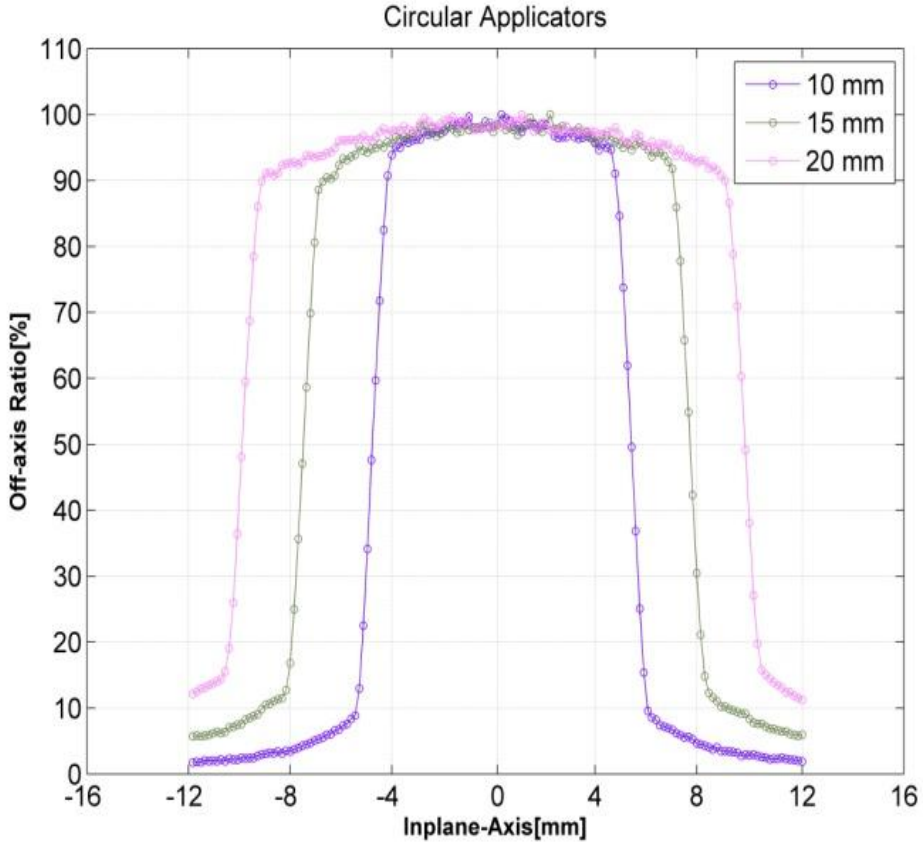

Figure 2.18: Off-axis ratio as a function of the distance along the In-plane axis for 10.0, 15.0, and 20.0 mm diameter circular field sizes measured with EBT2 film at 2 cm depth.

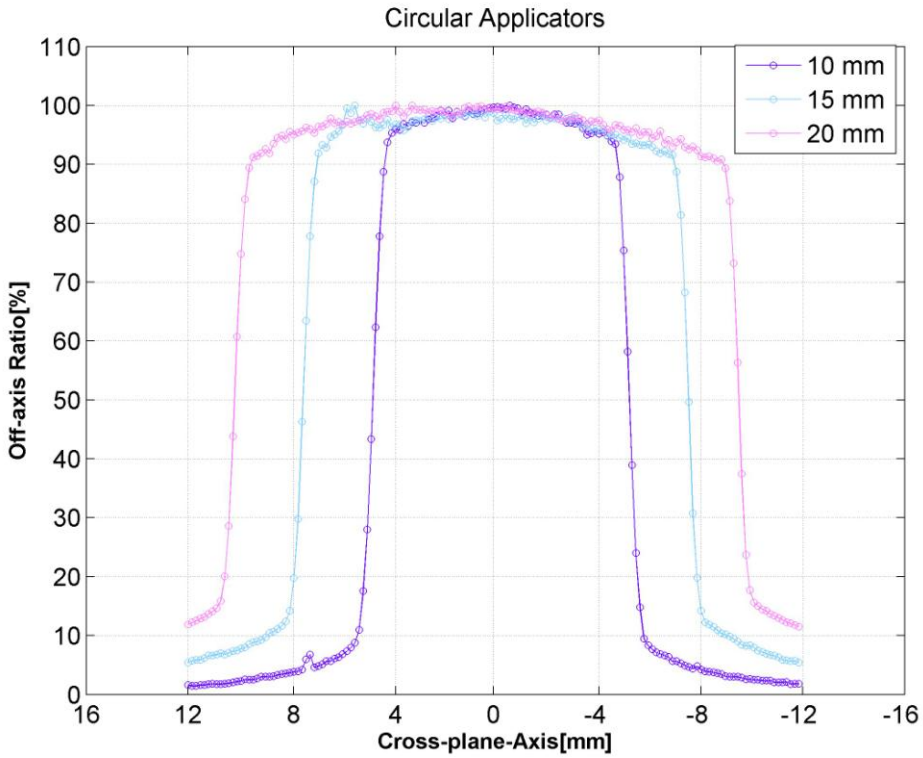

Figure 2.19: Off-axis ratio as a function of the distance along the Cross-plane axis for 10.0, 15.0, and 20.0 mm diameter circular field sizes measured with EBT2 film at 2 cm depth

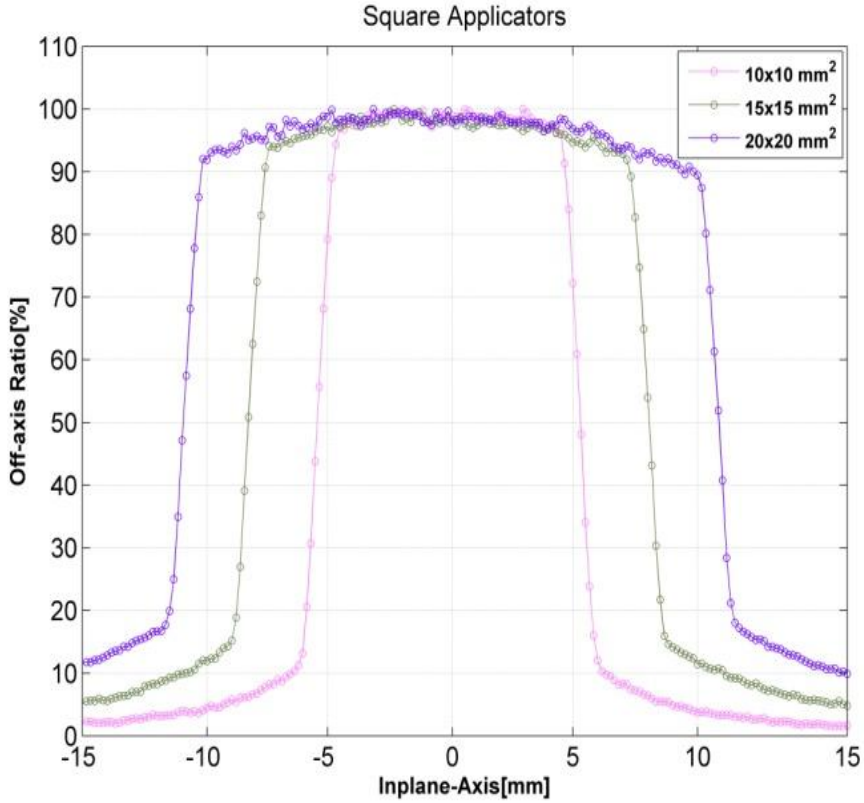

Figure 2.20: Off-axis ratio as a function of the distance along the In-plane axis for 10x10 mm^2, 15x15 mm^2, and 20x20 mm^2 square field sizes measured with EBT2 film at 2 cm depth

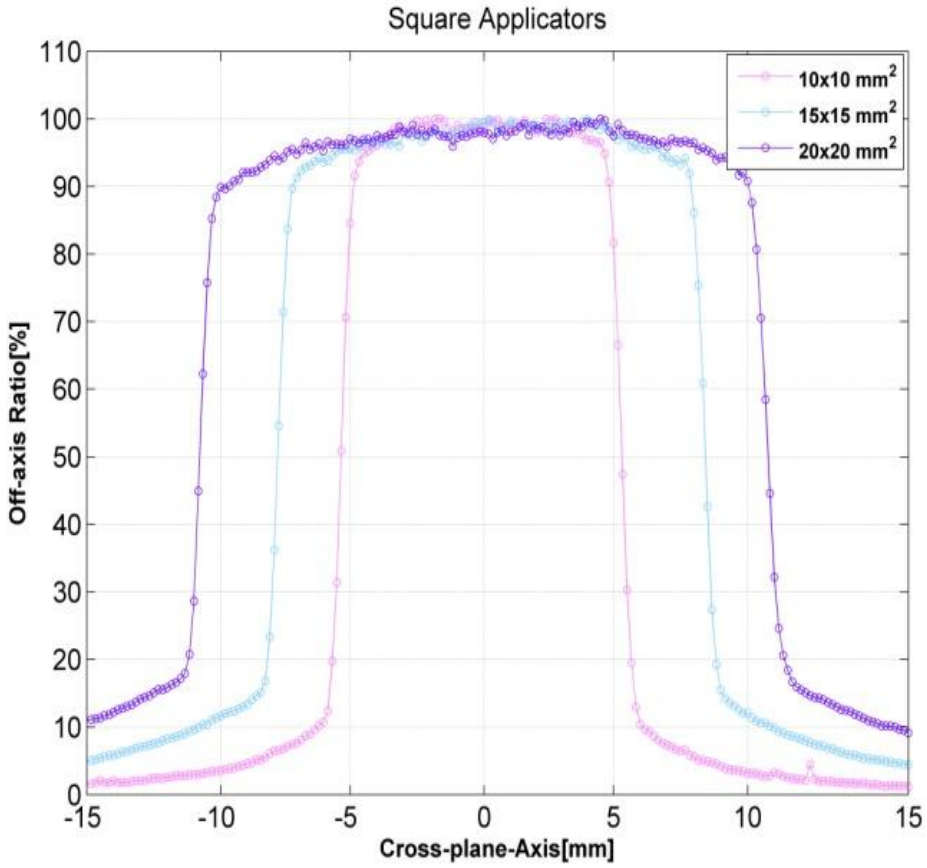

Figure 2.21: Off-axis ratio as a function of the distance along the Cross-plane axis for 10x10 mm^2, 15x15 mm^2, and 20x20 mm^2 square field sizes measured with EBT2 film at 2 cm depth

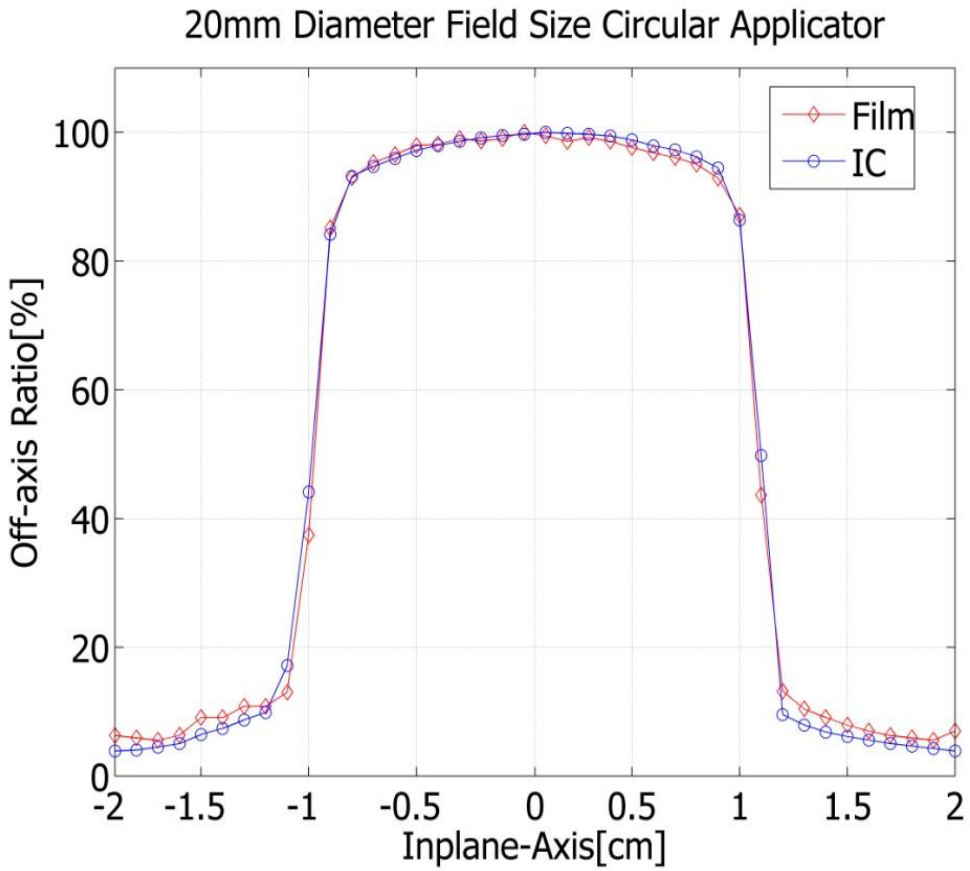

Figure 2.22: Off-axis ratio as a function of the distance along the cross-plane measured using EBT2 film and pinpoint ionization chamber for 20 mm field size applicator at a depth of 2cm.

2.6.4. End effect

For treatment planning purposes beams are scanned and modeled as measured. As a result of the time delay required to switch the beam “ON” and “OFF” in an x-ray unit, however, a timer correction (also referred to as the "end effect") is required to accurately calculate the dose. The correction is determined by measuring the charge with ionization chamber with varying time settings. The data is fitted with first degree polynomial. Using the graphical extrapolation method, the end effect was determined to be 0.5833 s as represented by the intercept of the regression line on the time axis in Figure 2.23.

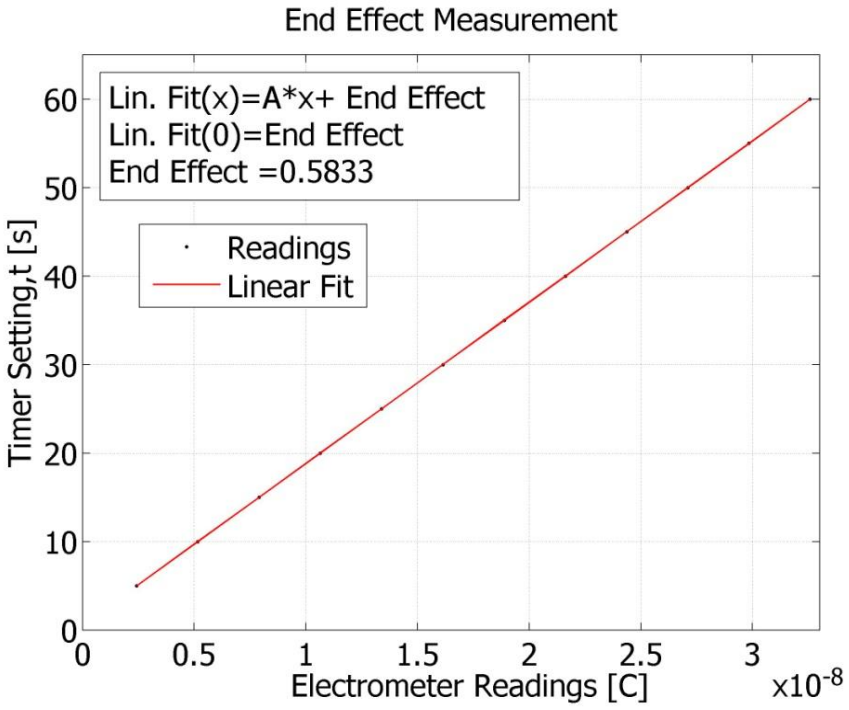

Figure 2.23: The timer error of x-ray unit was determined graphically as the intercept of the regression line on the time axis.

2.6.3 Dose linearity with tube current

The ability to vary mAs in a linear manner is essential to obtaining finer dose increments. To determine beam intensity as a function of tube current, a pinpoint chamber was exposed at the surface of a water phantom using the reference collimator. Tube potential and time were held constant at 225 kVp and 30 seconds while varying the tube current from 1 to 13 mAs in 1 mAs increments (Figure 2.24). Consequently, doubling the current at constant exposure time has the same effect as doubling the exposure time at constant tube current.

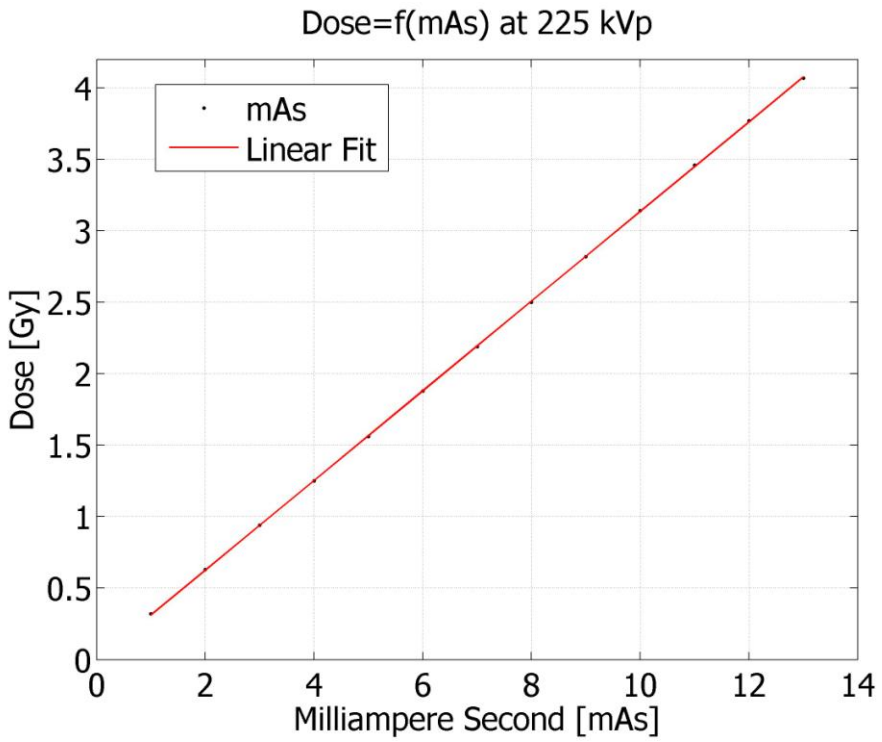

Figure 2.24: The linear relationship between x-ray beam intensity and the tube current.

References

CLARKSON, R., LINDSAY, P. E., ANSELL, S., WILSON, G., JELVEH, S., HILL, R. P. & JAFFRAY, D. A. 2011. Characterization of image quality and image-guidance performance of a preclinical microirradiator. *Medical Physics,* 38, 845-856.

DEVIC, S., SEUNTJENS, J., SHAM, E., PODGORSAK, E. B., SCHMIDTLEIN, C. R., KIROV, A. S. & SOARES, C. G. 2005. Precise radiochromic film dosimetry using a flat-bed document scanner. *Med. Phy.,* 32, 2245-2253.

FELDKAMP, L. A., DAVIS, L. C. & KRESS, J. W. 1984. Practical cone-beam algorithm. *J. Opt. Soc. Am. A,* 1, 612–619.

JAFFRAY, D. A., SIEWERDSEN, J. H., WONG, J. W. & MARTINEZ, A. A. 2002. Flat-panel cone-beam computed tomography for image-guided radiation therapy. *International journal of radiation oncology, biology, physics,* 53, 1337-1349.

LUTZ, W., WINSTON, K. R. & MALEKI, N. 1988. A system for stereotactic radiosurgery with a linear accelerator. *International journal of radiation oncology, biology, physics,* 14, 373-381.

MA, C. M., COFFEY, C. W., DEWERD, L. A., LIU, C., NATH, R., SELTZER, S. M. & SEUNTJENS, J. P. 2001. AAPM protocol for 40-300 kV x-ray beam dosimetry in radiotherapy and radiobiology. *Med Phys,* 28, 868-93.

CHAPTER THREE

A Monte Carlo Source Model of the XRAD 225Cx irradiator

3.1 Introduction: Monte Carlo Method

Monte Carlo approaches to radiation transport in medical radiation dosimetry provide a numerical solution to the Boltzmann transport equation by employing fundamental physical laws of electron-atom and photon–atom interactions. Individual particle tracks are faithfully reproduced within the physical laws, incorporating 1) scattering and 2) absorption cross sections. By transporting millions, or billions of individual particles, individual "solutions" concerning each particle are obtained. This process is a statistical method of "random sampling" (Bielajew, 2006). The Central Limit Theorem states that as the number of the individual solutions for each particle increases and approaches infinity, the average of all solutions approaches an expected value for the problem, hence a solution to Boltzmann Equation (Bielajew, 2006, Lindeberg, 1922, Feller, 1967). Monte Carlo simulation requires the user to provide detailed information regarding each particle transported, including 1) particle type, 2) initial position, 3) particle direction and energy, and 4) an exact geometry with different material atomic compositions and densities.

Monte Carlo codes often used in radiation therapy include EGSnrc, MCNPX, DPM, Penelope and VMC++ (Briesmeister, 2000, Nelson et al., 1985, Sempau et al., 2000, Salvat, 2001). The various codes differ in a number of ways, including how they handle the creation of secondary electrons. In a class I algorithm (e.g., MCNPX), the energy and direction of the primary electrons are not affected by secondary particle

creation, and angular deflections and energy losses are grouped together. In a class II algorithm (e.g., EGS), the energy of the primary electron is directly correlated to that of the secondary electron, and the primary electron's direction is also affected by the creation of knock-on electrons (delta rays) (Jenkins et al., 1988). In the creation of secondary photons, both MCNPX and EGS use a class II algorithm. Despite the differences in electron transport, these codes have achieved a similar level of acceptance in radiation transport applications. The MCNP package is repeatedly chosen based on its robust geometry package, but its inherent limitation of adaptation and flexibility comes at the cost of increase CPU time (Mainegra-Hing and Kawrakow, 2006). In this work, the EGSnrc Monte Carlo code is chosen over MCPNX due to certain advantages expressed in medical physics applications, i.e., the variety of user codes available for routine design that allow users to address many issues without writing alternate code, as well as improvements in low energy cross section data related to differential Bremsstrahlung and Rayleigh scattering.

3.2 Geometric Model in Monte Carlo

In this work, the BEAM/EGS coupled photon-electron transport code was used to simulate a 225 kVp photon beam from the XRAD 225Cx system. BEAM is a package of codes originally used for building accelerator geometries and for evaluating results of radiation transport simulations (Rogers et al., 1995, Nelson et al., 1985). The virtual geometry and material composition of the XRAD 225Cx components in the simulation are based on the manufacturers' specifications. An image of the x-ray tube head is shown in Figure 3.1A. The component module (CM) in the BEAMnrc is designed to aid in the creation of virtual geometries. Several CMs were used to model structures for the XRAD 225Cx and are shown in Figure 3.1B. The anode target, using a focal spot dimension of 3.54 mm wide by 2.94 mm in length as provided by manufacturer, was defined using a CM called XTUBE. Filtration materials, representing inherent beryllium and copper filtration, were defined as CM SLABS. The primary collimator was constructed using a CM called PYRAMID and the monitor chamber was constructed using a CM called CHAMBER. Reference collimators, along with intermediate inserts, were constructed with a CM called PYRAMID or CIRCAP. A CM, CHAMBER as PHANTOM, was used to score the dose in a water medium. In all MC simulations, updated BEAMnrc material cross-section data were used for more accurate photon and electron transport (Kawrakow et al., 2011). In the MXR225 tube, the x-ray generating target is constructed of 2 mm tungsten with an anode angle of 20° and an inherent beryllium filtration. Lead and lead bismuth alloy collimators were used for both shielding and for defining the beam. The primary collimator is off center to the beam axis to avoid radiation damage to the imaging panel electronics.

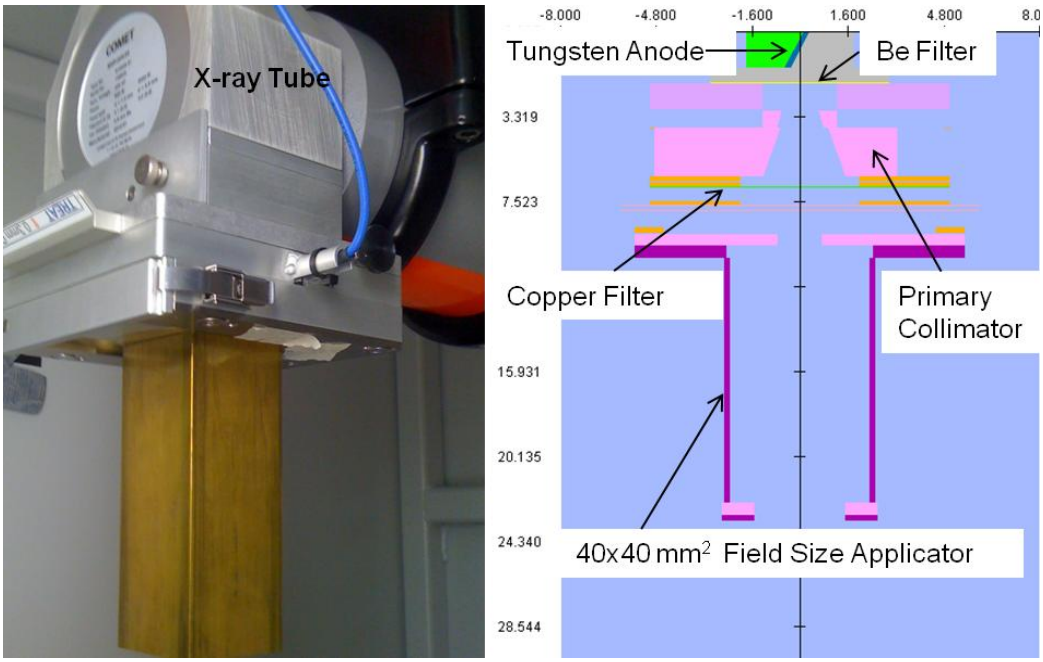

A B

Figure 3.1 A: The x-ray therapy system inside the XRAD 225Cx irradiator enclosure.
Figure 3.1 B: Monte Carlo geometric model of the components of the x-ray tube as used to generate the 225 kV photon beam. All dimensions are in centimeters. Values on the figures distances from the central axis to the inner edges of the openings, for both *x* and *y* collimators and have 0.01 cm uncertainty.

3.3 Variance Reduction Technique

Variance reduction techniques are commonly used to increase the precision of the uncertainty that can be obtained for a given number of histories without introducing statistical bias. Bremsstrahlung production in the orthovoltage energy range is very inefficient process (Mainegra-Hing and Kawrakow, 2006), and therefore to achieve meaningful results in a reasonable time frame, use of variance reduction techniques is necessary. The gain in efficiency (ε) of a particular technique in Monte Carlo calculation is estimated using

$$\varepsilon = \frac{1}{\sigma^2 T} \tag{3.1}$$

where σ is an estimate of the variance quantity of interest and T is CPU time (s) required to obtain this variance. From this equation, one can estimate the efficiency and number of histories required to achieve the desired variance. To save computing time and enhance the efficiency of the Bremsstrahlung production in the target, a variance reduction technique known as Directional Bremsstrahlung Splitting (DBS) was invoked in the simulation process (Kawrakow et al., 2004). This is a "particle splitting" technique which increases the number of Bremsstrahlung photons in the simulation geometry.

In DBS, we define circular area at a specific source to surface distance (SSD), such that all photons inside the circular target field are assigned a weight of 1/ N, and all photons outside are assigned a weight of 1. Those with weight of 1 are discarded.

At each Bremsstrahlung interaction site on the target, N photons are sampled individually and their weights are reduced by a factor of 1/N. The split photons are transported towards the defined field of radius; photons not transported towards the circular area are

subjected to a Russian roulette process, so whereby to ensure an unbiased result, the weight of the surviving particles is increased by the inverse of the probability. This ensures an unbiased result.

For our simulation, the user defined optimum splitting number 'N' was extrapolated ($3.5x10^5$) from published data for 225 kVp photons (Mainegra-Hing and Kawrakow, 2006), to maximize the efficiency and to save a significant amount of computing time. Each time an electron is about to create a Bremsstrahlung photon, the energy and direction of $3.5x10^5$ bremsstrahlung photons are actually sampled from the appropriate probability distributions and their weight is reduced accordingly. We use a DBS splitting radius of 5 cm at 30.5 cm SSD to ensure that generated photons cover the largest possible field size. In the second stage of the simulation, the particles are transported without DBS.

3.4 Virtual Source

Photons emerging from the target pass through various components of the collimating system and are scored in a virtual source in a plane perpendicular to the central ray of the beam at a specified distance from the x-ray target..

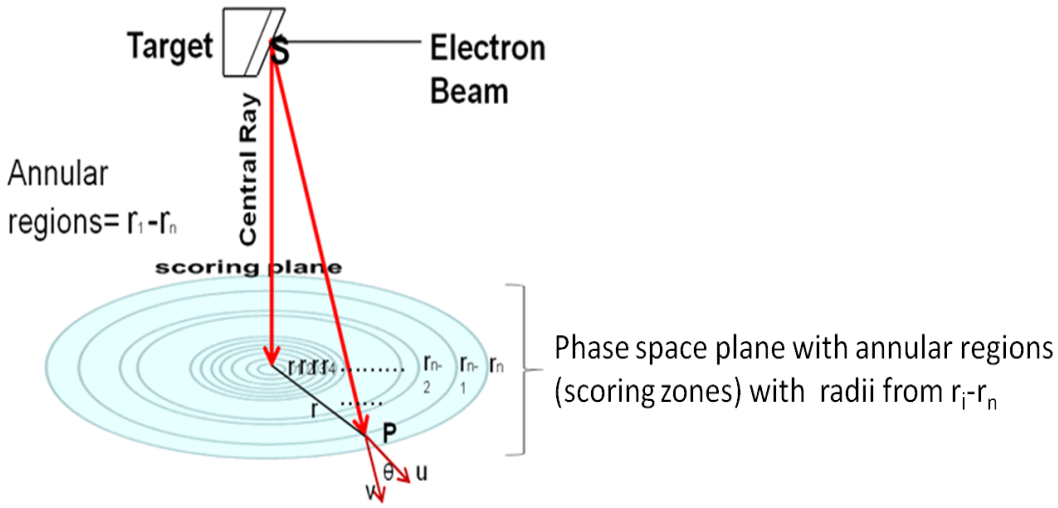

Figure 3.2: Scoring of energy spectrum and angular distribution.

The plane is divided into annular regions around the central ray as shown in Figure 3.2. For each annular region, the number of photons within each energy interval crossing the plane of interest is recorded. The i^{th} annulus corresponds to the space between radii r_{i-1} and r_i in Figure 3.2. Angular distributions are recorded over the entire plane as a function of the angle between two vectors ***u*** and ***v***, where vector ***v*** joins the source with the point of observation and vector ***u*** defines the direction of the photon. For each observation point P the direction of ***u*** describes the angular distribution of photons relative to ***v***. These data yield the angular spread at the point of observation relative to the initial direction of incidence and describe the spreading of fluence profile boundaries as a function of the

distance from the collimating system (Jenkins et al., 1988). These data are used to compute dosimetric characteristics. For example, by bombarding a target with $8x10^8$ mono-energetic electrons, a phase space file containing $6x10^8$ photons was created at the end of a 10x10 mm^2 square field applicator. The goal of each simulation is to obtain dosimetric results with low uncertainties. The number of particles in the phase space file, however, may be smaller than the number of histories required for achieving the desired uncertainty. In order to improve the statistics of the final dose calculation, oversampling or "recycling" of the particles in the phase space file is customarily performed. While this can create a source of systematic error (dose uncertainty <3%), a low recycling rate (<27 times) does not introduce observable statistical artifacts in the dose calculations (Walters et al., 2002). The dimensions of the annular regions and the total number of photons detected by each detector ring (per starting particle, per cm^2) are dependent on the field size of the applicator at its isocenter. Each scoring zone or annular region counts all incident photons and sorts them into an energy bin. For each applicator the annular regions were modified in order to appropriately score the resulting particles. Appropriate scoring zone radii for each field size are selected based on their respective beam exit. Table 3.1 shows entrance and exit dimensions for each applicator.

Field size diameter at isocenter	Applicator entrance aperture diameter	Applicator exit aperture diameter
1.0 mm	3.0 mm	0.75 mm
2.5 mm	3.0 mm	1.90 mm
3.5 mm	3.0 mm	2.70 mm
5.0 mm	9.9 mm	3.85 mm
10.0 mm	9.9 mm	7.60 mm
15.0 mm	9.9 mm	11.5 mm
20.0 mm	9.9 mm	15.0 mm
Field size at isocenter	Applicator entrance aperture dimensions	Applicator exit aperture dimensions
10x10 mm^2	12.5 mm x 12.5 mm	7.60 mm x 7.60 mm
15x15 mm^2	12.5 mm x 12.5 mm	11.6 mm x 11.6 mm
20x20 mm^2	12.5 mm x 12.5 mm	15.5 mm x 15.5 mm
40x40 mm^2	15.5 mm x 15.5 mm	30.0 mm x 30.0 mm

Table 3.1: List of the entrance and exit apertures for circular and square applicators that are measured and modeled in BEAMnrc. The entrance and exit apertures are located at a distance of 9.08 cm and 23.5 cm from the source, respectively.

Each phase space plane (phsp) is located at the end of the applicator CM. The maximum size of the annular scoring plane for the 40x40 mm^2 field size applicator is 3.0 cm in radius while that for the 1 mm applicator is 0.5 mm in radius. The scoring zone was positioned at an SSD of 23.5 cm along the z-axis for all applicators, as shown in Figure 3.3. The EGSnrc Monte Carlo transport parameters, Table 3.2, are chosen based on the information provided in the literature for the orthovoltage energy range (Mainegra-Hing and Kawrakow, 2006).

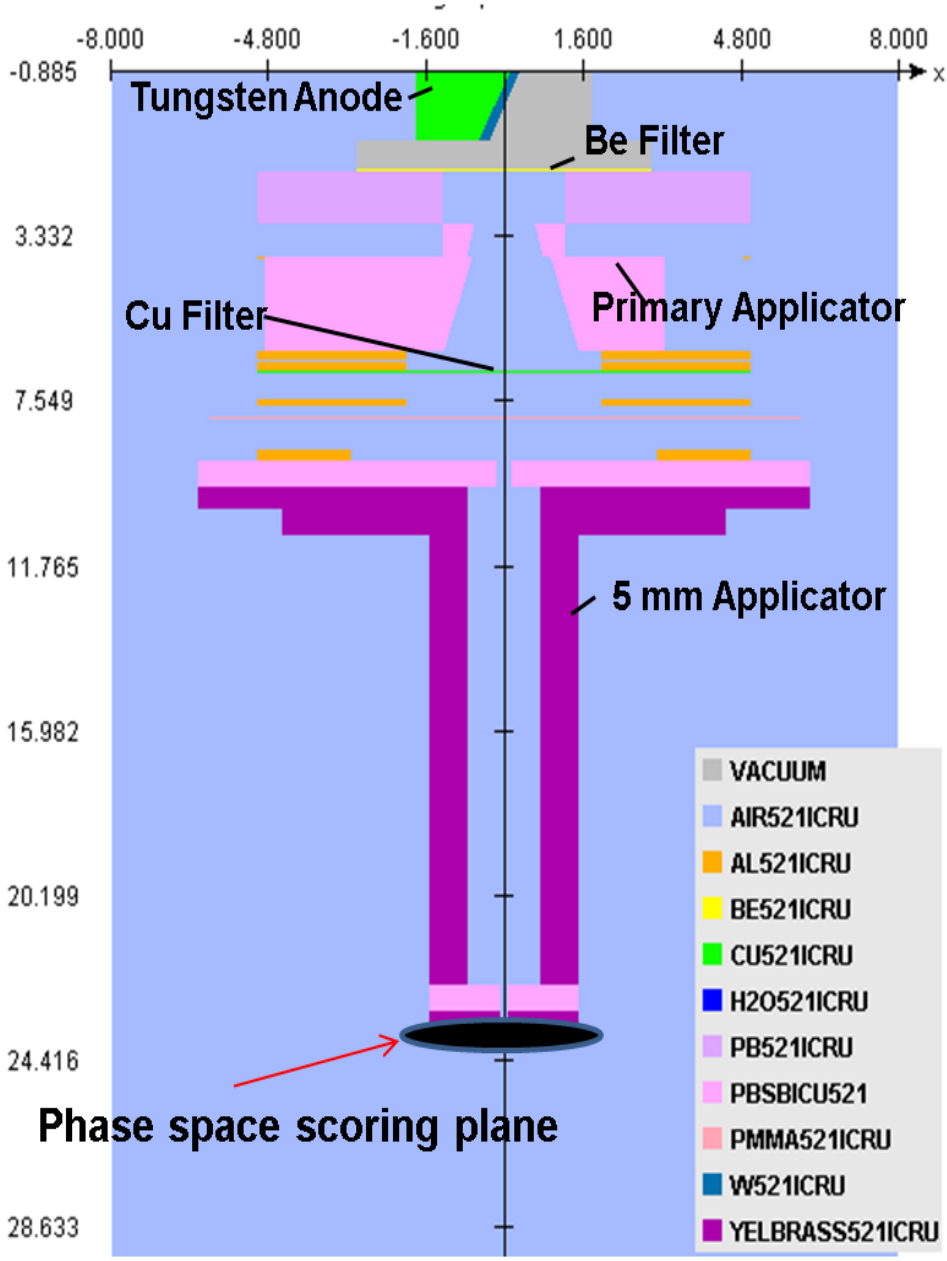

Figure 3.3: Geometry model for MC simulation in BEAMnrc for circular field applicator.

Transport parameters (EGSnrc input)	BEAMnrc ver.2.0 (source)	DOSXYZnrc v.1.1 (Phantom)
Photon cross sections		SI
Compton cross sections		default
Photon transport cutoff (MeV)		0.1000E-01
Photoelectron angular sampling		ON
Electron transport cutoff (MeV)		0.0100
Boundary crossing algorithm		EXACT
Electron-step algorithm		PRESTA-II
Electron Impact Ionization		On
Spin effects		On
Bremsstrahlung angular sampling		KM
Bremsstrahlung cross sections		NIST
Bound Compton scattering		ON
Rayleigh scattering		ON
Atomic relaxations		ON
Global electron cutoff energy- ECUT(MEV)		0.521
Global Photon cutoff energy- PCUT(MEV)		0.01
Variance reduction		DBS
Electron range rejection		off
Directional bremsstrahlung splitting (DBS) number	3.5x105	-
DBS splitting radius and z location from source	5 cm, 30.5 cm	-
BCSE	off	-

Table 3.2: MC Transport parameters used for simulations in the BEAMnrc and DOSXYZnrc.

3.5 Benchmarking

Calculation accuracy in treatment planning depends on numerous parameters and approximations in the development of beam model, chain of algorithm development and its implementation. Measurements are prone to minimal deviations resulting from reproducibility, detector suitability and also misinterpretations of results. In this work, ionization chamber and film were used to measure dosimetric characteristics. The variance of the dose determined for the ionization chamber measurements was estimated to be 1.5% at one standard deviation (Huq et al., 2001). Variance in film response to radiation depends on numerous factors such as differences in film composition and the orientation and position of the film during scanning. For this reason, variance in Gafchromic EBT2 film dosimetry was addressed by performing numerous exposures (n=20) from a single lot (Lot #A12091101) with identical film positioning, orientation and all given an identical dose (343 cGy mean dose). The variation in film response was determined to be 2.2% at one standard deviation.

The validation of the XRAD 225Cx Monte Carlo photon source model was performed by comparing the MC calculated values to measured data. These data consist of characterizing HVL, percent depth dose and dose profiles for several field sizes. Mean profiles were compared at 2 cm depth in a solid water phantom for circular field sizes of 1, 10, and 20 mm. After validation, the source model was benchmarked under multiple conditions in homogenous and heterogeneous phantoms.

Treatment planning in radiotherapy involves numerous uncertainties from positioning, imaging, defining the anatomy, establishment of beam geometry and dose calculation, all of which can affect the accuracy of treatment. Thus it is critical to benchmark the beam model in clinically relevant situations, including in both homogenous and heterogeneous media. A systematic verification process was undertaken to compare measurements to calculated dose distributions for benchmarking beam model. The standard method of comparison incorporated 1-D line comparisons (depth doses and dose profiles), 2-D isodose lines (overlaying isodose lines on axial, coronal and sagittal planes) and distance maps (measurement of the distance of equal dose points between measured and calculated dose distributions). The TG-53 protocol, provides acceptability criteria for external beam dose calculations for specific situations (homogenous and heterogeneous phantoms) (Fraass et al., 1998a), and is used to guide acceptance under a variety of conditions. Specific acceptance criteria between calculation and measurements are divided depending on the position of the radiation beam in the phantom. Figure 3.4A shows the four regions of a photon beam, each with different acceptance criteria. In the inner beam region, agreement within 1.5% and 5% in homogenous and heterogeneous media, respectively, is recommended. In the outer beam region, agreement should within 2% for homogenous and 5% for heterogeneous media. High dose gradients exist between the inner and outer beam regions, i.e penumbra (distance between the 20 and 80% dose level). Agreement in the penumbra region should be within 2 mm in a homogenous medium and 7 mm in a heterogeneous medium. The virtual homogenous 3D water phantom constructed for MC simulation for dose calculations using phase space files created for each field size as shown in Figure 3.4B.

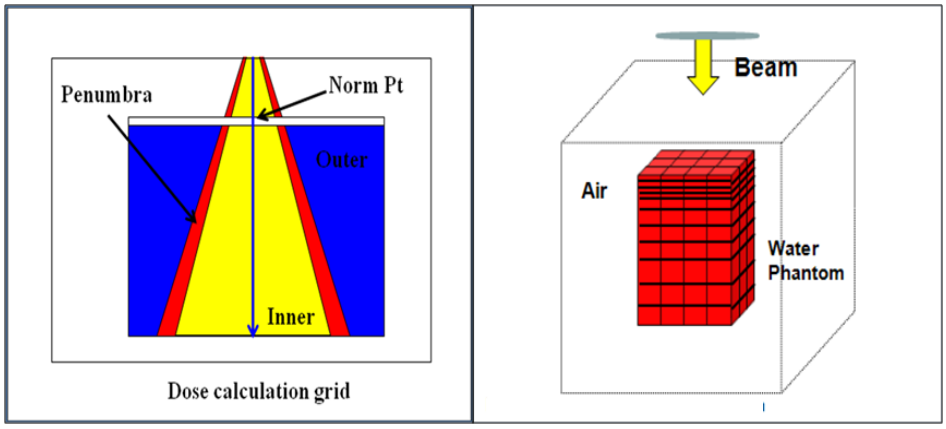

A B

Figure 3.4 A) Regions for photon dose calculation grid agreement analysis following the TG-53 protocol. B) Water phantom (10x10x12 cm^3) for DOSXYZnrc MC simulation.

3.5.1 Half Value Layer (HVL)

The HVL is derived from the photon spectra by finding the thickness of Cu attenuator that reduces the original fluence to 50% (Verhaegen et al., 1999). The half-value layer (HVL) can be found by iterating the absorber thickness (t) until the fluence of the spectrum is reduced to half. The thickness of attenuator defines the beam quality for specific beam model. To determine the half-value layer and mean energy of the beam model, a scoring plane with a 1 cm diameter scoring zone was placed (in air) at an SSD of 50 cm. Using the resulting phase space file, a spectrum was constructed with an energy bin width of 1.3 keV using the BEAMDP code (Ma and Rogers, 2009). Simulations were run until a statistical variance of 1% or less for each energy bin was achieved.

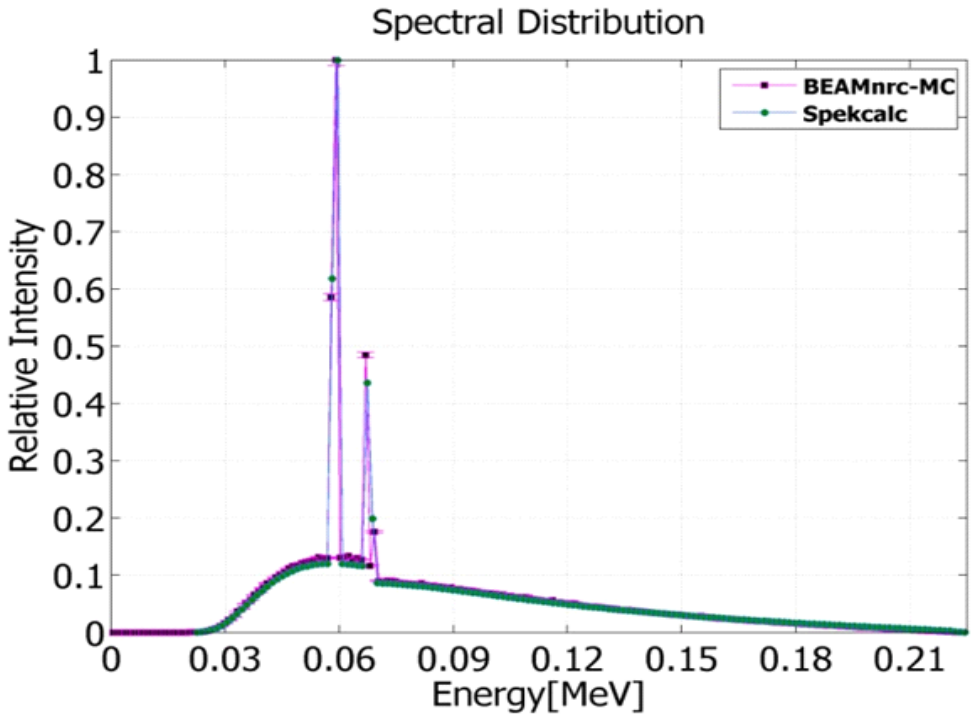

Figure 3.5: Spectral distribution comparison between Monte Carlo and Spekcalc.

HVL was calculated for the XRAD 225Cx with spectra derived from Monte Carlo simulation. The Monte Carlo simulation results then were compared to the numerical value from "Spekcalc" for this specific x-ray configuration. Spekcalc is a program developed for the calculation of x-ray spectra from a tungsten anode in any x-ray tube (Poludniowski et al., 2009, Poludniowski, 2007). This program relies on the deterministic equations for Bremsstrahlung and characteristic photon productions to determine the x-ray spectra. This program works for a wide range of potentials (4-300 kVp) and anode angles ($6\text{-}30^0$). The mean energy of the spectrum determined by Spekcalc is 85.4 keV, within 1% of the value of 84.7 keV derived from the BEAMnrc simulation. The spectral comparison between the Spekcalc and BEAMnrc in Figure 3.5 shows an average agreement of 1% with the largest outlier at 10%. The HVL measurement was performed in-air utilizing a 15 mm square collimator with a PTW N31014 pinpoint ionization chamber placed 50 cm from the collimator opening. The resulting HVL, at a tube potential of 225 kVp and tube current of 13 mAs, was measured to be 0.985 mm Cu (Chapter 2, Figure 2.6). Subsequent MC simulation using the spectrum derived above resulted in an HVL of 0.95 mm Cu, a difference of 3.5% between measurement and simulation (chapter 2). The likely source of this disagreement is the precision error of thickness of the attenuators used.

3.5.2 Percent Depth Dose (PDD)

An independent phsp file was simulated in BEAMnrc for each field size given in Table 3.1. The phsp space file was positioned at 23.5 cm SSD for all field sizes. Dose calculations using a voxelized water phantom were performed using the MC module DOSXYZnrc (ver1.1). Each file was used to compute dose in a 10x10x12 cm^3 water phantom at an SSD of 7 cm from the virtual source (phsp space scoring plane) as shown in Figure 3.4B, using transport parameters provided in Table 3.2. Because the field sizes span from 1 mm diameter to 40x40 mm^2, various phantom resolutions were chosen. The dimensions of the scoring voxels for each field size in the DOSXYZnrc simulations are given in Table 3.3.

A file containing the 3D dose was generated after MC simulation for each field size from which percent depth dose (PDD) was determined. Each 3D dose file was imported into MATLAB and analyzed to extract the four central voxels volumes 0.04 mm^3 (0.1 mm x 0.1 mm x 1 mm) to 4 mm^3 (2 mm x 2 mm x 1 mm) for smallest to largest field size. The dose within each of the four central voxels was then averaged.

Depth dose characteristics were measured using a pinpoint ionization chamber in water, and using Gafchromic EBT2 film in a solid water phantom. For all square and "larger" circular field sizes, i.e., greater than or equal to 10 mm diameter, a pinpoint ionization chamber was utilized using the same setup as described for absolute dose calibration, with an exposure time of 30 seconds at each depth. To avoid partial volume effects in the ionization chamber, PDD measurements for field sizes less than 10 mm in diameter were measured using only film. For circular field sizes less than 10 mm in diameter, Gafchromic EBT2 films placed between thin solid water slabs and exposed for

60 seconds. Starting from top to bottom, the solid water phantom consisted of eight 1 mm slabs, six 2 mm slabs, eight 3 mm slab, and eight 5 mm slabs. This setup resulted in a total of 31 films. The measurement depths were corrected for the average film thickness of 0.270 mm. In addition, PDDs for larger fields were also measured with film to study any deviations from measurements in solid water to water.

The maximum dose (D_{max}) for orthovoltage energies is at the surface, so percent depth dose for each field size was normalized to the surface voxel. Comparison of PDD curves performed by fitting each curve with a 9^{th} degree polynomial (regression co-efficient value greater than 0.9999 for each fit) to enable point-by-point comparison (percent difference) at equal depths. The statistical uncertainty in Monte Carlo simulation was 1 to 2.5 % (the uncertainty increases with depth).

The recommendations of the AAPM TG-53 protocol were used for comparing MC simulation data with the corresponding measurements (Fraass et al., 1998a). For instance, the acceptability criteria for a homogeneous medium for depth dose at the central-axis should be within 1% of the measurement.

The MC PDDs and ionization chamber measured PDDs for circular and square field sizes are shown in Figure 3.6 and Figure 3.7 respectively. In this work 20 mm, 10 mm, 5 mm and 1 mm diameter circular field sizes were choose to bench mark the percent depth dose measurements against Monte Carlo calculations. The mean difference was 1% between the MC calculations and ionization chamber measurements for the 20 mm field size shown in Figure 3.6. Similarly, for the 20 mm field size, PDD measurements with film were compared to MC calculations shown in Figure 3.8 exhibit a mean difference of 1.83% and maximum deviation of 3.5% towards the tail of the curve. For the 10 mm field

size, a mean difference of 0.15% between MC and measurement was observed. A maximum deviation of 2% occurred near the surface (Figure 3.9). Figure 3.10 shows results for the 5 mm collimator, with a mean difference of 2.3% between the MC and film measurements. A comparison between MC calculations and film measurement for the 1 mm collimator is shown in Figure 3.11; the average difference between calculation and measurement is 3.2% with a maximum deviation of 5.5 %.

Field size at isocenter	Total number of voxels for 3D phantom	X-axis	Y-axis	Z–axis
1.0 mm	42x42x80 (10x10x12 cm^3)	01 x 4.50 cm 40 x 0.01 cm 01 x 4.50 cm	01 x 4.50 cm 40 x 0. 01 cm 01 x 4.50 cm	40 x 0.1 cm 40 x 0.2 cm
2.5 mm 3.5 mm 5.0 mm	42x42x80 (10x10x12 cm^3)	1 x 4.500 cm 40x 0.025 cm 1x 4.500 cm	01 x 4.500 cm 40 x 0.025 cm 01 x 4.500 cm	40 x 0.1 cm 40 x 0.2 cm
10.0 15.0 mm 20 .0 mm 10x10 mm^2 15x15 mm^2 20x20 mm^2 40x40 mm^2	42x42x80 (10x10x12 cm^3)	1x 1.0 cm 40x 0.2cm 1x 1.0 cm	01 x 1.0 cm 40 x 0.2 cm 01 x 1.0 cm	40 x 0.1 cm 40 x 0.2 cm

Table 3.3: DOSXYZnrc virtual phantom size and pixel sizes are provided along x, y and z axis.

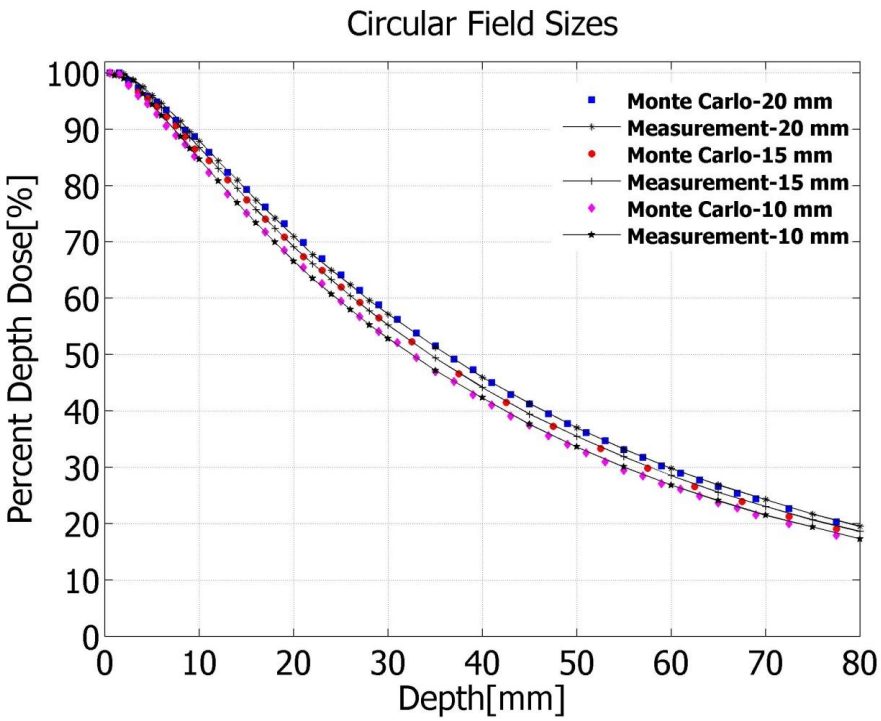

Figure 3.6: Monte Carlo calculated and ionization chamber measured percent depth dose curves at 225 kVp for 20 mm, 15 mm, and 10 mm diameter circular field sizes.

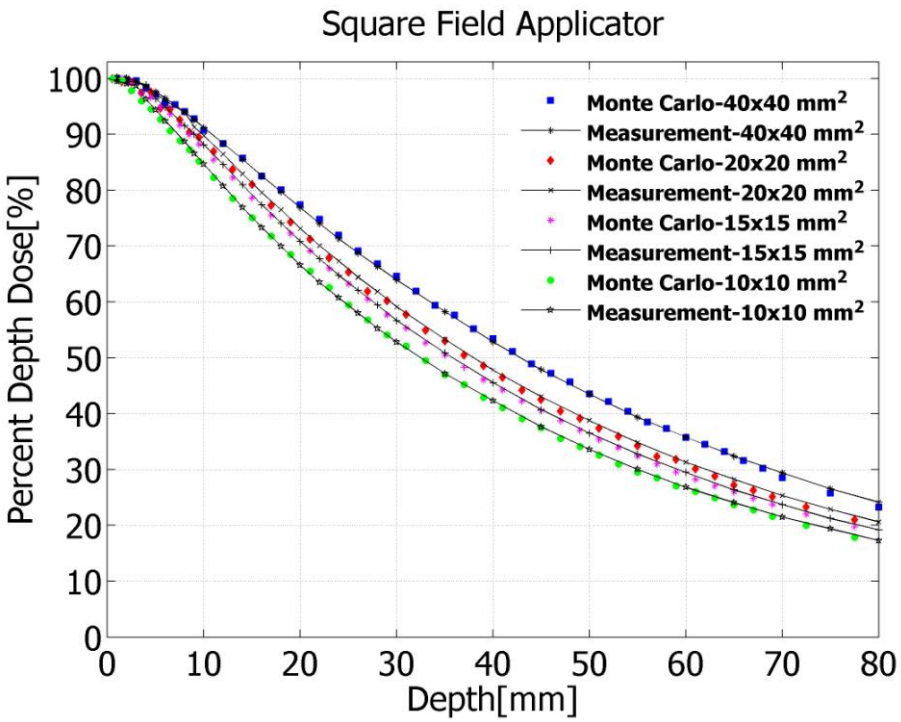

Figure 3.7: Monte Carlo calculated and ionization chamber measured percent depth dose curves at 225 kVp for square field sizes.

.

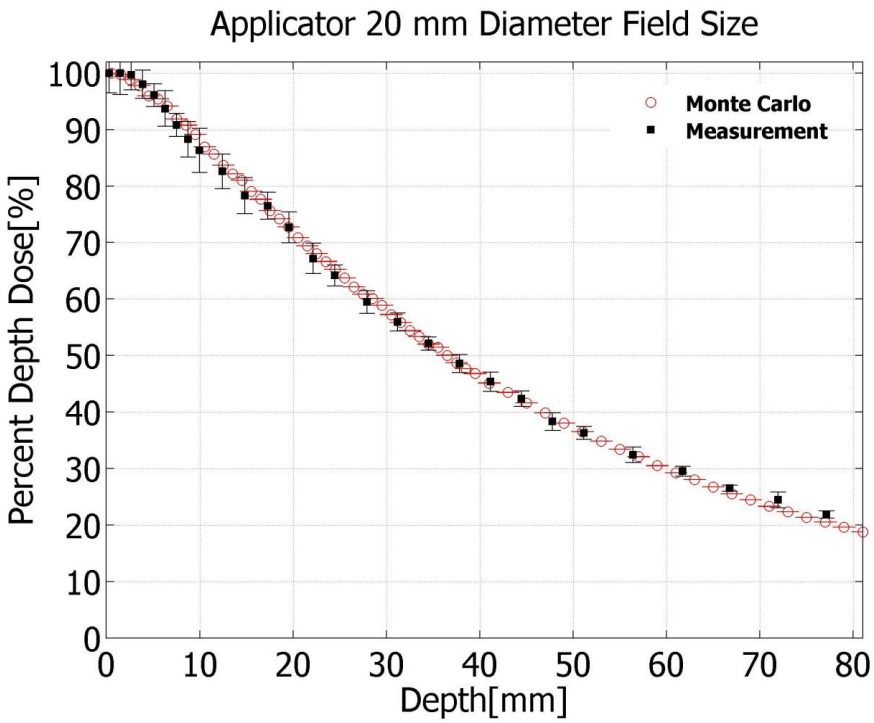

Figure 3.8: Monte Carlo (MC) calculated and EBT2 film measured percent depth dose curves at 225 kVp for a 20 mm diameter circular field.

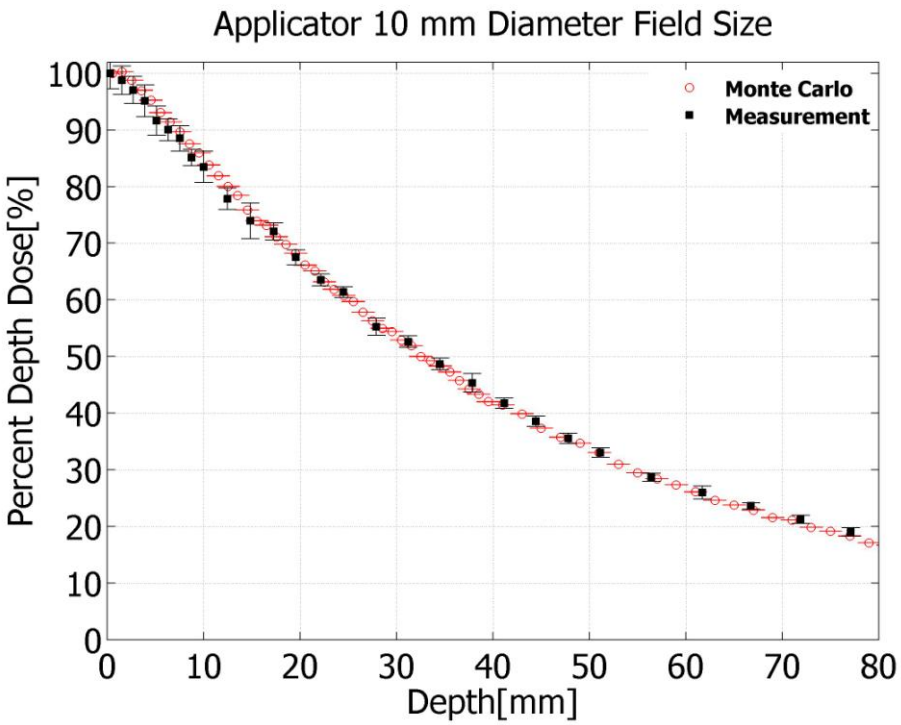

Figure 3.9: Monte Carlo calculated and EBT2 film measured percent depth dose curves at 225 kVp for a 10 mm circular field.

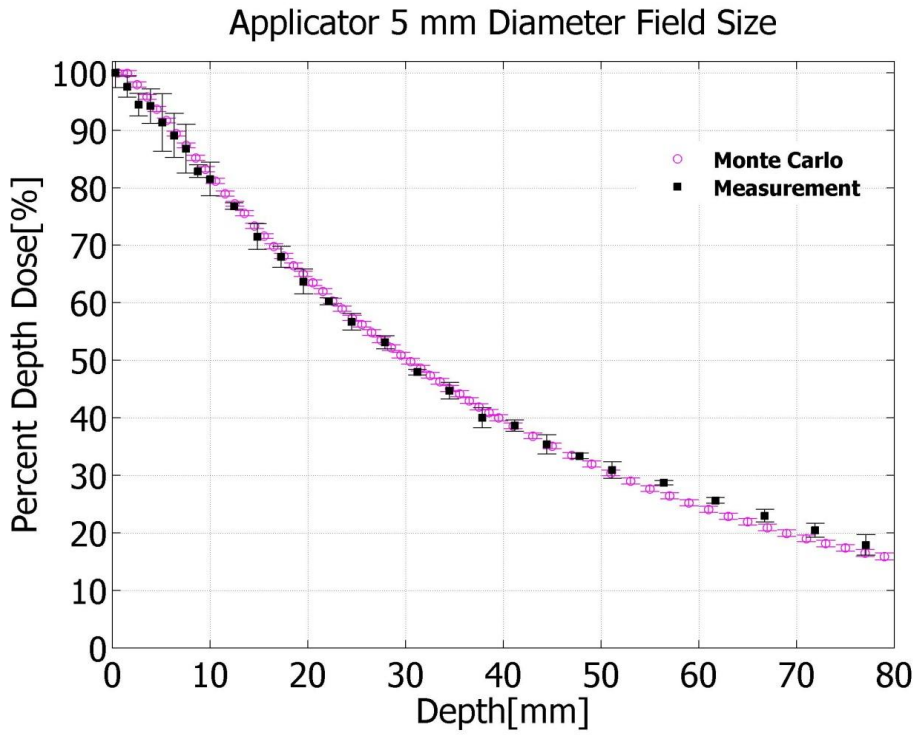

Figure 3.10: Monte Carlo calculated and EBT2 film measured percent depth dose curves at 225 kVp for a 5 mm circular field.

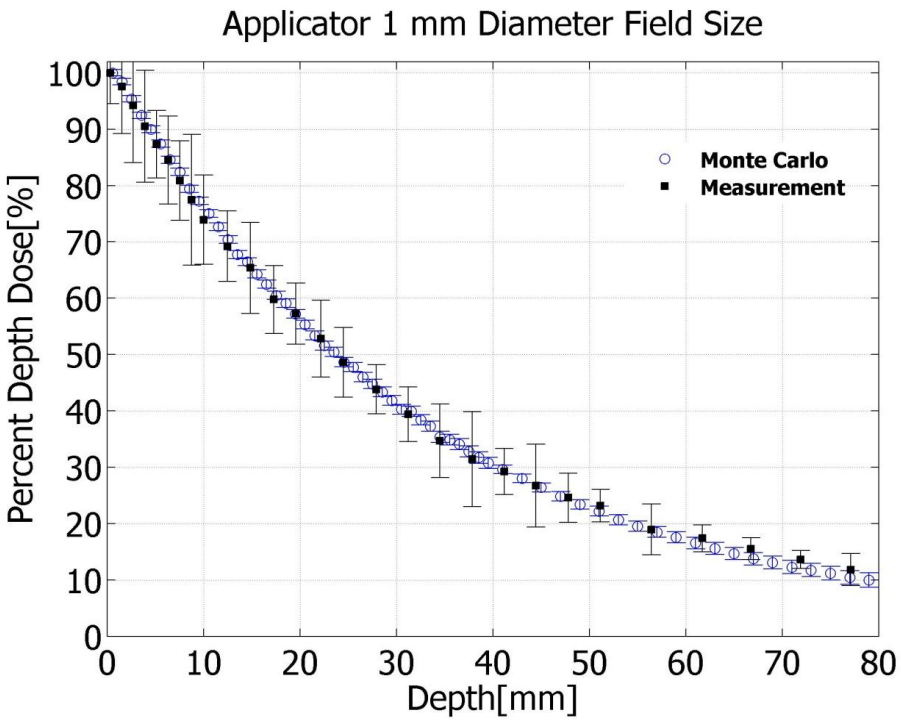

Figure 3.11: Monte Carlo calculated and EBT2 film measured percent depth dose curves at 225 kVp for a 1 mm diameter circular field size

3.5.3 Dose profiles

Gafchromic EBT2 film was used to measure dose profiles, the dose variation across the field at a specified depth. Profiles were obtained using film placed perpendicular to the radiation beam at a depth of 2 cm in a solid water medium. Each film (4x4 cm^2) was exposed for 2 minutes at 250 kVp, 13 mAs irradiator settings. Films were scanned at a resolution of 150 dpi 24 hours following irradiation and saved in "TIF" image format. Resulting images were imported into MATLAB, where optical density was converted to dose using the kV calibration curve (225 kVp) obtained in Chapter 2. The resulting 2D distributions were normalized to the central axis dose. Dose profiles were obtained by averaging the two central rows of each image.

MC calculations were performed in a simulated water phantom using DOSXYZnrc for various field sizes (20 mm, 10 mm, 1 mm) and were imported into MATLAB. The planar dose (2D dose matrix) at 2 cm depth was extracted from each 3D dose matrix (simulation). Each 2D dose matrix was normalized to the central axis of the beam. Dose profiles were computed for 20 mm, 10 mm and 1 mm circular collimators.

Both measurement and simulation results are plotted in Figures 3.12-3.14. Deviations between measurement and calculation results are divided into three regions 1) the low dose region (outer beam), the high dose region (inner beam) and the penumbra region. For the 10 and 20 mm field sizes, a mean difference of 1% was observed between measurement and MC in the inner beam region. For the 1 mm field size the mean difference was 5%. This relatively large disagreement is primarily due to the low resolution of the Monte Carlo simulation and applicator design for smaller field sizes less

than 5mm. These applicators having two apertures at the top and bottom, the top aperture doesn't aligned with the bottom aperture.

For the 20 mm field size, a mean difference of 2.1% was observed in the outer beam region. Similarly for the 1 and 10 mm field sizes, the mean difference was less than 1%. The penumbra and FWHM for Monte Carlo simulations and film measurements for the 1, 10 and 20 mm field sizes are given in Table 4.4.

Field Size	20 mm	10 mm	1 mm
Measured Penumbra (mm)	1.45	1.20	0.30
Monte Carlo Penumbra (mm)	1.67	1.23	0.21
Measured FWHM (mm)	20.05	10.05	1.07
Monte Carlo FWHM (mm)	20.02	10.05	1.01

Table 3.4**:** Monte Carlo calculated and measured penumbra and Full width half maximum at 2 cm depth for a 20, 10 and 1 mm diameter circular field sizes.

3.5.4 Gamma Analysis

To assist in the quantitative comparison of dose distributions, Low et al. have developed a quantitative evaluation tool that combines dose and distance criteria in a single metric. Doses and spatial coordinates are normalized by user-selected dose and distance acceptance criteria, resulting in a unitless quantity. The Gamma method uses the following equation (3.2) to compare the measurements versus the calculated result

$$\gamma(r_m, r_c) = \sqrt{\frac{r^2(r_m, r_c)}{\Delta d_M^2} + \frac{\delta^2(r_m, r_c)}{\Delta D_M^2}} \tag{3.2}$$

When $\gamma(r_m) \leq 1,$ calculation agree with measurements

$\gamma(r_m) > 1,$ calculation and measurement do not agree.

Where $\delta(r_m,r_c) = D_c(r_c)-D_m(r_m)$

$r(r_m,r_c)_{,=} |r_c - r_m|$

ΔD_M is the dose difference between the measured and calculated dose distribution.

Δd_M is the distance between a measured data point and the nearest point in calculated dose distribution.

δ is the difference between the measured dose point $[D_m(r_m)]$ and calculated dose point $[D_m(r_m)]$

r_c is the spatial location of the calculated dose distribution point relative to the measured point r_m

$\gamma(r_m)$ is the gamma index value.

Gamma analysis between MC and film measurements was performed for the 20 and 10 mm dose profiles. Typical gamma acceptance criteria are 3% dose difference and 3% distance to agreement (Fraass et al., 1998a). As general rule in gamma analysis the pixel spacing should be less than or equal to 1/3 of the distance to agreement (Low and Dempsey, 2003, Low et al., 1998). Based on the small fields used in this work, therefore, we have chosen 3% dose difference and 0.5 mm distance to agreement gamma acceptance criteria for analysis. For the 20 mm and 10 mm field sizes, both the inner and outer beam meet the gamma index value <1, while in the penumbra region there are some pixels with gamma index >1. The overall gamma passing rate is 95 % and 98% for the 20 and 10 mm field sizes respectively.

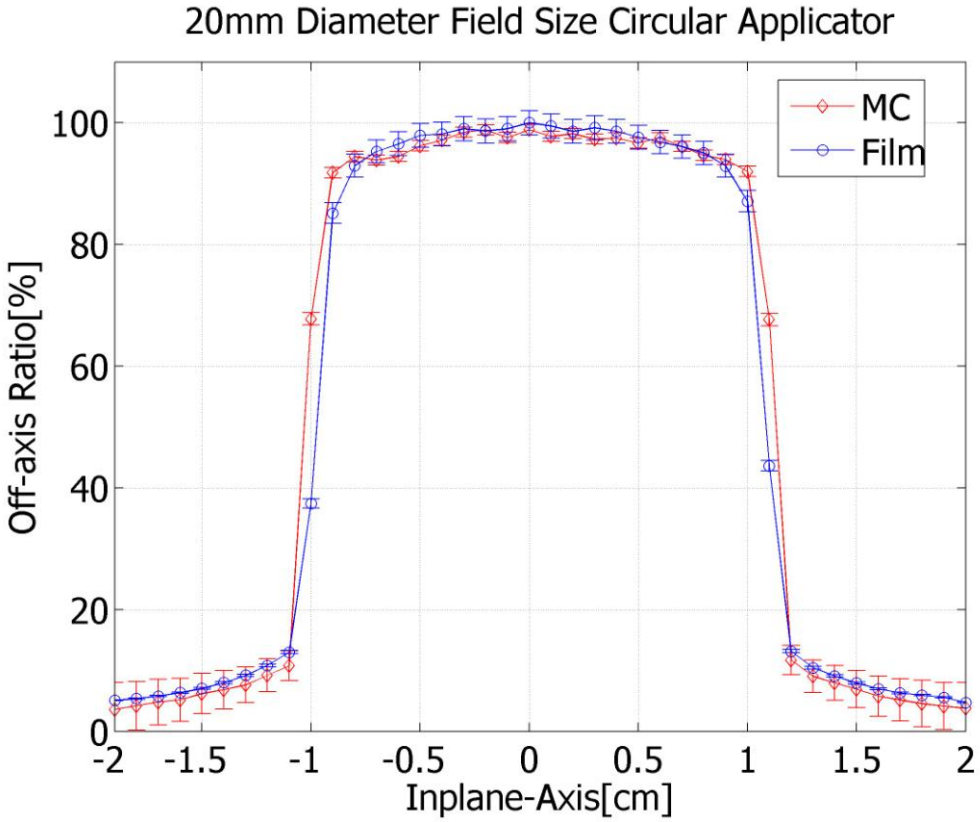

Figure 3.12: Dose profile measurements using EBT2 film (blue line) and MC simulation result (red line) of 20 mm diameter circular field size. Each profile is normalized to the central axis point.

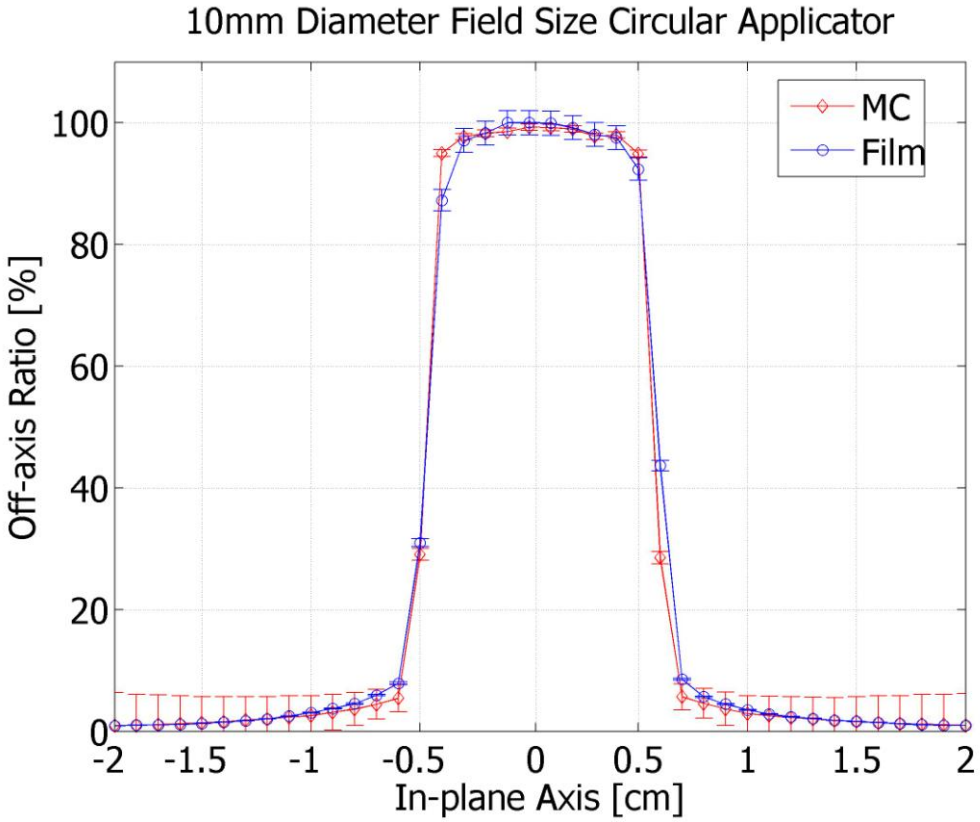

Figure 3.13: Dose profile measurements using EBT2 film (blue line) and MC simulation result (red line) of 10 mm diameter circular field size applicator.

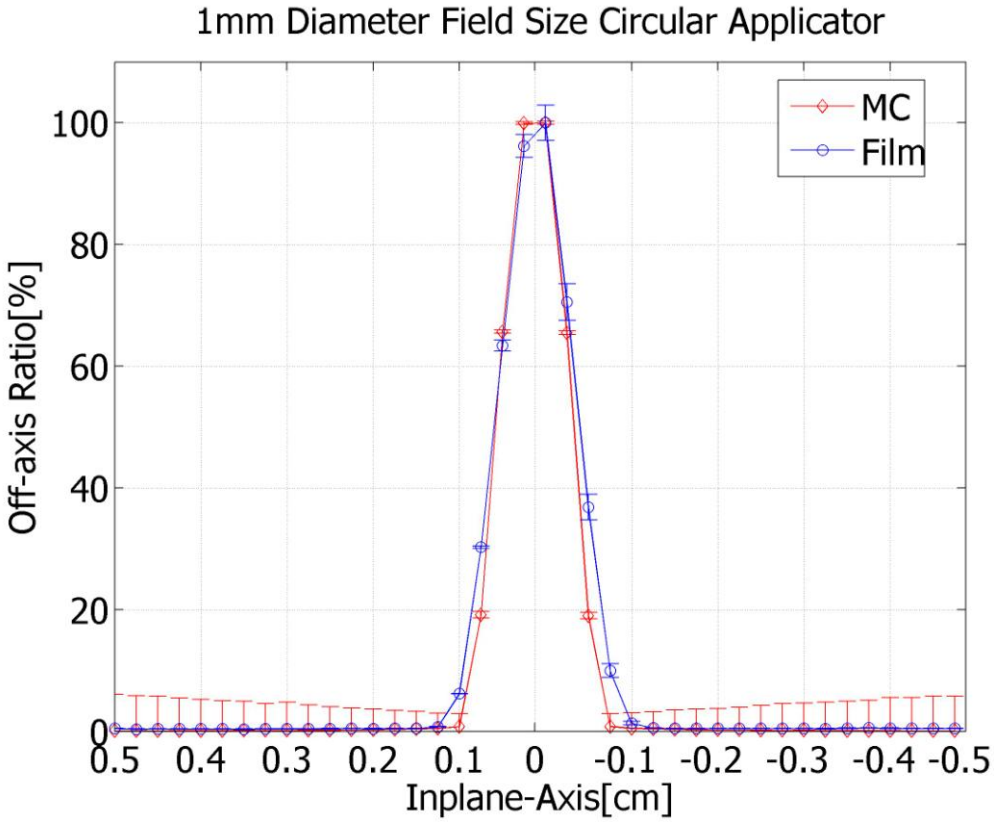

Figure 3.14: Dose profile measurements using EBT2 film (blue line) and MC simulation result (red line) of 1 mm diameter circular field size applicator.

3.6 Validation of the Monte Carlo source model in homogeneous Medium

3.6.1 Gamma Analysis in homogeneous medium

Quantitative evaluation of measured and MC computed planar isodose a distribution was performed using Film QA, and analyzed using a commercial film dosimetry software package. Calculated results of planar dose for a 10x10 mm^2 square field and a 20 mm diameter circular field were compared against the measurements obtained at a depth of 2 cm. The three dimensional dose file from DOSXYZnrc was imported into MATLAB and a 2D matrix containing the planar dose at 2 cm depth was extracted for import into FilmQA. Measured planar dose distributions were obtained by exposing EBT2 films at depth of 2 cm in a solid water medium (10x10x12 cm^3). These films were scanned using an EPSON 1000XL scanner and saved in TIF format. The scanned images were imported into Film QA software for gamma analysis.

The 90%, 80%, 50% and 20% isodose lines for measurement and simulation are shown superimposed in Figure 3.15. Profiles were normalized to the maximum dose value according to the TG-53 protocol (Fraass et al., 1998b). Dose profiles along two perpendicular axes are shown in Figures 3.16 and 3.17. Agreement between the calculation and the measurement is within 1% the outer and inner beam regions. The gamma analysis is shown in Figures 3.18–3.19, with minor disagreement (gamma index>1) in the penumbra region. Overall, 95.3% of the pixels meet the gamma criteria of 3%/0.5 mm. A similar analysis for a 20 mm circular field is shown in Figures 3.20 - 3.22. Agreement in the inner and outer beam regions of dose profiles within 1% and 3%, respectively. The large disagreement of 3% in the low dose regions for large fields is due to over response of the film from low energy scattered photons (detailed discussion

provided in section 3.10). The gamma index map within the region of interest, shown in Figure 3.23, indicates that 97.6 % of measured and calculated points meet the 3%/0.5 mm gamma criteria.

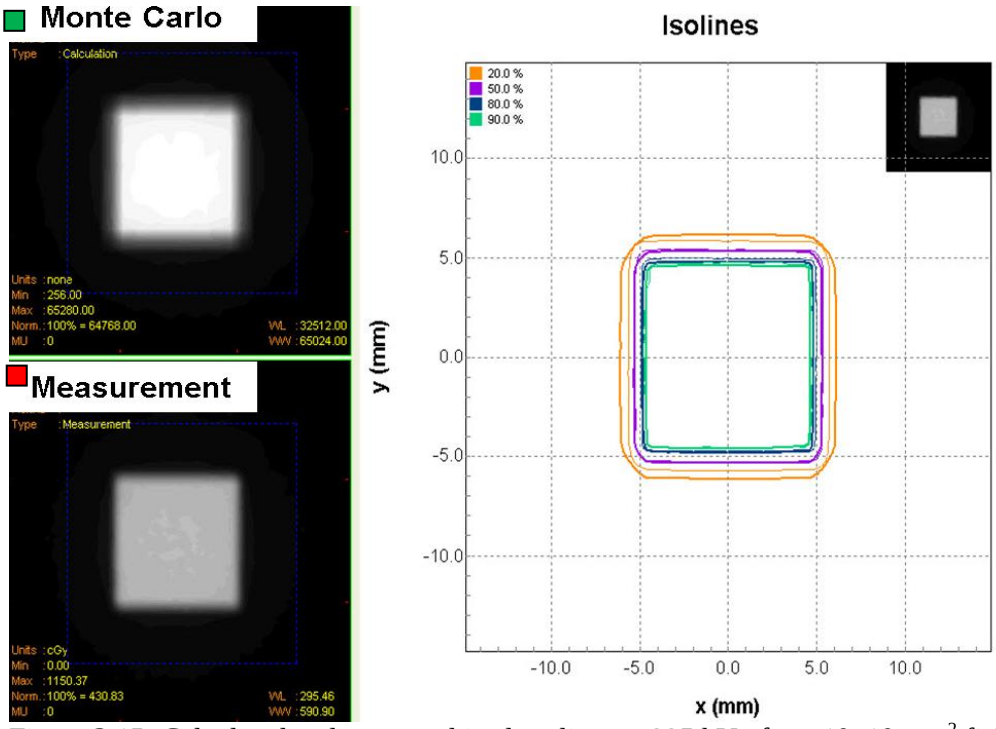

Figure 3.15**:** Calculated and measured isodose lines at 225 kVp for a 10x10 mm^2 field size at 2 cm depth. Thin isodose lines correspond to measurement and thick lines to Monte Carlo.

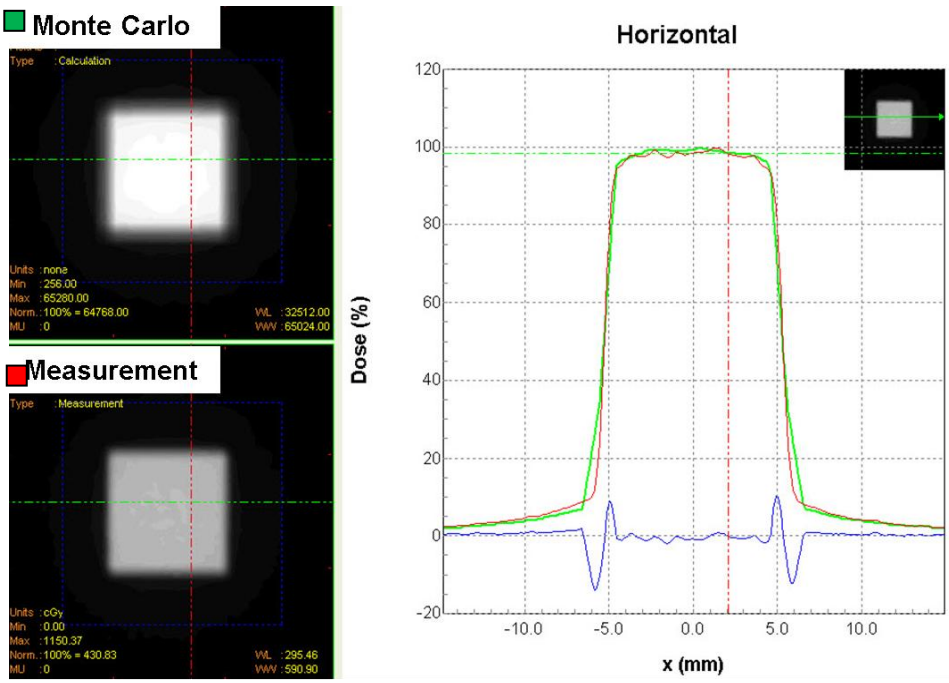

Figure 3.16**:** Calculated and measured horizontal dose profile at 225 kVp for a 10x10 mm^2 field size at 2 cm depth.

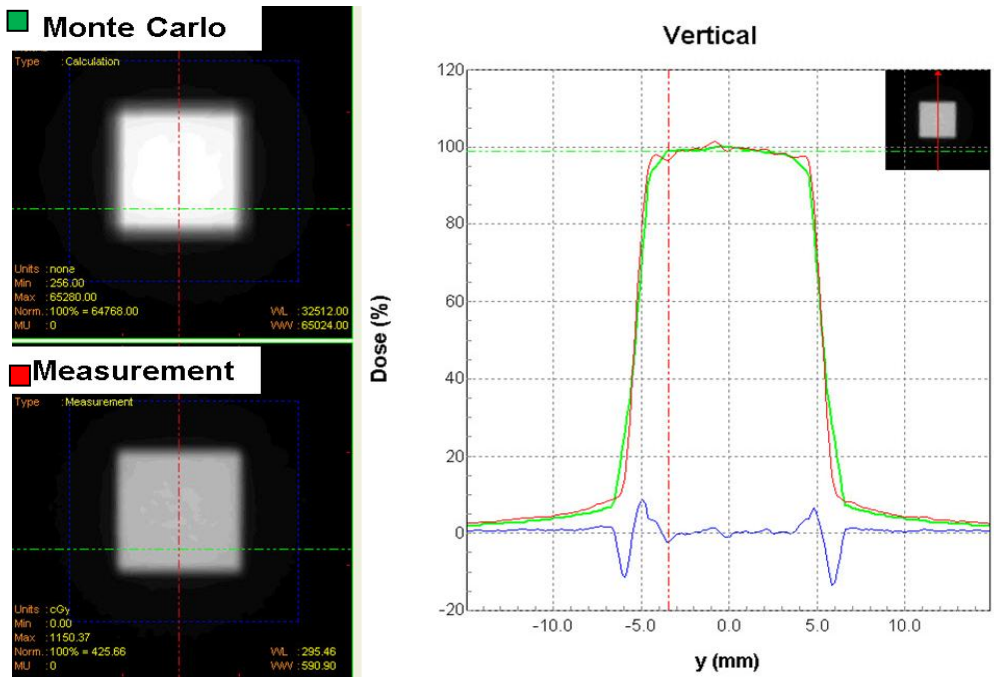

Figure 3.17: Calculated and measured vertical dose profile at 225 kVp for a 10x10 mm^2 field size at 2 cm depth.

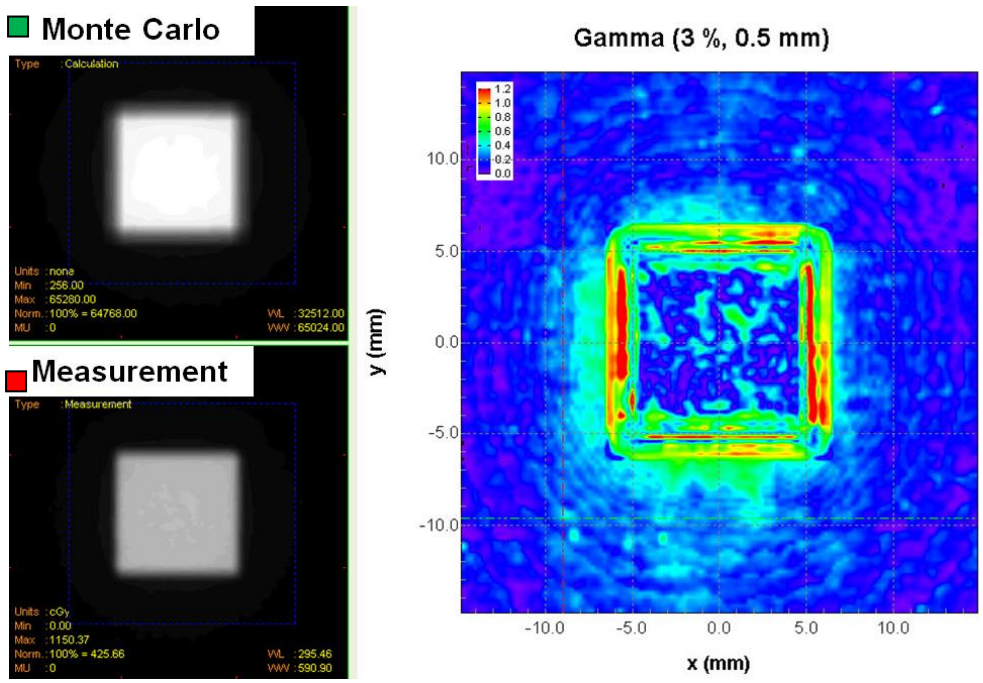

Figure 3.18: A comparison between simulated and measured 2D results for a 10x10 mm^2square field applicator. The 3% and 0.5 mm gamma criterion was used.

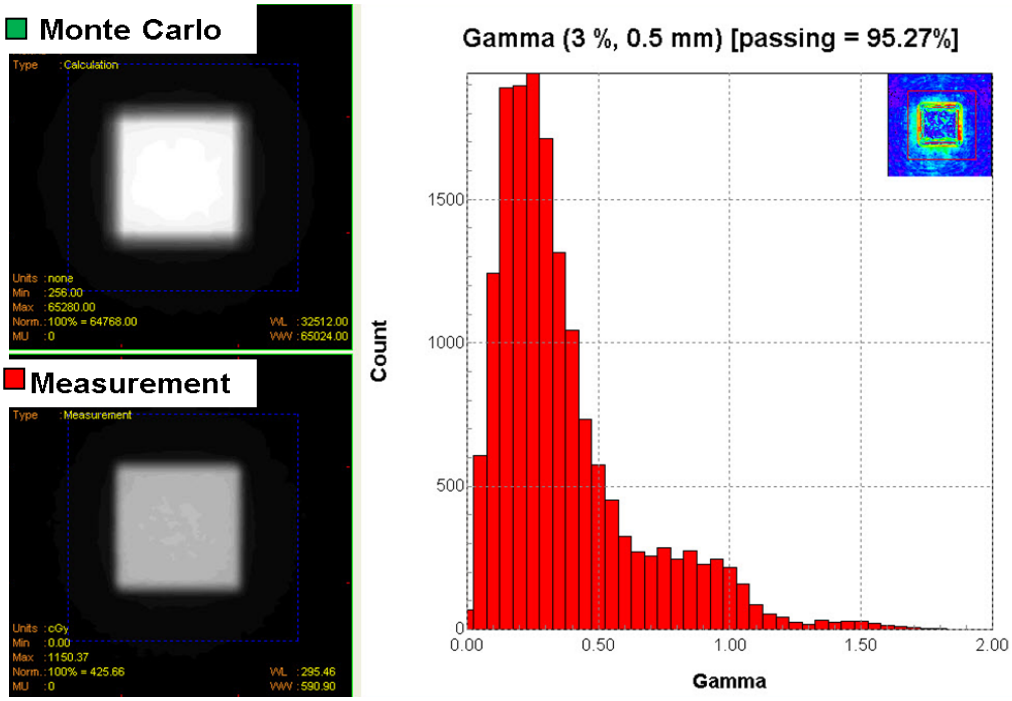

Figure 3.19: Anterior to posterior single beam irradiation. Gamma map for 3%/0.5 mm criteria, indicating 95.27% passing rate.

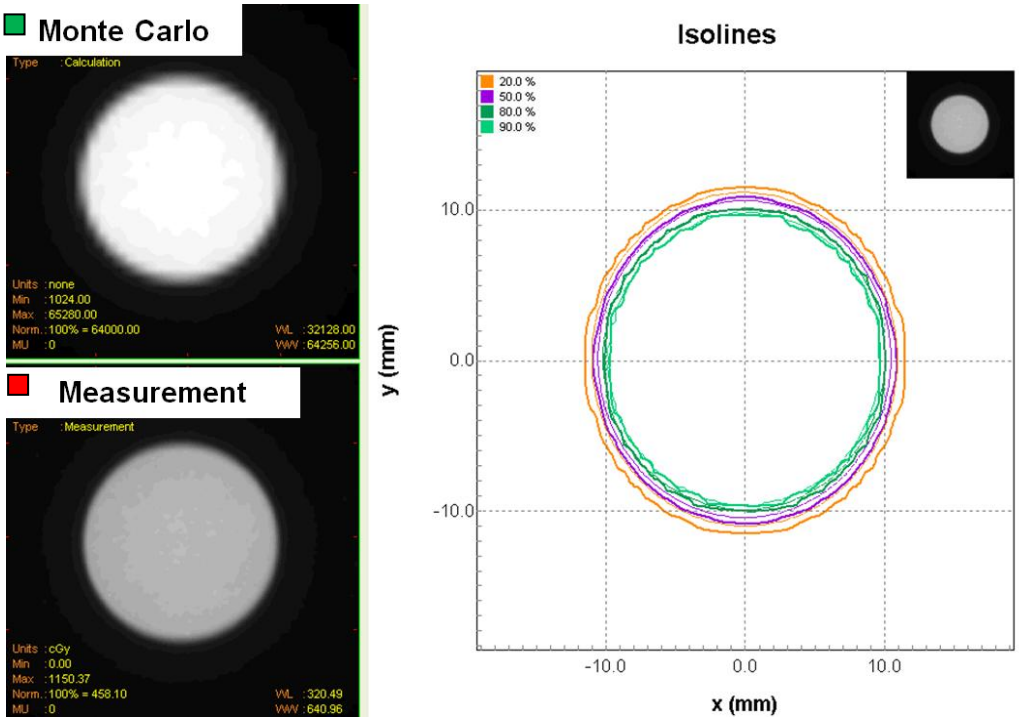

Figure 3.20: Calculated and measured isodose lines at 225 kVp for a 20 mm diameter circular field size at 2 cm depth. Thin isodose lines correspond to measurement and thick lines to Monte Carlo.

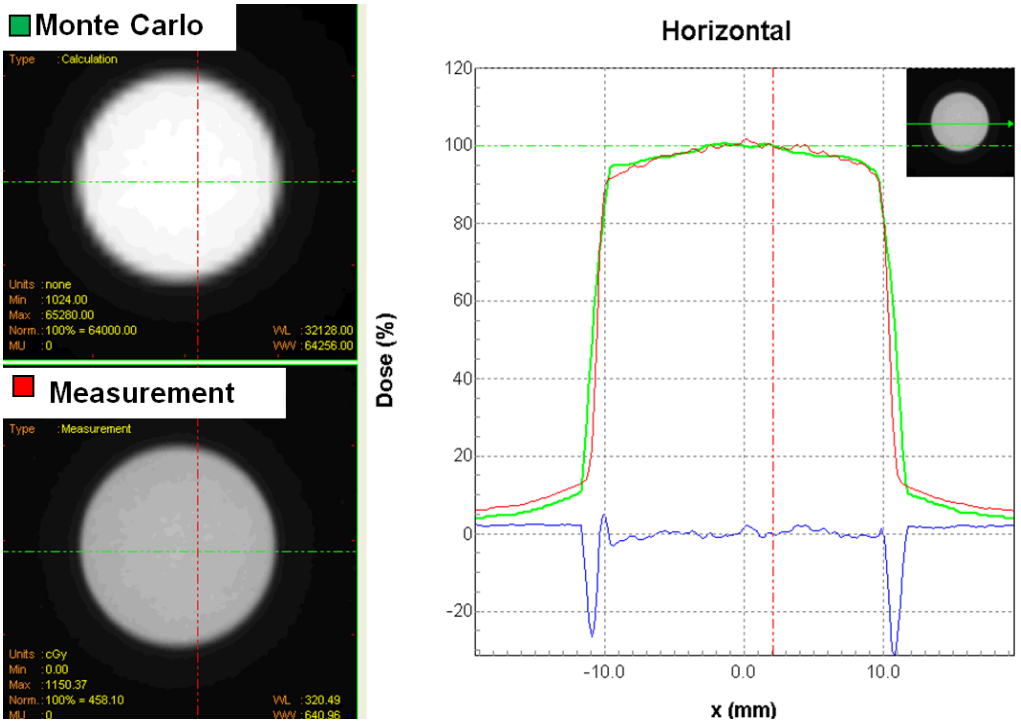

Figure 3.21: Calculated and measured horizontal dose profile at 225 kVp for a 20 mm diameter circular field size at 2 cm depth.

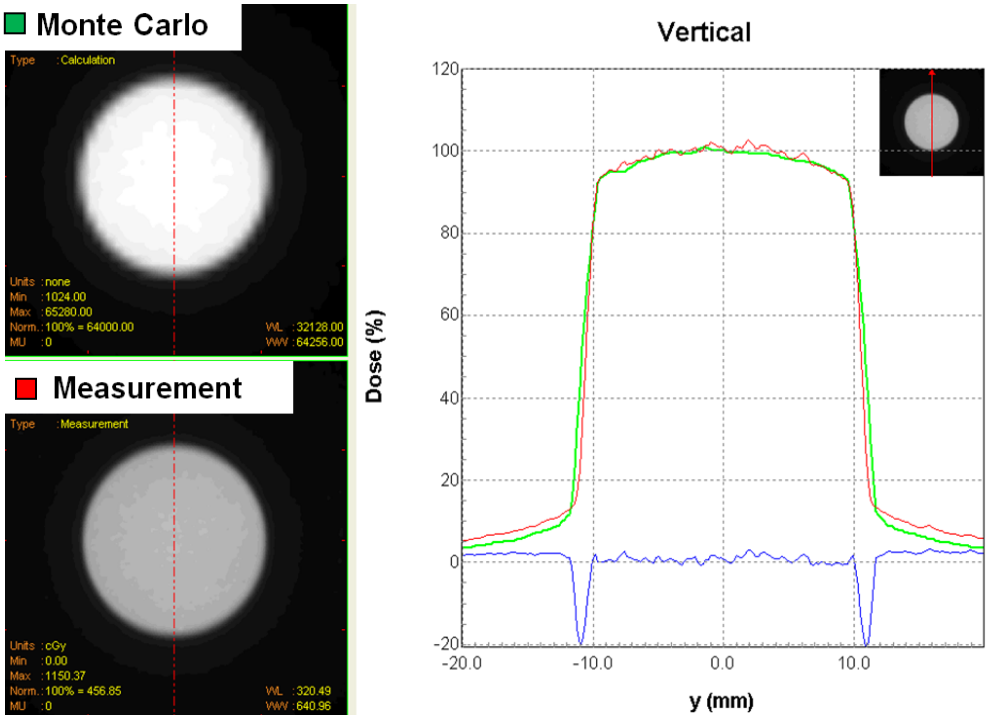

Figure 3.22: Calculated and measured vertical dose profile at 225 kVp for a 20 mm circular diameter field size at 2 cm depth.

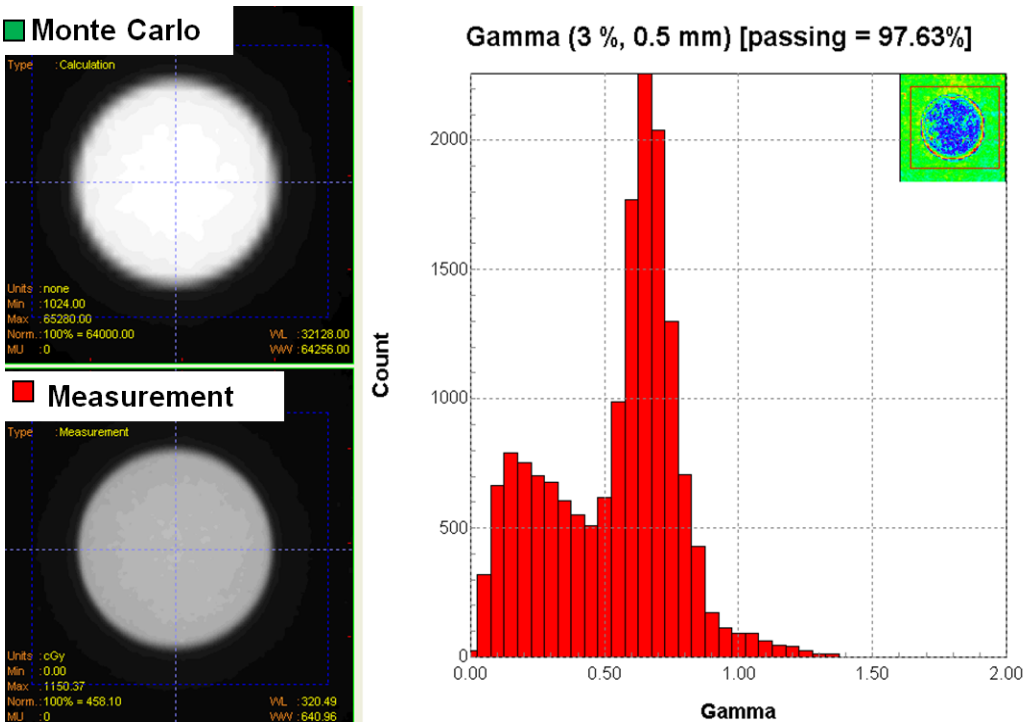

Figure 3.23: Anterior to posterior single beam irradiation. Gamma map for 3%/0.5 mm gamma criteria indicating 97.63% passing rate.

3.7 A study of dose deposition in various materials with Monte Carlo

In order to study dose deposition in various materials relative to solid water, the 3D phantom shown in Figure 3.24 was created in DOSXYZnrc. The phantom size was composed of four 4x4x4 cm^3 slabs. The three bottom slabs are solid water, each with a thickness of 1 cm (4x4x1 cm^3). The top slab consists of two parts, half an interchangeable heterogeneous material (air, lung, adipose, bone, inner bone and cortical bone) and half solid water (2x4x1 cm^3). A 20 mm field size phase space file was used to compute dose in this phantom by varying heterogeneous tissue density (cortical bone, muscle, lung, air, adipose, and inner bone). The number of histories used in simulation was increased until the uncertainty of each voxel was within 3% for the inner beam. The dose resolution was 2x2x1 mm^3 along x, y, z axis, respectively.

Figures 3.25 - 3.30 show isodose lines through the central axis of the heterogeneous phantoms computed by DOSXYZnrc for a 20 mm diameter field. The isodose lines are normalized to the maximum dose in the phantom. Dose in heterogeneous tissue was compared to dose in solid water at depth of 5 mm, and at a 2 mm lateral distance from the central axis. This procedure was repeated for all six heterogeneous tissues. The results provided in Table 3.5 show the relative dose ratios of heterogeneous materials to solid water. These findings indicate the necessity of a Monte Carlo treatment planning system for small animal irradiator, as the dose deposition varies with density of the tissues.

Heterogeneous slab	Density (g/cm^3)	**Dose ratio of heterogeneous tissue to solid water**
Air	0.001205	0.62
Lung	0.45	0.98
Adipose	0.92	0.81
Muscle	1.05	1.00
Spongy bone	1.12	1.58
Cortical bone	1.81	2.36

Table 3.5: Relative comparison of dose between the heterogeneous materials to solid water at 5 mm phantom depth for 20 mm field size.

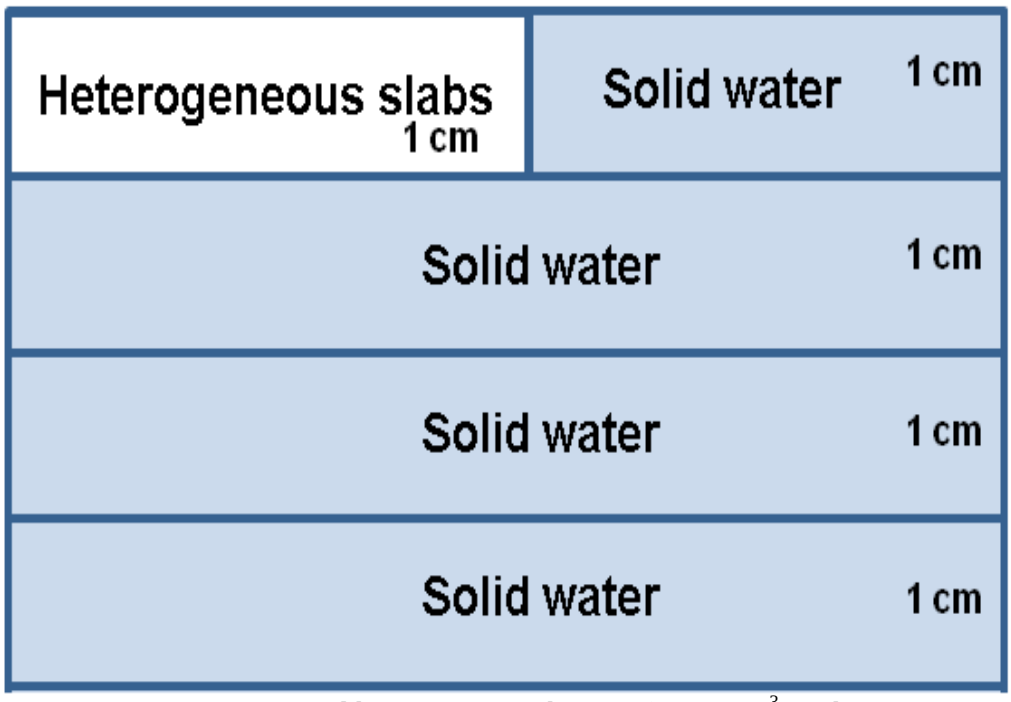

Figure 3.24: DOSXYZ virtual heterogeneous phantom (4x4x4 cm^3) with heterogeneous equivalent slabs (air, lung, adipose, muscle, inner bone, cortical bone and solid water) are simulated with 20 mm field size phase space for comparing dose between solid water to heterogeneous equivalent slabs at same depth.

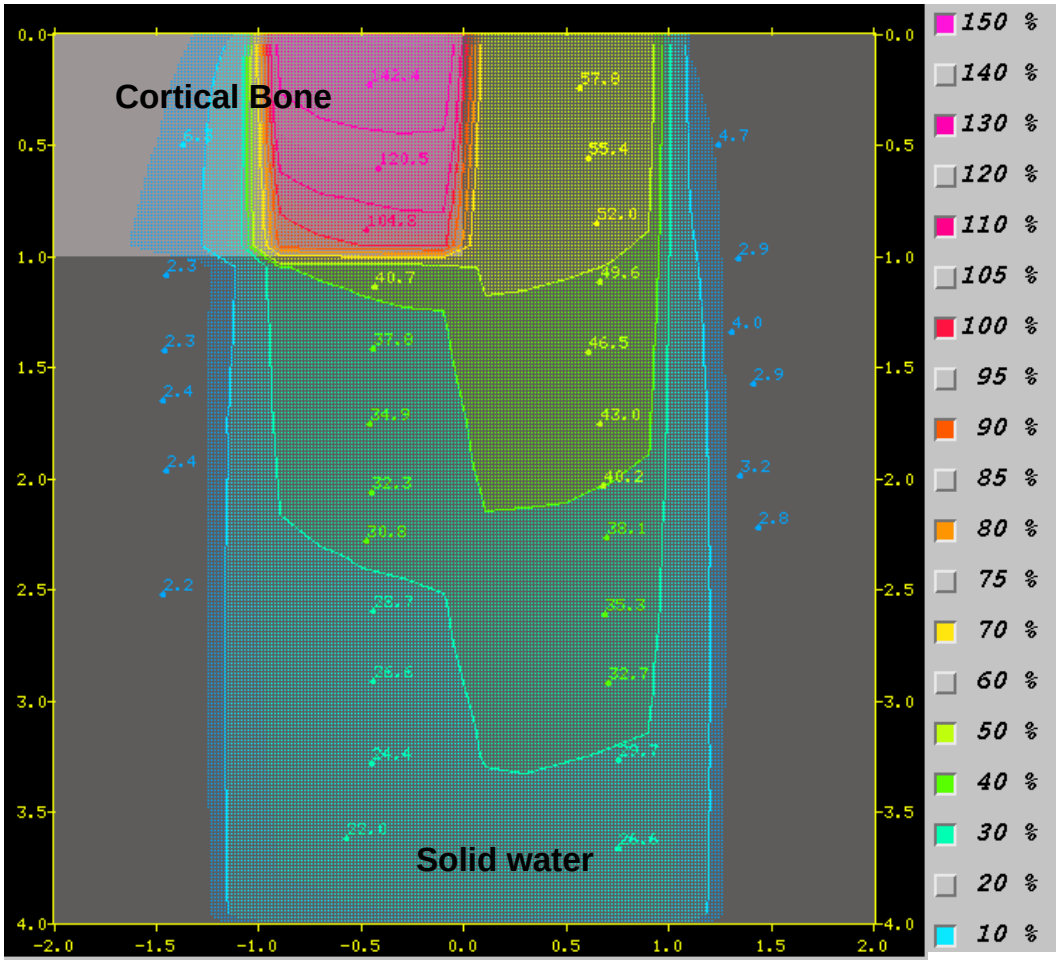

Figure 3.25: Heterogeneous phantom composed of cortical bone and solid water.

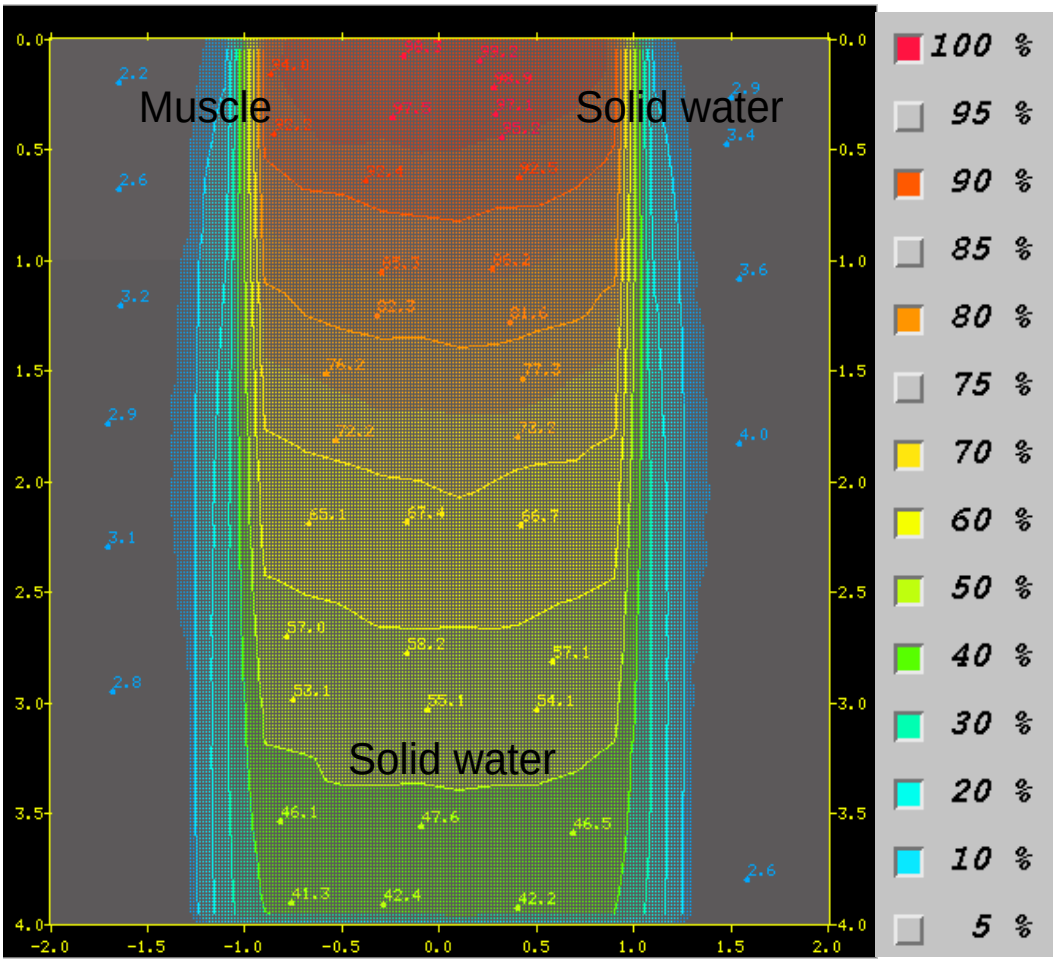

Figure 3.26: Heterogeneous phantom composed of muscle and solid water.

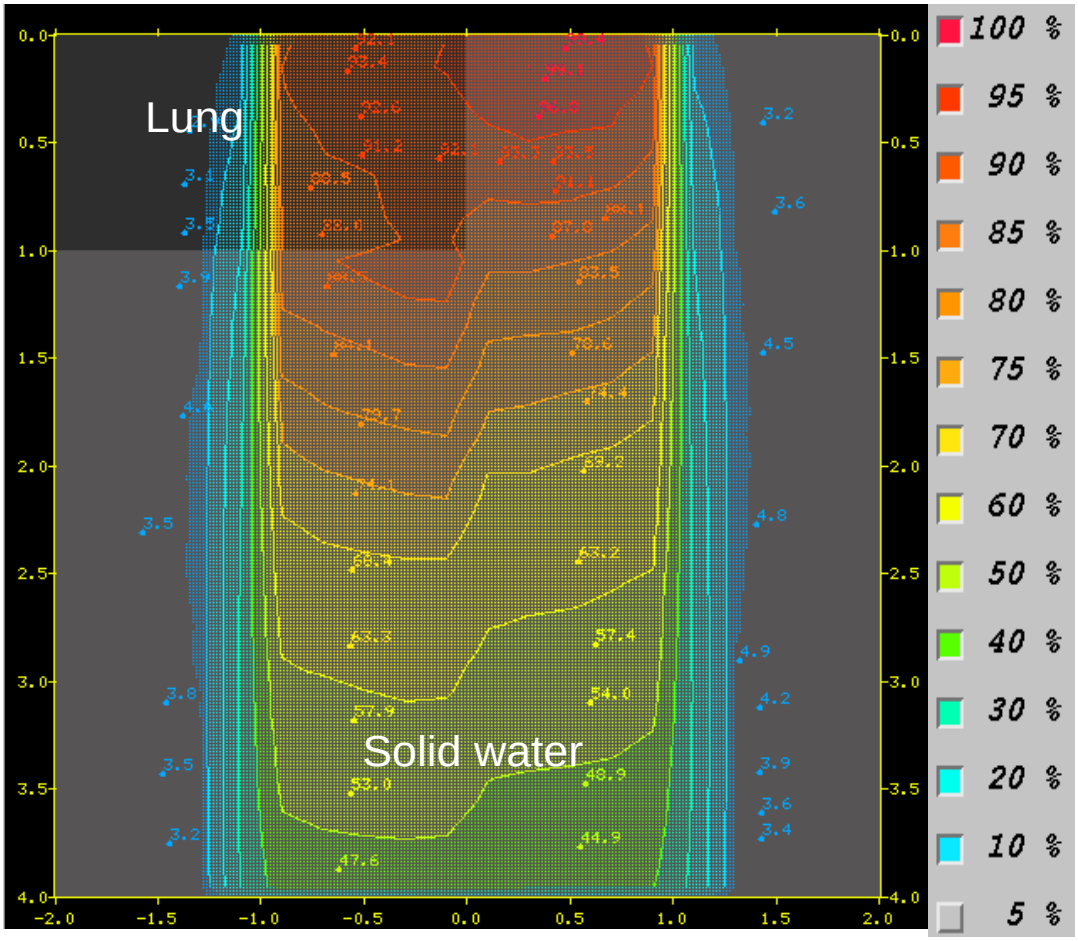

Figure 3.27: Heterogeneous phantom composed of lung and solid water.

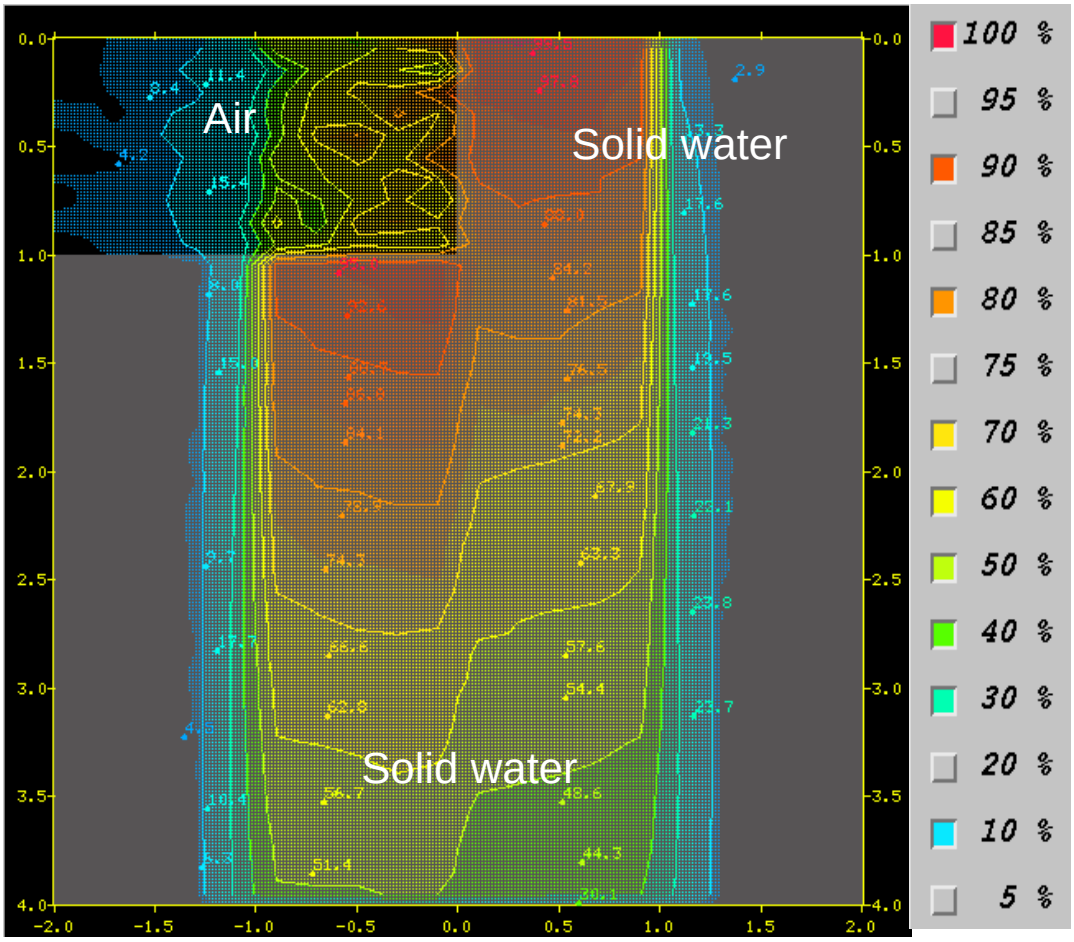

Figure 3.28: Heterogeneous phantom composed of air and solid water.

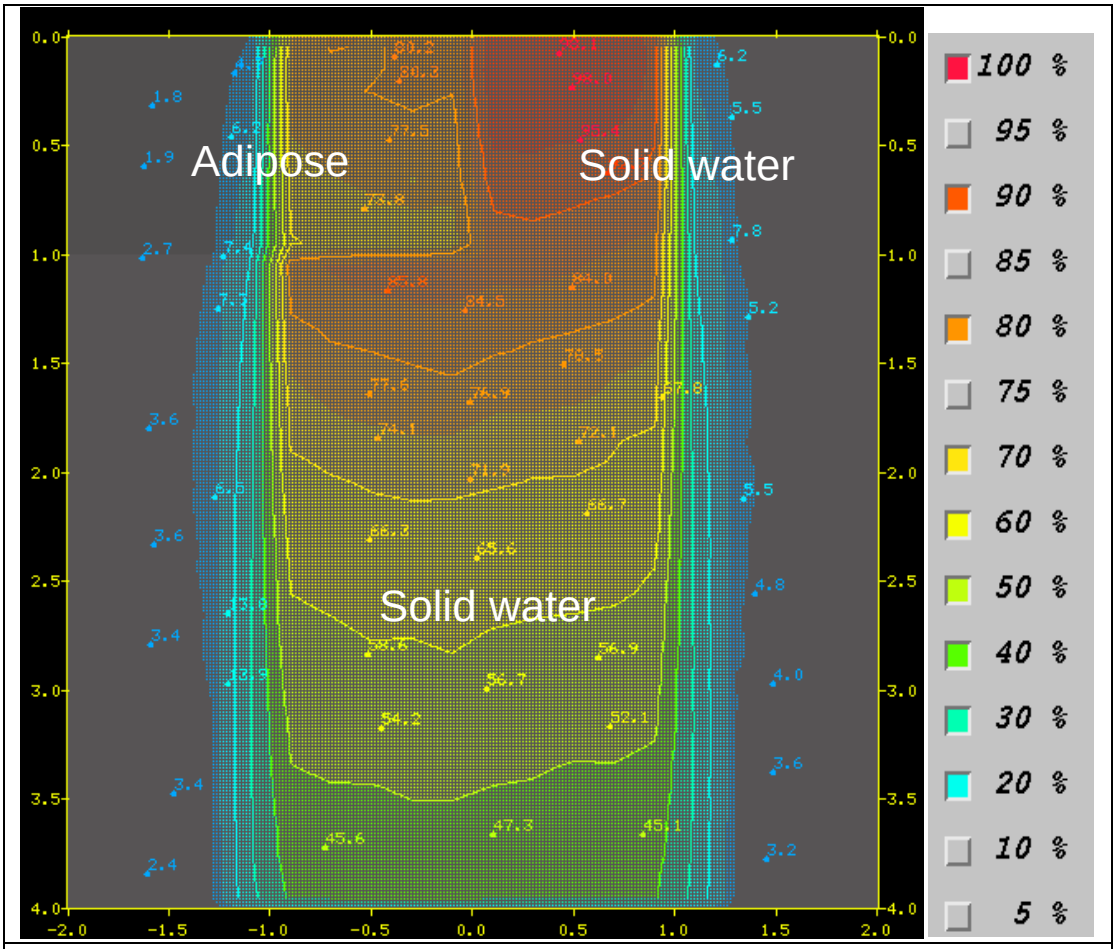

Figure 3.29: Heterogeneous phantom composed of adipose and solid water.

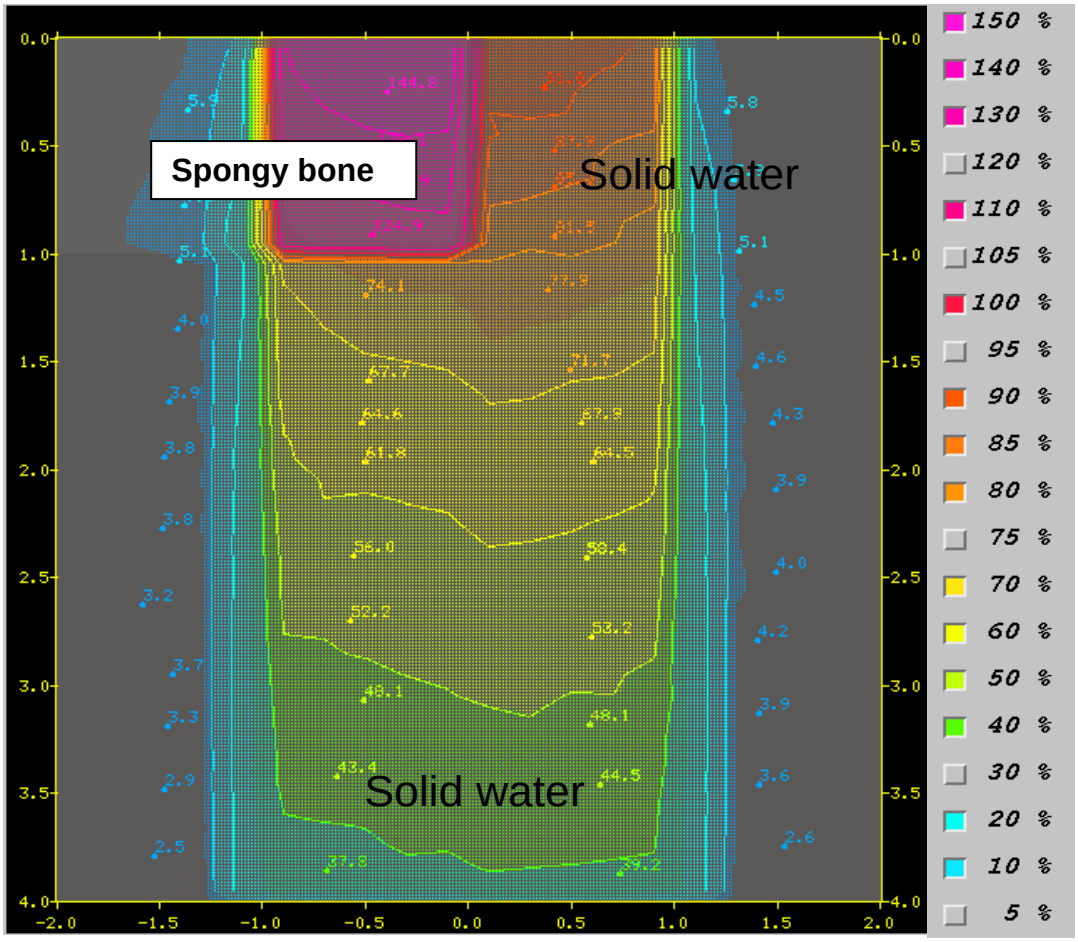

Figure 3.30: Heterogeneous phantom composed of spongy bone and solid water.

3.8 Validation of Monte Carlo source model in heterogeneous medium

Radiation dose deposition in tissue such as lung, muscle, adipose and cortical bone depends on the atomic number and density of the material. In the kV energy range, photoelectric and Compton are the dominant photon interactions (Chow, 2010, Khan, 1993). High Z material such as bone produces significant photoelectric interactions resulting in higher dose deposition in the bone. The objective of this part of the study is to benchmark the Monte Carlo beam model in heterogeneous media, quantitatively comparing calculation and measurement.

Benchmarking the model in heterogeneous media was performed in two steps. A heterogeneous phantom (4x4x4 cm^3) composed of solid water and cortical bone was constructed. The phantom consisted of a 1 cm slab of solid water, three 2 mm thick slabs of cortical bone, and three 1 cm slabs of solid water. EBT2 film was cut to 4x4 cm^2 pieces, marked for orientation and sandwiched between these slabs. The phantom was exposed using a 10 mm diameter circular field applicator for 2 minutes at 225kVp, 13mAs irradiator settings and 30.5 cm SSD. 24 h following irradiation, the exposed films were scanned in the same orientation using the EPSON 1000 XL scanner at 150 dpi. The orthovoltage calibration curve (225 kVp) was used to convert the optical density to dose.

An identical solid water – bone configuration was created in DOSXYZnrc with the exception that film between the bone slabs was omitted (Figure 3.31). The 10 mm field size phase space file from BEAMnrc for was used to compute the 3D dose distribution. The simulations were run until the uncertainty in the inner beam of the 3D matrix was within 2.5%. The 3D dose file was imported in MATLAB; four central pixels were averaged at each film depth to obtain the dose information. The PDD curve was

obtained by normalizing the depth dose data to the surface dose. The resulting dose distributions from MC were plotted against measurement.

A comparison of depth dose between measured and simulated data in water for the 10 mm circular field size at 225 kVp photon beam is shown in Figure 3.32. The MC simulation indicates that there is a 2.4 times increased dose deposition in cortical bone, in agreement with published data (Johns and Cunningham, 1983). This increased dose deposition, however, was not observed in film measurements.

To investigate the discrepancy between calculation and measurement, a second MC simulation was performed. For this purpose a new virtual phantom was created with EBT2 films sandwiched between cortical bone slabs to mimic the exact measurement conditions (Figure 3.33). This DOSXYZnrc simulation revealed no increased dose deposition in the film layers sandwiched between cortical bones slabs, in agreement with the previous measurements (Figure 3.34). The explanation for this finding is that secondary electrons from the primary beam generated in cortical bone have sufficiently low energy that they fail to reach the active layer of the film, that is, the thickness of the coated layer on the active layer of EBT2 film is greater than the range of secondary electrons generated from bone and also the tissue equivalence of the detector where photoelectric effect is not significant due to smaller atomic number compared to bone. The maximum range of the electrons this energy spectrum is 0.03 cm, which is equivalent to the thickness of the EBT2 film (0.029 cm).

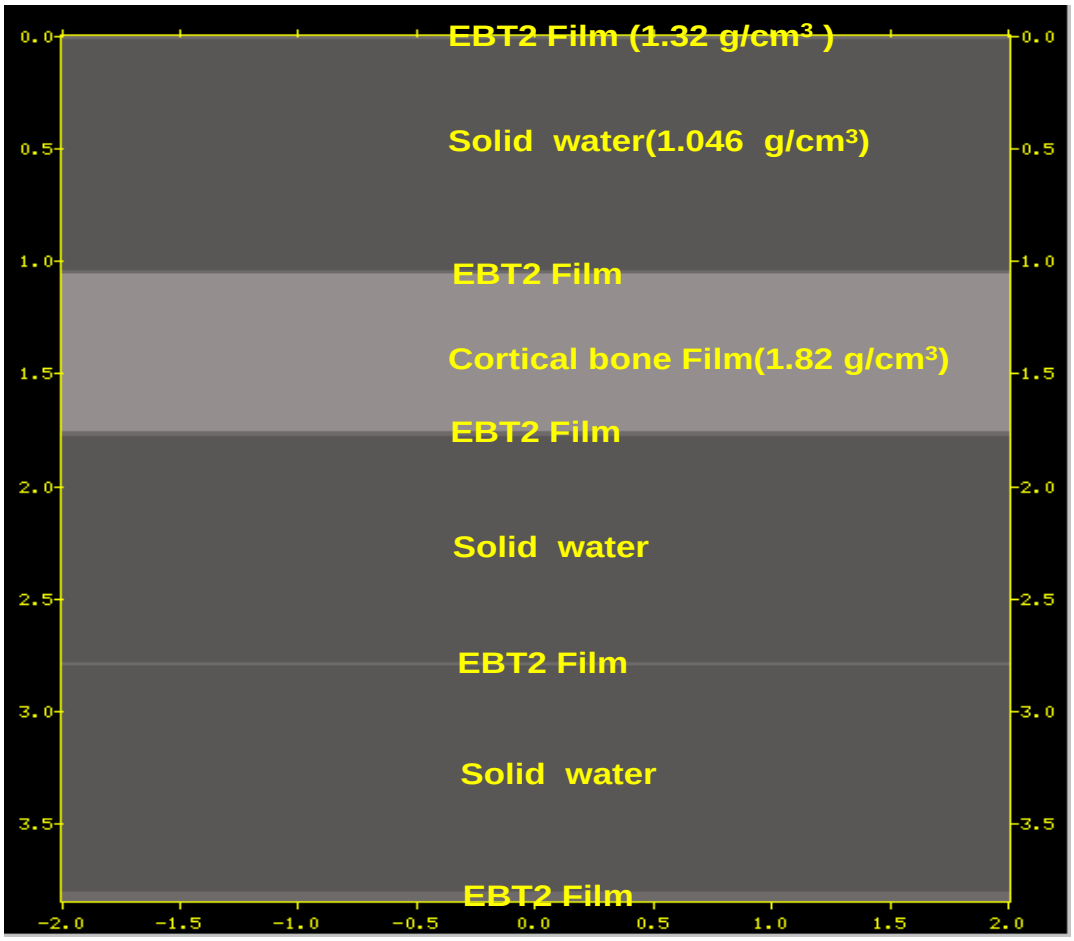

Figure 3.31: MC DOSXYZ virtual heterogeneous density phantom composed of solid water, cortical bone and EBT2 film slabs.

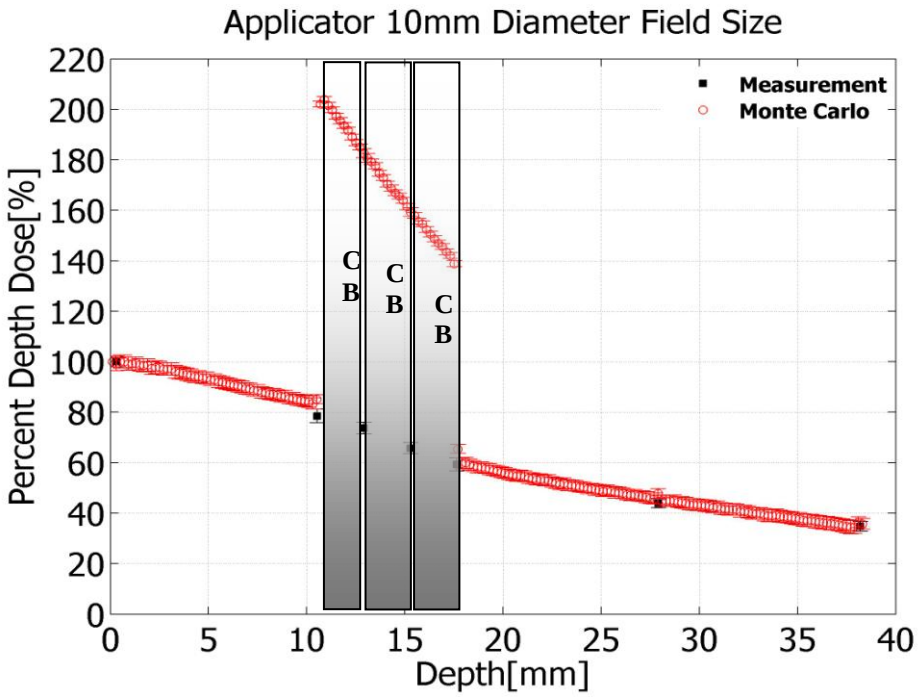

Figure 3.32: PDD curves for calculated and measured (film) 10 mm field size in virtual heterogeneous density phantom (Figure 2.5). CB: Cortical Bone

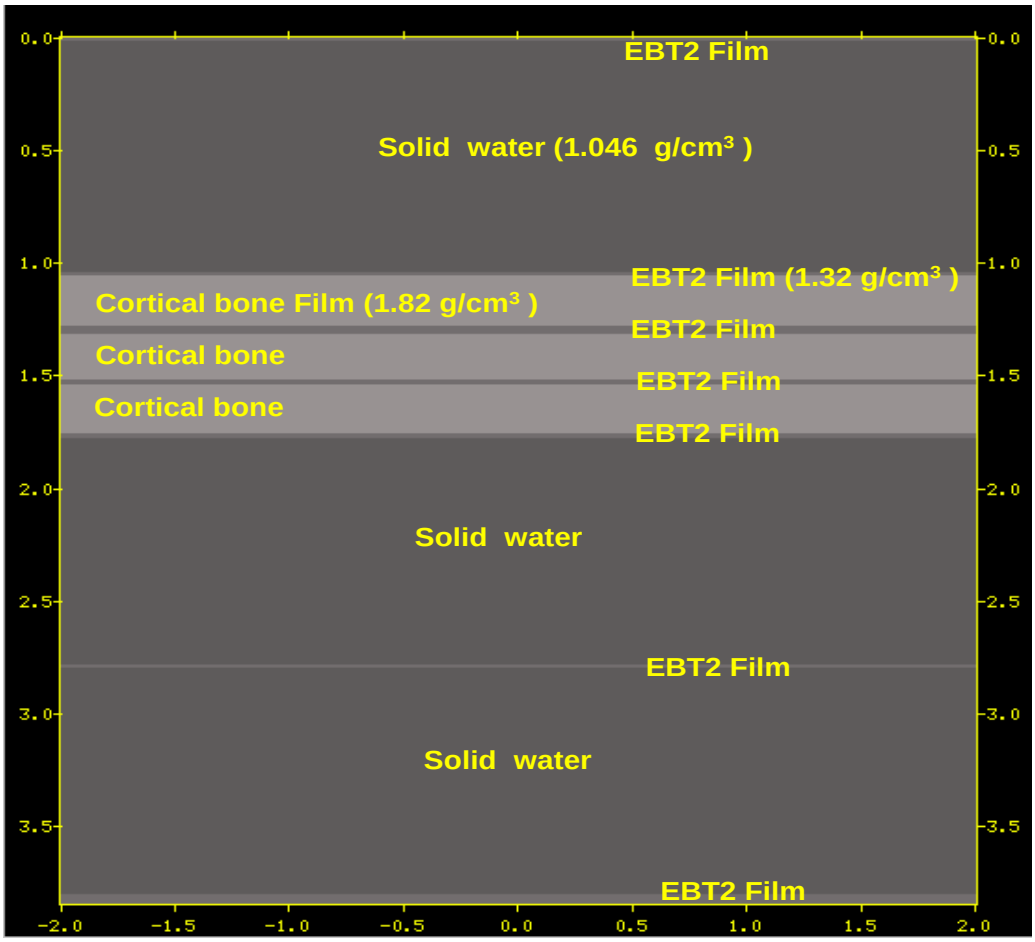

Figure 3.33: DOSXYZ virtual heterogeneous density phantom composed of solid water, cortical bone and EBT2 film slabs.

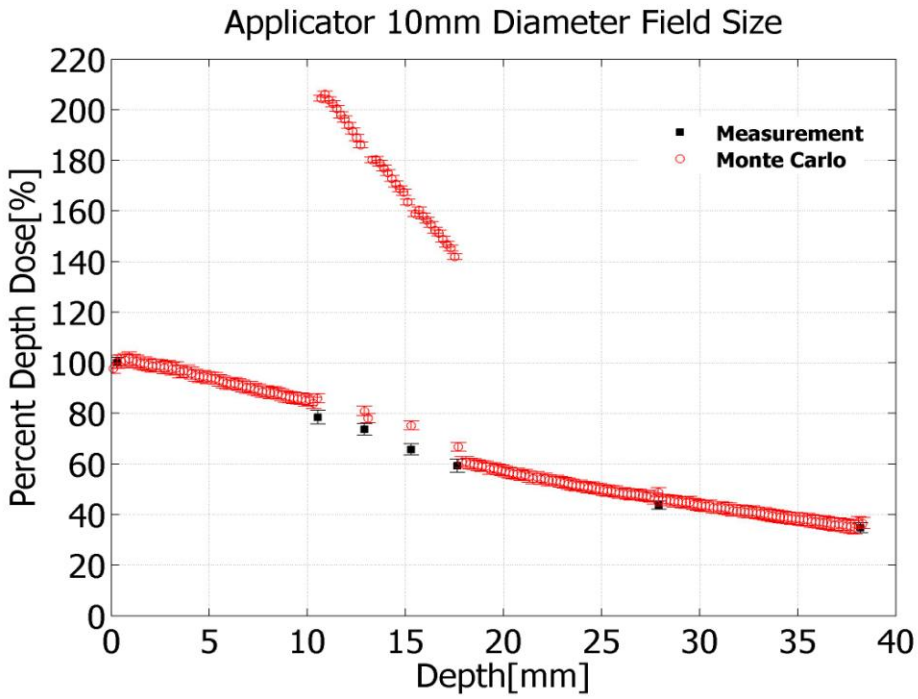

Figure 3.34: PDD curves for calculated and measured (film) 10 mm field size in virtual heterogeneous density phantom (Figure 3.26).

3.8.1 Gamma analysis in heterogeneous medium

Heterogeneous conditions were further validated using the phase space file for the 20 mm circular applicator. A 4x4x4 cm^3 phantom was created containing a heterogeneous material of 2x4x1 cm^3 insert composed of 1 mm solid water, 6.5 mm cortical bone and 2.5 mm inner bone and 2x4x1 cm^3 solid water, followed by three, 1 cm thick solid water slabs (Figure 3.35). EBT2 film was placed at depth of 10 mm of the heterogeneous phantom and aligned the center of the phantom to the beam axis. The film was exposed at 250kVp, 13 mAs and 30.5 cm SSD irradiator settings for 120 seconds with 20 mm field size applicator.

An identical configuration was created in DOSXYZnrc using materials of known physical density. A calculation grid 4x4x4 cm^3 was used, and the resulting dose distribution scored at a depth of 10 mm is shown in Figure 3.35.

The simulation result and film measurement were processed in MATLAB and exported to Film QA tool for gamma analysis. The AAPM TG53 protocol recommendations were used to benchmark simulation data with the measurement in heterogeneous medium (Fraass et al., 1998b). In a heterogeneous medium, the recommended acceptability criterion for the inner beam is 3%. The penumbra should be within 5 mm and the outer beam within 5%. A comparison of isodose lines is shown in Figure 3.36. Dose profiles show agreement within 3% in the high dose region i.e. within the inner beam as shown in Figures 3.37- 3.38. The discontinuity on the central axis is due to radiation streaming through the two halves of the phantom. Agreement in the outer beam region is within 5%. The reason for the relatively large dose difference in outer beam region, where dose is primarily from scatter, is due to over response of the film

(Butson et al., 2010). Gamma analysis was performed and the result of the analysis for a confined region is shown in Figure 3.39. The single beam with 20 mm diameter circular field irradiation demonstrates a good agreement within the region of interest, with 94% of the calculated data meeting the 5%/0.5 mm criterion.

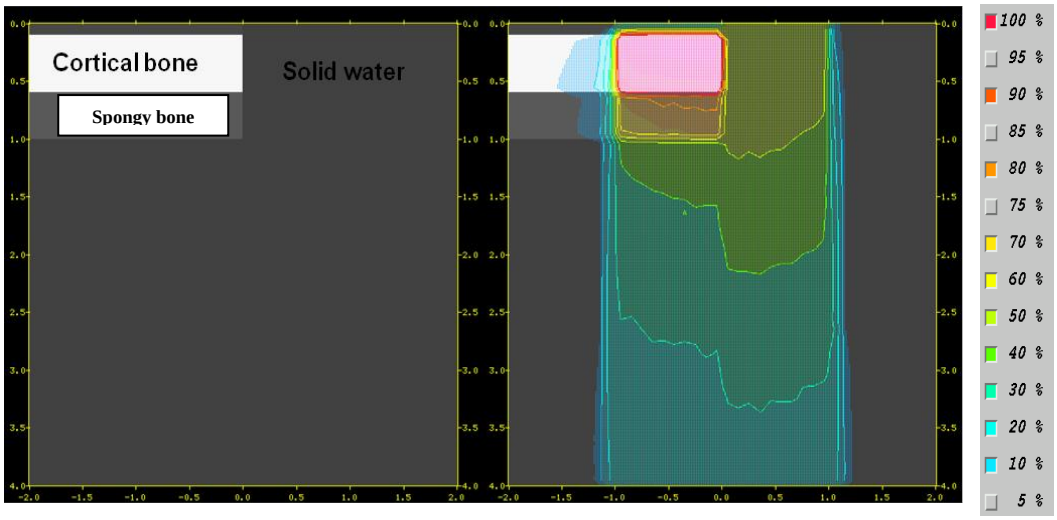

Figure 3.35: DOSXYZ virtual heterogeneous density phantom with equivalent slabs solid water, cortical bone and inner bone. Each dose point in 3D hetero phantom is normalized to maximum dose in the cortical bone. Dose uncertainty for each point in simulation is 0.5 to 2.0 % with maximum 7% uncertainty outside the beam view.

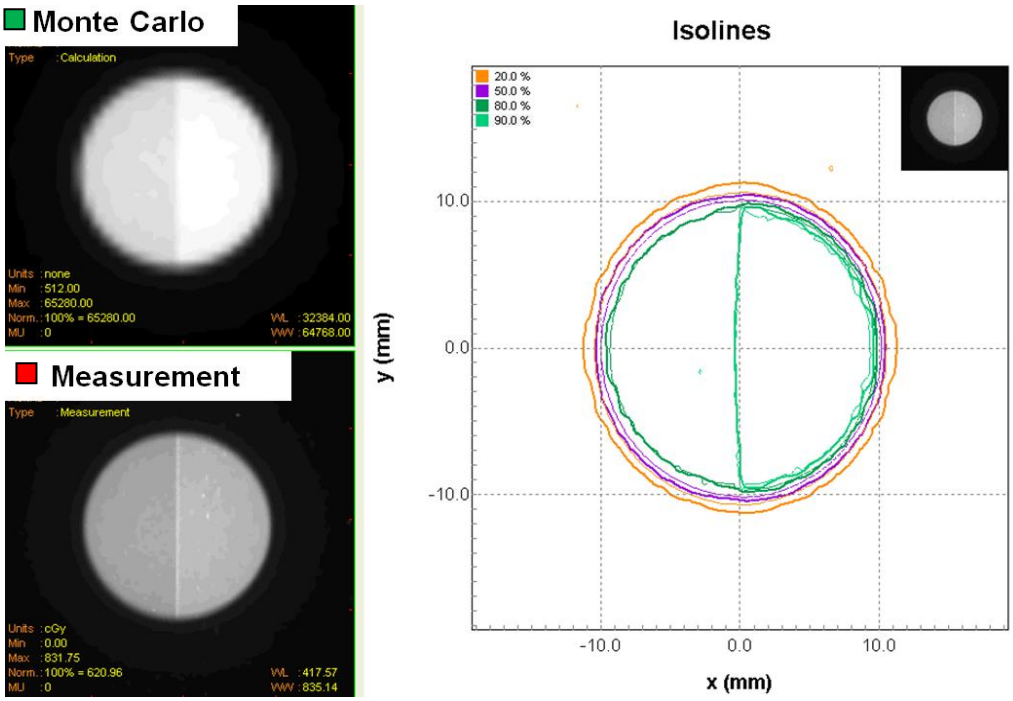

Figure 3.36: Calculated and measured isolines at 225 kVp from 20 mm field size at 1 cm depth. Thin isodose lines correspond to measurement and thick lines to Monte Carlo.

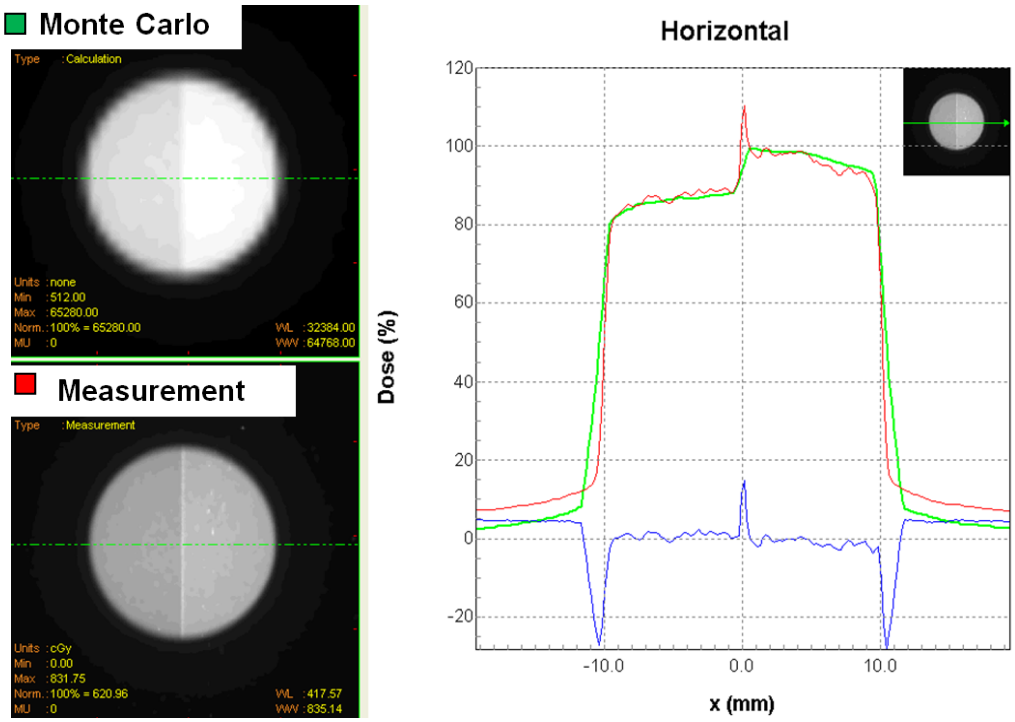

Figure 3.37: Calculated and measured horizontal dose profile at 225 kVp from 20 mm diameter circular field size at 1 cm depth.

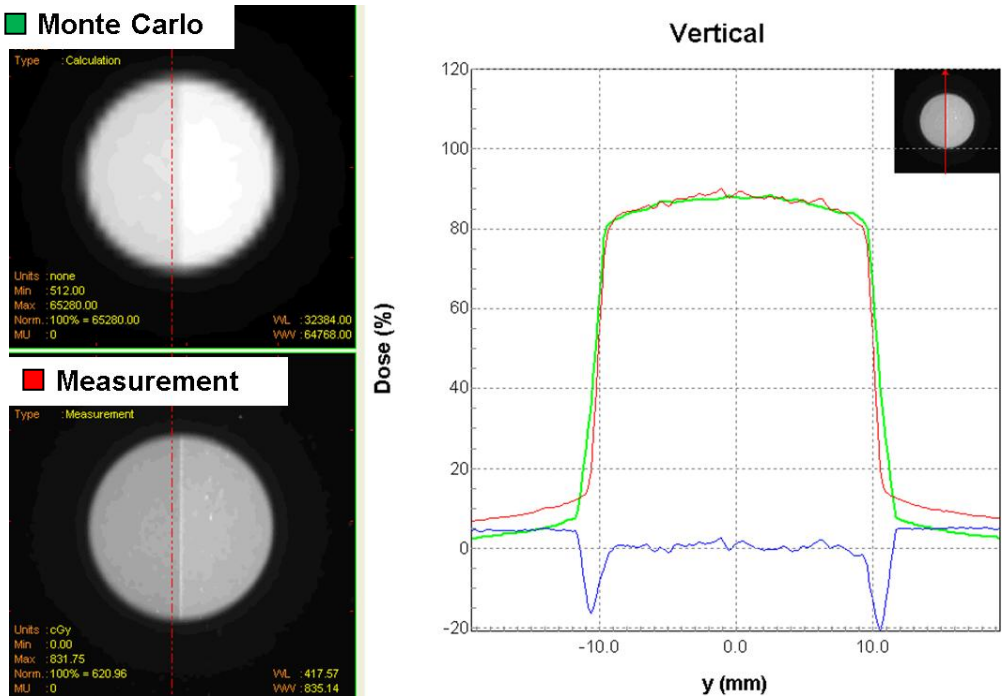

Figure 3.38: Calculated and measured vertical dose profile at 225 kVp from 20 mm diameter circular field size at 1 cm depth.

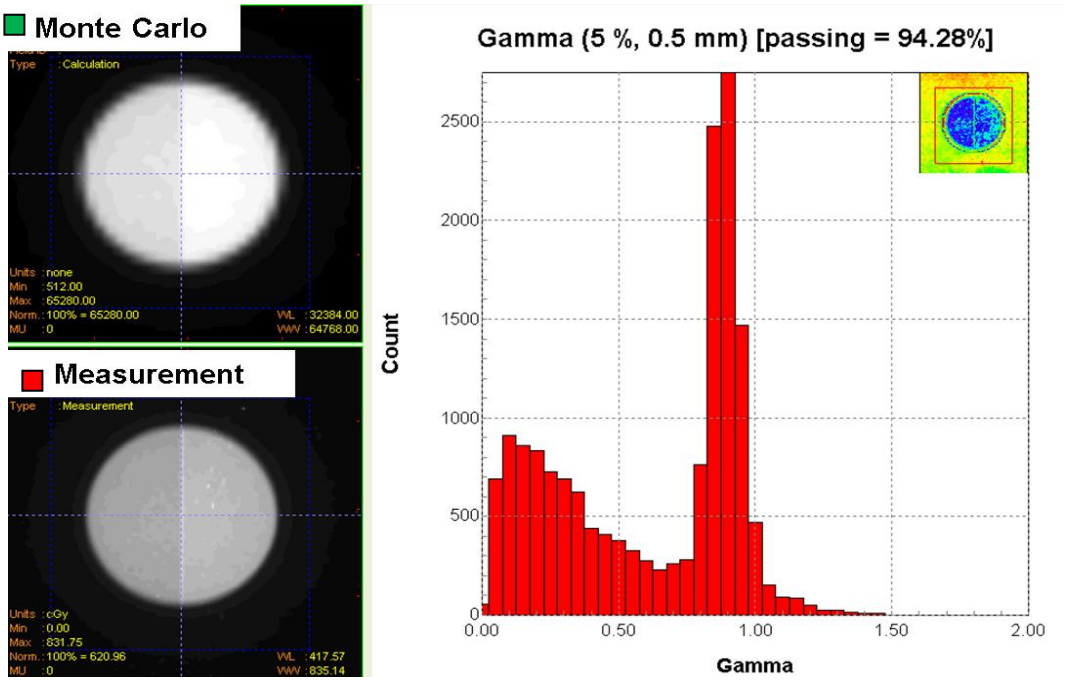

Figure 3.39: Anterior to posterior beam delivery single irradiation. Gamma map tested to 5%/0.5 mm criteria, Where 94.28% of the data passed.

3.9 Off -axis spectrum analysis

The superior resolution of film makes it a suitable dosimeter for small field dosimetry. For field sizes larger than 10 mm, the profile measurements between the ionization chamber and EBT2 film show a disagreement in the outer beam region. Figure 3.40 shows Monte Carlo calculated results for a 20 mm field size compared to ionization chamber measurements. While they agree within 1 % for both inner beam and outer beam of the profile, a similar measurement using EBT2 film (Figure 3.21) yielded a disagreement of 2.18 % in the outer beam region as compared to Monte Carlo and ionization chamber measurements. This is due to the over response of EBT2 film for the low energy (25-100 keV photon equivalent energy) photons scattered outside the primary field (Butson et al., 2010). At orthovoltage energies, scatter radiation increases with respect to field size (Khan, 1993). Further experiments were performed to verify that the film indeed exhibits over response for larger field sizes at 225kVp. To study the scatter radiation outside the beam, Monte Carlo phase space files were processed using BEAM data processing tool (BEAMDP) to acquire the spectrum for different field sizes. Phase space files created to extract the spectrum from different scoring zones in the phase space plane. The plane was divided into two zones: zone 1 covers the scoring zones within the full width half maximum of the field size (r_1-r_n), while zone 2 covers the remainder of the scoring plane (x_1-x_n) for each field size (Figure 3.41).

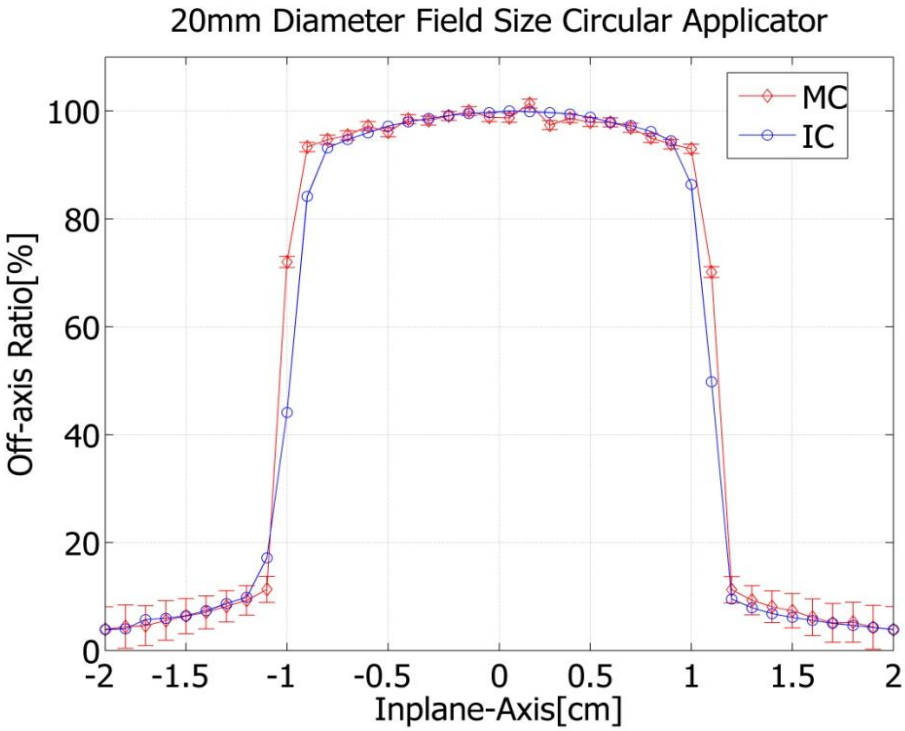

Figure 3.40: Beam-line profile measurements using pinpoint ionization chamber (blue line) and MC simulation result (red line) of 20 mm diameter field size circular applicator are shown above. Each profile is normalized max dose.

Two additional photon spectra were scored as a function of aperture size at the beam exit. 1, 5, 10 and 20 mm diameter circular field size spectra were derived as shown in Figures 3.42 and 3.43 for zone 1 and zone 2. In zone 1, photons were sorted into energy bins with bin width of 1.3 keV and averaged over a distance from the central axis to full width half maximum (Figure 3.41). Similarly, zone 2 photons were averaged over a distance which covered the tail of the beam profile. The average energy of the spectrum for each field size in zone 1 was 84.7 keV. However, the average energy of the spectrum in zone 2 was field size dependent. There is a decrease in average energy for 5 mm to 20 mm field size from 79 keV to 61 keV in zone 2. As the field size is increased, there is an increase in the lateral scatter with low energy photons, and a corresponding decrease in average energy (Figure 3.43).

Quantitative analysis to study the over response of the film to the low energy photon scatter was performed by determining the appropriate photon equivalent energy (effective energy) for each spectrum in Zone 1 and Zone 2 in terms HVL. For the spectrum in zone 1, the simulated HVL was 1 mm Cu with a photon equivalent energy 80 keV. The 20 mm field size spectrum in zone 2 was used to calculate the half value layer in MC. The result found was 0.5 mm Al with a photon equivalent energy of 40 keV. The corresponding energy over response for the EBT2 film at 80 keV and 40 keV are 1.01 and 1.04 (Butson et al., 2010). This result is in agreement with margin of error 1% that is observed in the film measurements presented above.

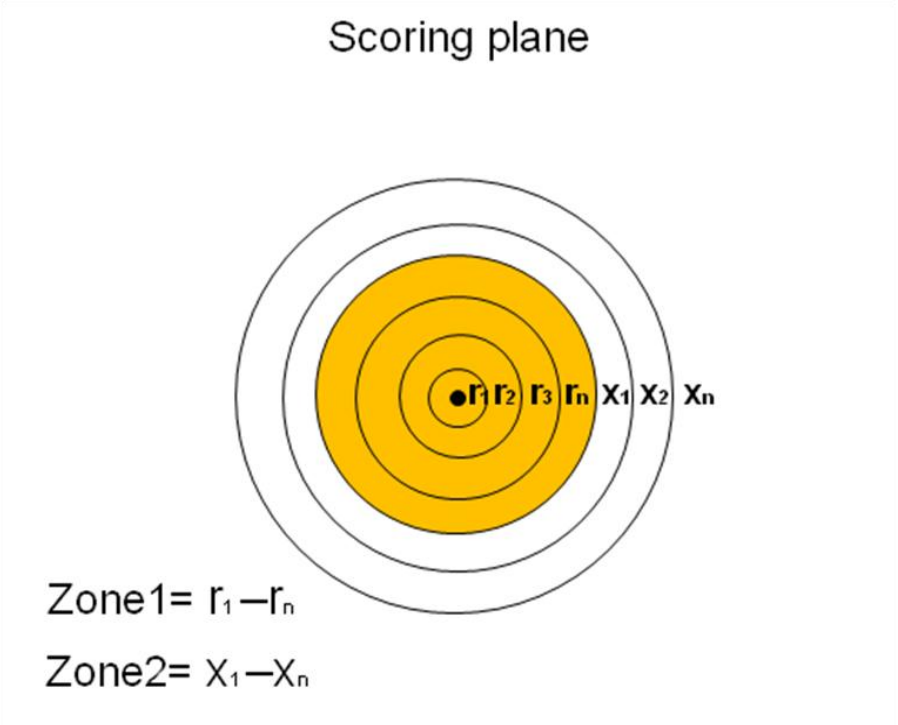

Figure 3.41: Each applicator scoring plane was divided into zones; zone1 covered the full-width half maximum of the beam from the central axis (color: yellow), whereas zone 2 covered the rest of the scoring plane (color: white).

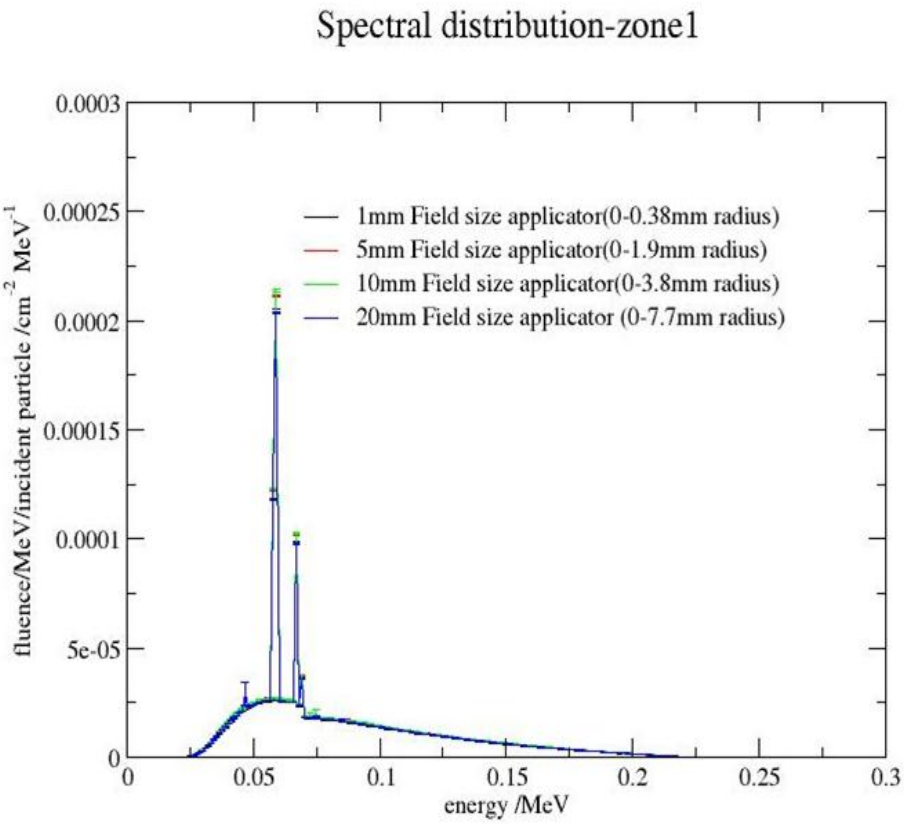

Figure 3.42**:** Spectral distribution for zone1 at SSD of 23.5 cm for 1,5,10 and 20 mm field sizes.

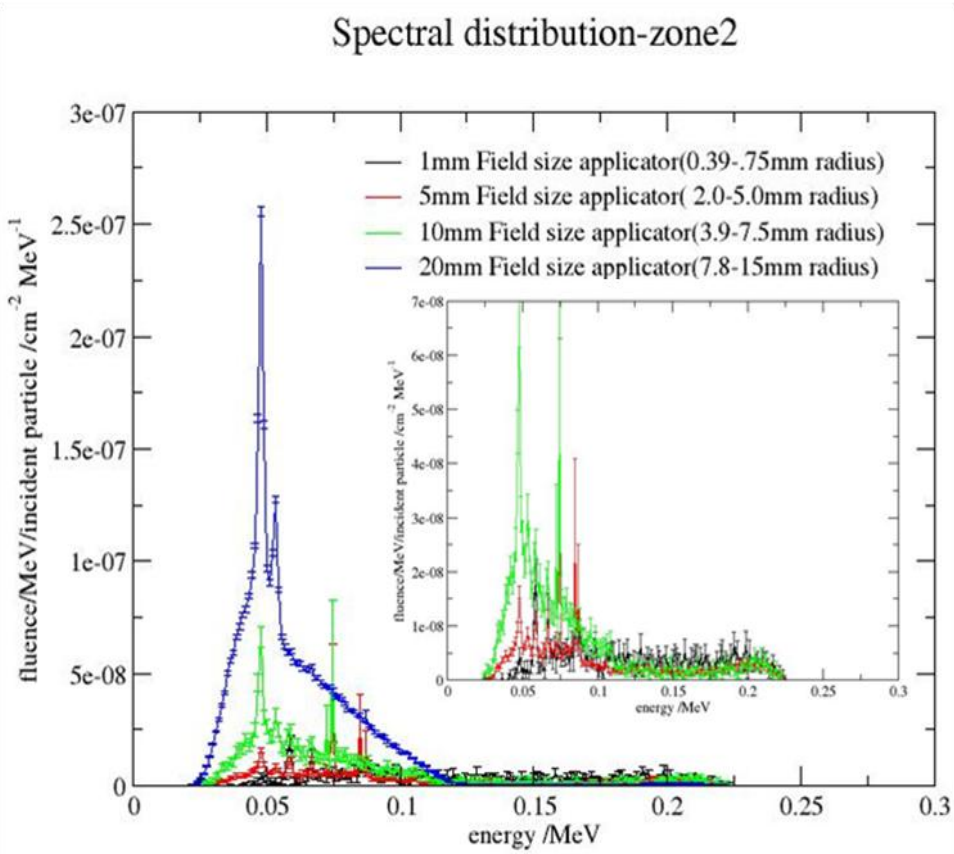

Figure 3.43: Spectral distribution for zone2 at SSD of 23.5 cm for 1,5,10 and 20 mm field sizes.

3.10 Output factors

The EGSnrc/BEAM Monte Carlo code was used to calculate output factors for XRAD 225Cx irradiator. Monoenergetic 225 keV electrons were simulated to impinge on a rectangular focal spot of 3.54 mm wide by 2.94 mm in length. The focal spot dimensions were provided by manufacturer. Figure 3.44A and Figure 3.44B shows the schematic of the simulation geometry. Simulations were performed in two stages. In the first stage a large phsp file (~4.3 GB) was generated above the collimating system (applicators). In the second stage, the phsp file was used as a source to calculate dose in the water phantom. The Monte Carlo transport parameters used for OF simulations are provided in Table 3.2. All simulations were performed in BEAMnrc using the DBS variance reduction technique. An individual phase space file, containing $1.6x10^9$ particles, was created below the monitor chamber at a distance of 9.08 cm from the source (The maximum number of particles cannot exceed $(2^{32}-1)$ in one phase space file). This phsp was used as a virtual source for output factors calculations in water medium as shown in Figure 3.48B. Particles were sampled from the phsp file and further transported through each applicator and into a water phantom to calculate dose. Each field size simulation was performed independently with the same source. In the second stage of the simulation in which particles were transported through the applicator, no further DBS was used. Dose was calculated in water using the CM called chamber as phantom. This component module was used to calculate the dose along the central axis of the beam at 30.5 cm SSD.

A 5.0 mm diameter dose scoring detector was used for all square and circular collimators, with the exception of circular field sizes less than 10 mm in diameter. The

40x40 mm^2 field size was used as a reference collimator. For field sizes less than or equal to 3.5 mm, the dose scoring detector diameters were 1.75, 1.25 mm and 0.5 mm for the 5 mm, 3.5 mm, 2.5 mm and 1.0 mm field sizes, respectively.. The 10 mm field size was used as an intermediate reference for smaller fields. Using the same phsp file for each field size, dose was scored along the central axis of the beam. In the orthovoltage energy range, electron contamination contributes to the dose at shallow depths. For that reason TG-61 protocol recommends water phantom calibration be performed at 2 cm depth. We extended the TG 61 recommendation to output factor measurements, i.e., OFs were measured at both the surface and at a depth of 2 cm depths. For large field sizes, output factors were calculated using equation 3.3, while for field sizes less than 10 mm, output factors were calculated using equation 3.4.

$$OF(fs,d) = \frac{\frac{D(fs,d)}{PDD(fs,d)}}{\frac{D(fs_{ref},d)}{PDD(fs_{ref},d)}} \tag{3.3}$$

$$OF(fs,d) = \frac{\frac{D(fs,d)}{PDD(fs,d)}}{\frac{D(fs_{10},d)}{PDD(fs_{10},d)}} * \frac{\frac{D(fs_{10},d)}{PDD(fs_{10},d)}}{\frac{D(fs_{ref},d)}{PDD(fs_{ref},d)}} \tag{3.4}$$

where *fs* is the diameter [mm] of a circular field or side [mm] of a square field, *d* [cm] indicates the measurement depth in water, *D* is the dose [Gy], and fs_{ref} is 40x40 mm^2 field size applicator used as a reference field size, fs_{10} is the 10 mm diameter collimator used as intermediate reference for smaller field sizes. The output factor at each depth requires a

PDD value at that depth for calculations from their respective sources such as Monte Carlo simulations or measurements.

Output factors were measured using two independent techniques, using a pinpoint ionization chamber in water, and Gafchromic EBT2 film in a solid water phantom. For all square fields and circular field sizes greater than or equal to 10 mm diameter, a pinpoint ionization chamber was utilized using the same setup as described for absolute dose calibration, with an exposure time of 60 seconds with 225 kVp, 13mAs irradiator settings at surface and 2 cm depth. For all field sizes, film measurements were performed at the surface and 2 cm depth of a phantom 10x10x12 cm^3 solid water using EBT2 Film (Lot#A12091301) with exposure time of 120 sec with 225 kVp and 13mAs. Film measurements were repeated three times to provide an estimate of the uncertainty. The optical density of the film was converted to dose in MATLAB using 225 kVp calibration curve given in Chapter 2. Output factors calculated at two depths using equation 3.3 and equation 3.4 are given in Tables 3.5 and 3.6.

Table 3.5 shows a comparison of output factors for circular and square fields from the 225kVp beam at the surface of the phantom. Overall agreement is within 2% between the Monte Carlo calculated results and the measurement (Film and IC) calculated output factors for all field sizes. The output factor values, as expected, decrease as the field size decreases. Table 3.6 shows a similar comparison for output factors determined at a 2 cm depth. Good agreement exists between the simulation and measurements, i.e. less than 3% for all field sizes except for 2.5 mm and 1 mm, with 3.11% and 11 % agreement, respectively. Comparison of the output factor values at the surface relative to 2 cm depth poorer agreement (3-5%). This is not unexpected, as the

electron component contribution to the beam creates significant uncertainty in surface measurements. For a system of dosimetric calculations, a reference depth of 2 cm is therefore recommended.

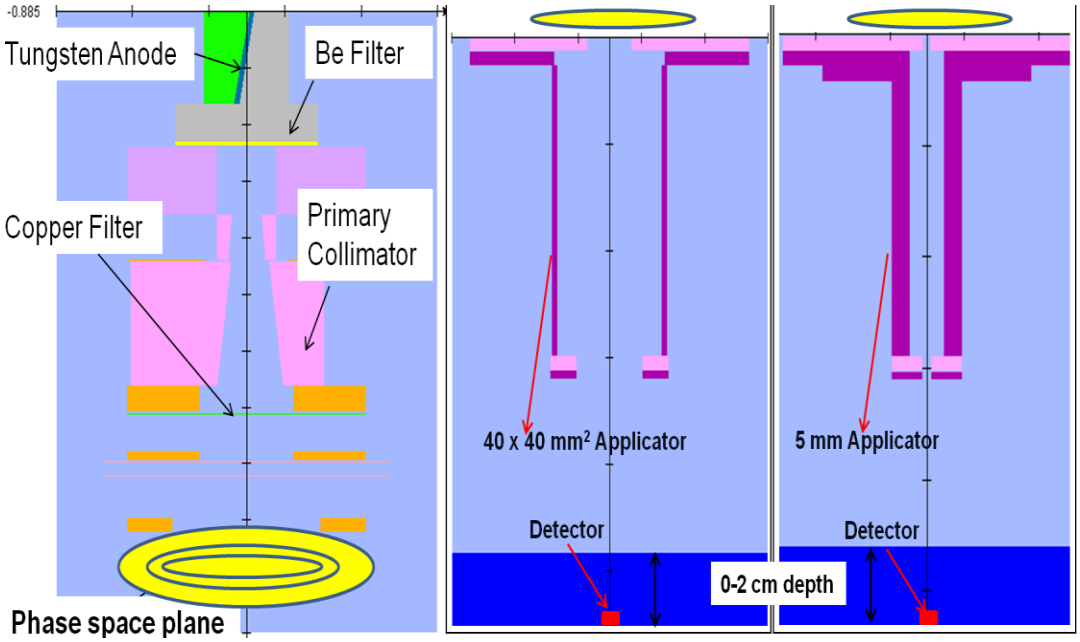

Figure 3.44: A) Schematic of the MC model for the XRAD225cx small animal irradiator. Indicated are BEAM Component Modules as the tungsten anode (XTUBE), beryllium filter (SLABS), primary collimator (PYRAMIDS), Cu filter (SLABS) and phase space plane at the end of the design.
B) Using the same space plane a source for MC simulation for output factors with BEAM Component Modules as square applicators (PYRAMID), 1-20mm applicator with (CIRCAP) were used in the model.

Total scatter factor (S_{cp}) with electron contamination							
Circular field applicators							
Dosimeter	20 mm	15 mm	10 mm	5 mm	3.5 mm	2.5 mm	1 mm
Ionization Chamber	0.924	0.910	0.887		NA		
EBT2 Film	0.924	0.896	0.877	0.861	0.814	0.808	0.565
Monte Carlo	0.936	0.913	0.883	0.843	0.815	0.807	0.692
Difference (%)							
MC vs IC	-1.36	-0.40	0.45		NA		
MC vs Film	-1.30	-1.94	-0.64	2.07	-0.12	0.11	18.36

Square field applicators				
Dosimeter	40x40 mm^2	20x20 mm^2	15x15 mm^2	10x10 mm^2
Ionization Chamber	1.0	0.944	0.924	0.896
EBT2 Film	1.0	0.937	0.916	0.894
Monte Carlo	1.0	0.951	0.926	0.908
Difference (%)				
MC vs IC		0.67	0.29	1.32
MC vs Film		-1.42	-1.11	-1.54

Table 3.5: The total scatter factors relative to the reference 40 x40 mm^2 square field size measured with a Gafchromic EBT2 film and pinpoint N31014 ionization chamber (IC) at surface. They were compared against Monte Carlo calculated result.

Total scatter factor (S_{cp}) without electron contamination							
Circular field applicators							
Dosimeter	20 mm	15 mm	10 mm	5 mm	3.5 mm	2.5 mm	1 mm
IC	0.911	0.891	0.866		NA		
EBT2 Film	0.917	0.911	0.889	0.837	0.792	0.784	0.544
Monte Carlo	0.922	0.912	0.891	0.862	0.808	0.809	0.611
Difference (%)							
MC vs IC	1.15	2.36	2.87		NA		
MC vs Film	0.57	0.11	0.22	-2.99	-1.97	-3.11	-11.02
Square field applicators							
Dosimeter		40x40 mm^2	20x20 mm^2		15x15 mm^2	10x10 mm^2	
IC		1.000	0.909		0.888	0.865	
EBT2 Film		1.000	0.943		0.925	0.902	
Monte Carlo		1.000	0.935		0.902	0.864	
Difference (%)							
MC vs IC			-2.80		-1.49	0.08	
MC vs Film			0.85		2.56	-2.77	

Table 3.6: The total scatter factors relative to the reference 40 x40 mm^2 square field size measured with a Gafchromic EBT2 film compared to pinpoint N31014 ionization chamber (IC) at 2 cm depth. They were compared against Monte Carlo (MC) calculated result.

3.11 Conclusion:

This study has investigated the feasibility of using the Monte Carlo method to develop a beam model of kV photon beams from the XRAD 225Cx irradiator. The EGSnrc/BEAMnrc MC code was used to simulate the entire geometry, from the X-ray tube to secondary applicators and various phantoms. Excellent agreement was observed between the energy spectrum obtained from MC simulation and that determined using the analytical modeling software package called Spekcalc. Measured and MC calculated half-value-layers (HVL) agree within 5%. Dosimetric characteristics including percent depth dose (PDD), output factors (OF), off-axis ratios (OAR), and penumbra were benchmarked against measurements. The comparison between MC and measured dose distributions was quantitatively validated using the gamma index method for various field sizes in both homogenous and heterogeneous situations

The field size dependent over-response effect of EBT2 film in the beyond penumbra region was further investigated and determined to be due to EBT 2 film over response to low energy photons. Output factor measurement with various dosimeters were benchmarked against simulations. Electron contamination creates significant uncertainty in surface measurements, and therefore a reference depth of 2 cm is recommended.

References

BIELAJEW, A. F. (ed.) 2006. The Monte Carlo Simulation of Radiation Transport. In: Integrating New Technologies into the Clinic: Monte Carlo and Image-Guided Radiation Therapy.: Madison: Medical Physics Publishing; 1-20.

BRIESMEISTER, J. 2000. MCNP – A general monte carlo n-particle transport code. Los Alamos: LA-13709-M.

BUTSON, M. J., YU, P. K. N., CHEUNG, T. & ALNAWAF, H. 2010. Energy response of the new EBT2 radiochromic film to x-ray radiation. Radiation Measurements, 45, 836-839.

CHOW, J. C. L. 2010. Depth dose dependence of the mouse bone using kilovoltage photon beams: A Monte Carlo study for small-animal irradiation. Radiation Physics and Chemistry, 79, 567-574.

FELLER, W. 1967. An Introduction to Probability Theory and Its Applications, Newyork, wiley.

FRAASS, B., DOPPKE, K., HUNT, M., KUTCHER, G., STARKSCHALL, G., STERN, R. & VAN DYKE, J. 1998a. American Association of Physicists in Medicine Radiation Therapy Committee Task Group 53: quality assurance for clinical radiotherapy treatment planning. Med Phys, 25, 1773-829.

FRAASS, B., DOPPKE, K., HUNT, M., KUTCHER, G., STARKSCHALL, G., STERN, R. & VAN DYKE, J. 1998b. American Association of Physicists in Medicine Radiation Therapy Committee Task Group 53: Quality assurance for clinical radiotherapy treatment planning. Medical Physics, 25, 1773-1829.

HUQ, M. S., SONG, H., ANDREO, P. & HOUSER, C. J. 2001. Reference dosimetry in clinical high-energy electron beams: Comparison of the AAPM TG-51 and AAPM TG-21 dosimetry protocols. Medical Physics, 28, 2077-2087.

JENKINS, T. M., NELSON, W. R. & RINDI, A. (eds.) 1988. Monte Carlo Transport of elcectrons and Photons

JOHNS, H. E. & CUNNINGHAM, J. R. (eds.) 1983. The Physics of Radiology, Springfield,IL .

KAWRAKOW, I., MAINEGRA-HING, E., ROGERS, D. W. O., TESSIER, F. & WALTERS, B. R. B. 2011. The EGSnrc Code System: Monte Carlo Simulation of Electron and Photon Transport. NRCC Report PIRS-701.

KAWRAKOW, I., ROGERS, D. W. O. & WALTERS, B. R. B. 2004. Large efficiency improvements in BEAMnrc using directional bremsstrahlung splitting. Medical Physics, 31, 2883-2898.

KHAN, F. M. (ed.) 1993. The Physics of radiation therapy, Philadelphia: Lippincott Williams &Wilkins.

LINDEBERG, J. W. 1922. Eine neue Herleitung des Exponentialgesetzes in der Wahrscheinlichkeitsrechnung. Math. Zeitschr, 15, 211–225.

LOW, D. A. & DEMPSEY, J. F. 2003. Evaluation of the gamma dose distribution comparison method. Medical Physics, 30, 2455-2464.

LOW, D. A., HARMS, W., MUTIC, S. & PURDY, J. 1998. A technique for the quantitative evaluation of dose distributions. Med. Phys., 25, 656.

MA, C. M. & ROGERS, D. W. O. 2009. BEAMDP Users Manual [Online]. Ottawa: NRC: NRCC Report PIRS-0509C. [Accessed].
MAINEGRA-HING, E. & KAWRAKOW, I. 2006. Efficient x-ray tube simulations. Medical Physics, 33, 2683-2690.
NELSON, W. R., HIRAYAMA, H. & ROGERS, D. W. O. 1985. The EGS4 Code System. SLAC-265,Stanford Linear Accelerator Center.
POLUDNIOWSKI, G., LANDRY, G., DEBLOIS, F., EVANS, P. M. & VERHAEGEN, F. 2009. SpekCalc: a program to calculate photon spectra from tungsten anode x-ray tubes. Phys Med Biol, 54, N433-8.
POLUDNIOWSKI, G. G. 2007. Calculation of x-ray spectra emerging from an x-ray tube. Part II. X-ray production and filtration in x-ray targets. Medical Physics, 34, 2175-2186.
ROGERS, D. W. O., FADDEGON, B. A., DING, G. X., MA, C.-M., WE, J. & MACKIE, T. R. 1995. BEAM: A Monte Carlo code to simulate radiotherapy treatment units. Medical Physics, 22, 503-524.
SALVAT, F., FERNANDEZ-VAREA, J.M., COSTA, E., AND SEMPAU,J. 2001. PENELOPE - A Code System for Monte Carlo Simulation of Electron and Photon Transport. Workshop Proceedings, Issy-les-Moulineaux, France, 92-64-18475-9.
SEMPAU, J., WILDERMAN, S. J. & BIELAJEW, A. F. 2000. DPM, a fast, accurate Monte Carlo code optimized for photon and electron radiotherapy treatment planning dose calculations. Physics in Medicine and Biology, 45, 2263.
VERHAEGEN, F., NAHUM, A. E., VAN DE PUTTE, S. & NAMITO, Y. 1999. Monte Carlo modelling of radiotherapy kV x-ray units. Phys Med Biol, 44, 1767-89.
WALTERS, B. R. B., KAWRAKOW, I. & ROGERS, D. W. O. 2002. History by history statistical estimators in the [small-caps BEAM] code system. Medical Physics, 29, 2745-2752.

BIELAJEW, A. F. (ed.) 2006. *The Monte Carlo Simulation of Radiation Transport. In: Integrating New Technologies into the Clinic: Monte Carlo and Image-Guided Radiation Therapy.*: Madison: Medical Physics Publishing; 1-20.
BRIESMEISTER, J. 2000. MCNP – A general monte carlo n-particle transport code. Los Alamos: LA-13709-M.
BUTSON, M. J., YU, P. K. N., CHEUNG, T. & ALNAWAF, H. 2010. Energy response of the new EBT2 radiochromic film to x-ray radiation. *Radiation Measurements,* 45**,** 836-839.
CHOW, J. C. L. 2010. Depth dose dependence of the mouse bone using kilovoltage photon beams: A Monte Carlo study for small-animal irradiation. *Radiation Physics and Chemistry,* 79**,** 567-574.
CUNNINGHAM, J. R. 1984. Quality assurance in dosimetry and treatment planning. *International journal of radiation oncology, biology, physics,* 10**,** 105-109.
FELLER, W. 1967. *An Introduction to Probability Theory and Its Applications,* Newyork, wiley.
FRAASS, B., DOPPKE, K., HUNT, M., KUTCHER, G., STARKSCHALL, G., STERN, R. & VAN DYKE, J. 1998a. American Association of Physicists in Medicine

Radiation Therapy Committee Task Group 53: quality assurance for clinical radiotherapy treatment planning. *Med Phys,* 25**,** 1773-829.

FRAASS, B., DOPPKE, K., HUNT, M., KUTCHER, G., STARKSCHALL, G., STERN, R. & VAN DYKE, J. 1998b. American Association of Physicists in Medicine Radiation Therapy Committee Task Group 53: Quality assurance for clinical radiotherapy treatment planning. *Medical Physics,* 25**,** 1773-1829.

HUQ, M. S., SONG, H., ANDREO, P. & HOUSER, C. J. 2001. Reference dosimetry in clinical high-energy electron beams: Comparison of the AAPM TG-51 and AAPM TG-21 dosimetry protocols. *Medical Physics,* 28**,** 2077-2087.

JENKINS, T. M., NELSON, W. R. & RINDI, A. (eds.) 1988. *Monte Carlo Transport of elcectrons and Photons*

JOHNS, H. E. & CUNNINGHAM, J. R. (eds.) 1983. *The Physics of Radiology,* Springfield,IL .

KAWRAKOW, I., MAINEGRA-HING, E., ROGERS, D. W. O., TESSIER, F. & WALTERS, B. R. B. 2011. The EGSnrc Code System: Monte Carlo Simulation of Electron and Photon Transport. *NRCC Report PIRS-701*.

KAWRAKOW, I., ROGERS, D. W. O. & WALTERS, B. R. B. 2004. Large efficiency improvements in BEAMnrc using directional bremsstrahlung splitting. *Medical Physics,* 31**,** 2883-2898.

KHAN, F. M. (ed.) 1993. *The Physics of radiation therapy,* Philadelphia: Lippincott Williams &Wilkins.

LINDEBERG, J. W. 1922. Eine neue Herleitung des Exponentialgesetzes in der Wahrscheinlichkeitsrechnung. *Math. Zeitschr,* 15**,** 211–225.

LOW, D. A. & DEMPSEY, J. F. 2003. Evaluation of the gamma dose distribution comparison method. *Medical Physics,* 30**,** 2455-2464.

LOW, D. A., HARMS, W., MUTIC, S. & PURDY, J. 1998. A technique for the quantitative evaluation of dose distributions. *Med. Phys.,* 25**,** 656.

MA, C. M. & ROGERS, D. W. O. 2009. *BEAMDP Users Manual* [Online]. Ottawa: NRC: NRCC Report PIRS-0509C. [Accessed].

MAINEGRA-HING, E. & KAWRAKOW, I. 2006. Efficient x-ray tube simulations. *Medical Physics,* 33**,** 2683-2690.

NELSON, W. R., HIRAYAMA, H. & ROGERS, D. W. O. 1985. The EGS4 Code System. *SLAC-265,Stanford Linear Accelerator Center*.

POLUDNIOWSKI, G., LANDRY, G., DEBLOIS, F., EVANS, P. M. & VERHAEGEN, F. 2009. SpekCalc: a program to calculate photon spectra from tungsten anode x-ray tubes. *Phys Med Biol,* 54**,** N433-8.

POLUDNIOWSKI, G. G. 2007. Calculation of x-ray spectra emerging from an x-ray tube. Part II. X-ray production and filtration in x-ray targets. *Medical Physics,* 34**,** 2175-2186.

ROGERS, D. W. O., FADDEGON, B. A., DING, G. X., MA, C.-M., WE, J. & MACKIE, T. R. 1995. BEAM: A Monte Carlo code to simulate radiotherapy treatment units. *Medical Physics,* 22**,** 503-524.

SALVAT, F., FERNANDEZ-VAREA, J.M., COSTA, E., AND SEMPAU,J. 2001. PENELOPE - A Code System for Monte Carlo Simulation of Electron and Photon Transport. *Workshop Proceedings, Issy-les-Moulineaux, France***,** 92-64-18475-9.

SEMPAU, J., WILDERMAN, S. J. & BIELAJEW, A. F. 2000. DPM, a fast, accurate Monte Carlo code optimized for photon and electron radiotherapy treatment planning dose calculations. *Physics in Medicine and Biology,* 45**,** 2263.

VERHAEGEN, F., NAHUM, A. E., VAN DE PUTTE, S. & NAMITO, Y. 1999. Monte Carlo modelling of radiotherapy kV x-ray units. *Phys Med Biol,* 44**,** 1767-89.

WALTERS, B. R. B., KAWRAKOW, I. & ROGERS, D. W. O. 2002. History by history statistical estimators in the [small-caps BEAM] code system. *Medical Physics,* 29**,** 2745-2752.

CHAPTER FOUR

Development of a Monte Carlo treatment planning system

Particle transport in Monte Carlo (MC) simulations is governed by interaction probabilities determined by particle energy, material composition and density. Material composition and density can be determined from computed tomography (CT) data using a CT number to material density calibration curve. This chapter describes challenges and approximations involved with animal modeling using cone beam CT (CBCT) data as input for MC based treatment planning system. A calibration curve is developed to convert CBCT images obtained on the XRAD unit to material and density information for input for MC calculations. The Monte Carlo CBCT model is subsequently benchmarked against measurement in a homogenous medium.

4.1Conversion of CT data into material data

As the existing tools developed in EGSnrc are not suitable for incorporating CBCT data as input for MC simulations, a series of scripts was written in MATLAB. Figure 4.1 depicts the flow chart of this process.

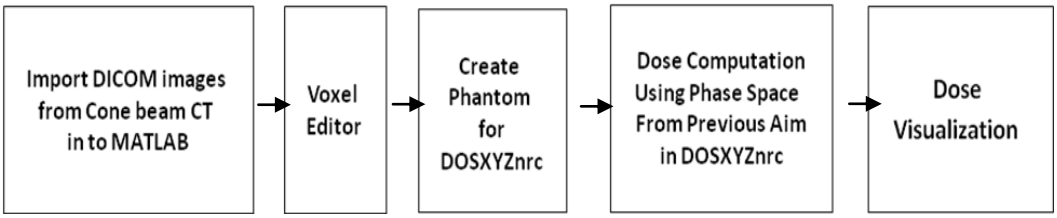

Figure 4.1: Flow chart for MC simulation for dose computation using image data from XRAD 225Cx irradiator.

The first step is to import DICOM CBCT images into MATLAB. The crucial parameters such as dataset geometry, voxel dimensions, field of view, and parameters defining the materials were determined from the XRAD 225Cx CBCT images. The acquired CBCT images were imported into MATLAB and then sub-sampled for planning.

4.1.1 Sub sampling of CBCT images

The inherent resolution of the XRAD 225Cx CBCT images is 0.1x0.1 mm^3 as shown in Figure 4.2a. High resolution was desirable for small animal representation, however, this causes to increases number of particle histories required to achieve low dose uncertainty. To reduce simulation time, bilinear interpolation method was used in MATLAB to down sample the image resolution. The level of sub-sampling was selected based on CBCT matrix variation relative to the original data set. Figures 4.2 b, c,d show images subsampled to various matrix sizes. Over sampling of the images causes a loss of material identification and dose accuracy in MC simulations (Figure 4.2d). The sub-sampled phantom files were converted from CBCT units to a material / density matrix for input to DOSXYZnrc.

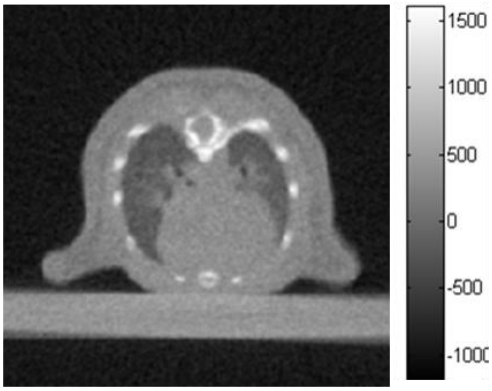

Figure 4.2a: 284x667 matrix (no sub sampling)

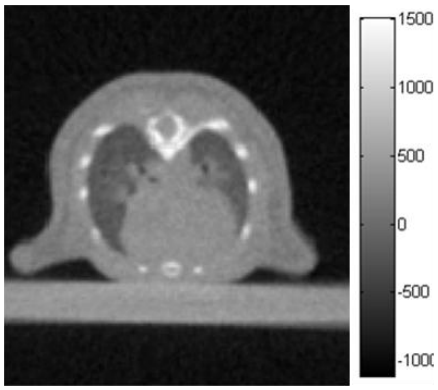

Figure 4.2b: 142x334 matrix (sub sampled using a factor of 2)

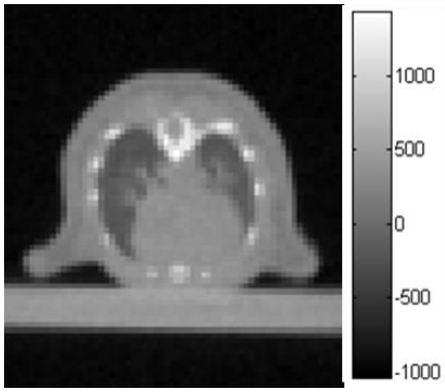

Figure 4.2c: 71x166 matrix (sub sampled using a factor of 4)

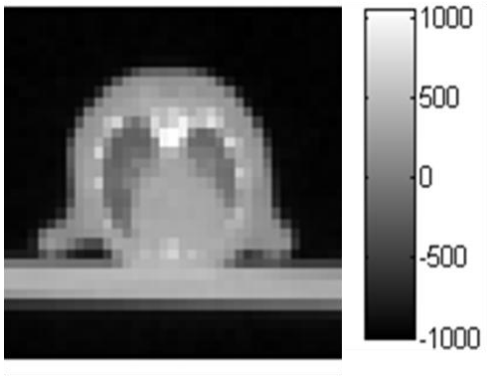

Figure 4.2d: 35x84 matrix (sub sampled using a factor of 8)

4.1.2 CBCT calibration curve

Homogenous phantom plugs (Gammex RMI 467, Middleton, WI) of known material and physical density were scanned using the XRAD 225Cx cone beam CT system. The scans were performed at 80 kVp. The DICOM images for each phantom plug were imported into MATLAB for analysis. A MATLAB script was written to select an area of interest (1x1cm^2) inside each phantom plug and to calculate the mean and

standard deviation of the corresponding CBCT units. The results are given in Table 4.1 for 80 kVp. Next, a lookup table for mapping the CBCT units to a corresponding material density unit was created. The resultant CBCT calibration is shown in Figure 4.3 with the line indicating an 8^{th} degree polynomial fit.

CBCT units (Mean)	Standard deviation	Material	Density [g/cm^3]
-963	5	air	0.001205
-596	218	lung 300	0.30
-372	177	lung 450	0.45
78	55	adipose	0.92
180	59	breast	0.98
292	64	water	1.00
416	68	muscle	1.05
864	74	inner bone	1.13
893	75	bone 200	1.15
1297	83	bone 484	1.34
2027	116	bone 480	1.52
2683	139	bone 450	1.82

Table 4.1**:** CBCT units of phantom plugs (Gammex 467) with known material composition and density at 80 kVp used for tissue characterization

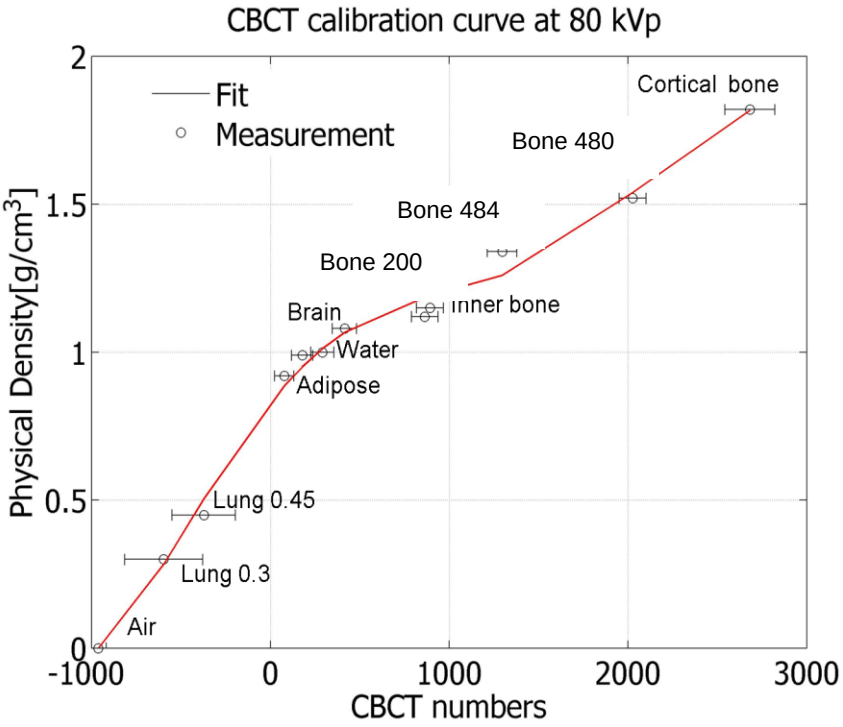

Figure 4.3: The conversion of CBCT units to material density.

4.1.3 Material assignment

MC simulations require cross section data for each material defined in EGSnrc. DOSXYZnrc provides some default material datasets with cross section data for dose calculations (Walters et al., 1996). Originally, these material data sets were created for a wide energy range and may be inaccurate in low energy region because of interpolation of the existing data (Walter and Hideo, 1995). For this project, several new material datasets were added to the existing PEGS4 library. This was be done by providing atomic composition of materials and/or modifying the existing compounds to make a unique library appropriate for orthovoltage energies. The material composition of the phantom plugs (Gammex RMI 467, Middleton, WI) were obtained from the manufacturer. The

known physical densities and atomic composition of human tissue were obtained from standard sources (DeMarco, 1997, DeMarco et al., 1998, ICRP, 1975, ICRU., 1989, Speiser, 2010) to create a material data set library. This was facilitated using the EGSnrc preprocessor program (Walters et al., 1996). This tool provides the cross section data for each medium. The human tissue material data sets given in Table 4.2 were concatenated into a library with the same cut off energies. The library was then used to assign the corresponding material based on their respective CBCT units. The material assignment calibration curve is shown in Figure 4.4. The flow chart for this procedure is shown in Figure 4.5. The phantom plugs (Gammex RMI 467, Middleton, WI) atomic compositions are not provided here due to manufacturer's confidentiality.

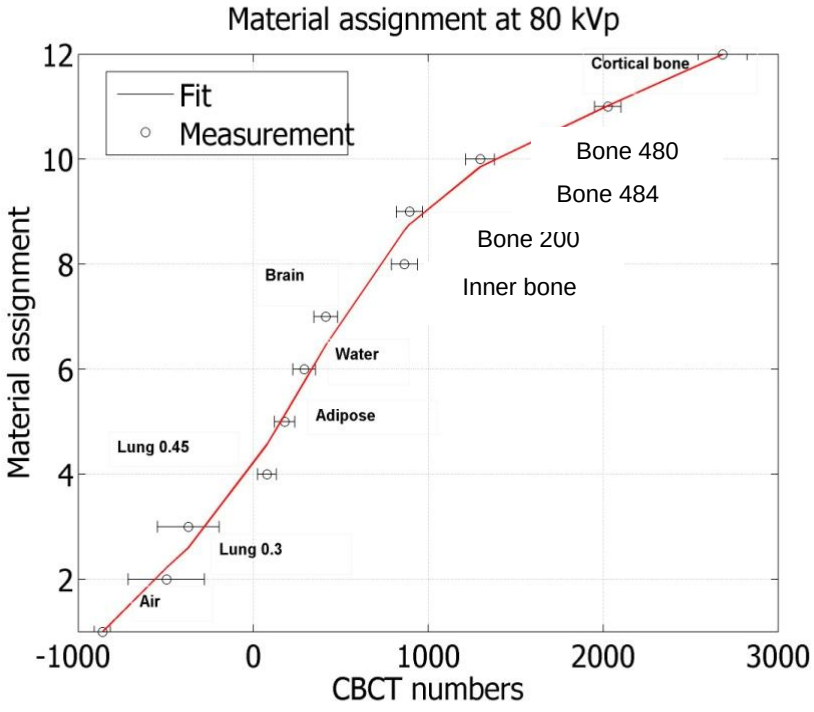

Figure 4. 4: CBCT unit to material conversion.

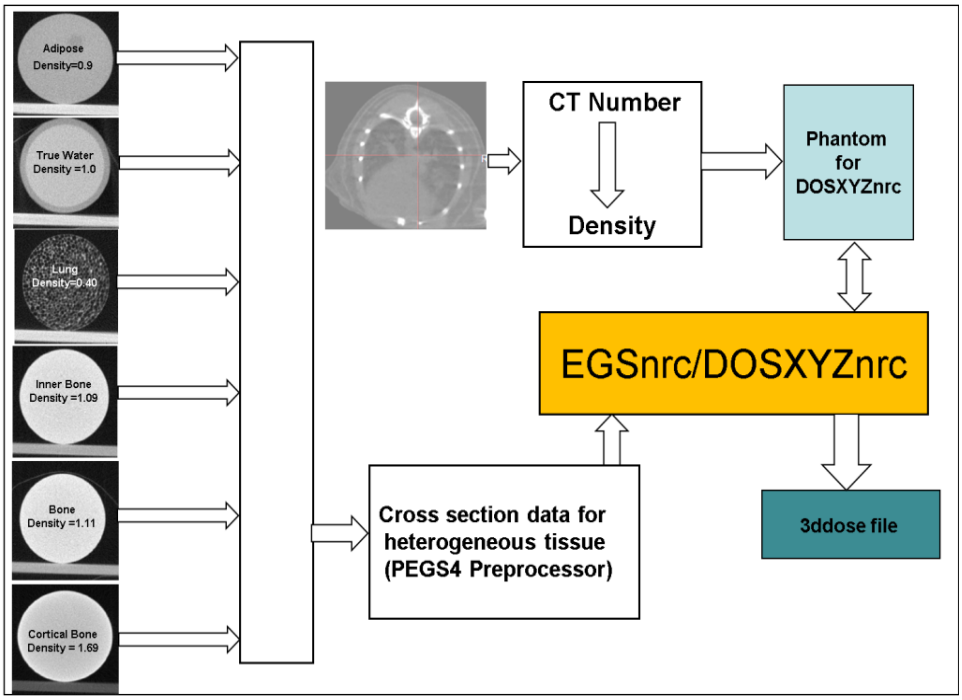

Figure 4.5: Creating cross section data of heterogeneous media for EGSnrc MC code using PEGS4 program. CBCT data are converted to density and used as phantom input in DOSXYZnrc for dose calculation.

CBCT units range upper	lower	Material	Elemental composition	Density[g/cm^3]
-1012	-862	Air	75.5%N, 23.2%O, 1.3%Ar	0.001205
-863	-496	Lung	10. 4%C, 10.3%H, 2.9%N, 76.4%O	0.30
-496	-371			0.45
-372	78	Fat	63.7%C, 11.9%H, 23.2%O, 0.8%N	0.92
79	180	Brain	2:1 H: O	0.98
181	292	Water		1.00
293	415	Muscle	10.8%C, 10.1%H, 2.8%N, 76.3%O	1.08
416	864	Bone	14.3%C, 20.8%Ca, 4.68%H, 4.16%C, 44.4%O, 10.6%Si	1.12
893	865			1.15
1297	894			1.34
2027	1298			1.52
2683	2028			1.82

Table 4.2: Lookup table used to convert CBCT units to specific tissue material and density.

Monte Carlo simulations were performed in the resulting 3D phantom and the results were recorded in files labeled 3D dose. This output file was typically normalized to a maximum dose at the isocenter or alternatively surface dose point for single beam on a 3D phantom image using the DOSXYZ_show editor for dose visualization. Dose computation results from MC simulation in DOSXYZ give 3D dose deposition information in terms of total dose per incident particle for each voxel with respective density voxel in the 3D phantom density file. The result of 3D dose distribution was normalized to dose at the isocenter for multiple beams or maximum dose point for single beam. The output dose distributions can be visualized using DOSXYZ_Show editor (Walter and Hideo, 1995).

4.2 Validation of the Monte Carlo source model in a CBCT based medium

A solid water phantom (4x4x4 cm^3) was scanned at 80 kVp and 0.3 mAs in CBCT mode. DICOM images were imported into MATLAB and processed to create a 3D phantom to be used for MC dose computation. The phantom resolution was sub-sampled from 0.1x0.1x0.1 mm^3 to 0.2x0.2x0.8 mm^3 in MATLAB. Computation was performed using a 10 mm diameter circular field phase space file in the DOSXYZnrc package, with an SSD of 30.5 cm and virtual source to surface distance of 7.0 cm.; the input file is given in Appendix B. An uncertainty of less than 1% was achieved using $1.5x10^9$ histories. Figure 4.6 shows the calculated 3D dose distribution of this simulation while Figure 4.7 shows the MC calculated PDD. Air gap artifacts in the CBCT images produce irregularities in the PDD.

Calculated and measured planar distributions were compared at a depth of 1 cm. The output 3D dose file from DOSXYZnrc was imported into MATLAB for data analysis. A 2D matrix containing the calculated dose at 1 cm depth was extracted from the "3D dose file". Next, an image file (TIF) was created representing a reference planar dose as input for Film QA analysis. The measured planar dose distributions were obtained by exposing EBT2 films at depth of 1 cm in a solid water medium (4x4x4 cm^3) for 1.5 minutes at 225 kVp, 13 mAs irradiator settings. The film was scanned using the EPSON 1000XL scanner and saved in TIF format.

The scanned image was imported into Film QA software and converted to dose using a kV calibration curve. The 90%, 80%, 50% and 20% isodose lines for measurements and simulations are shown in Figure 4.8. Following the TG-53 protocol, the profiles were normalized to the point of maximum dose.

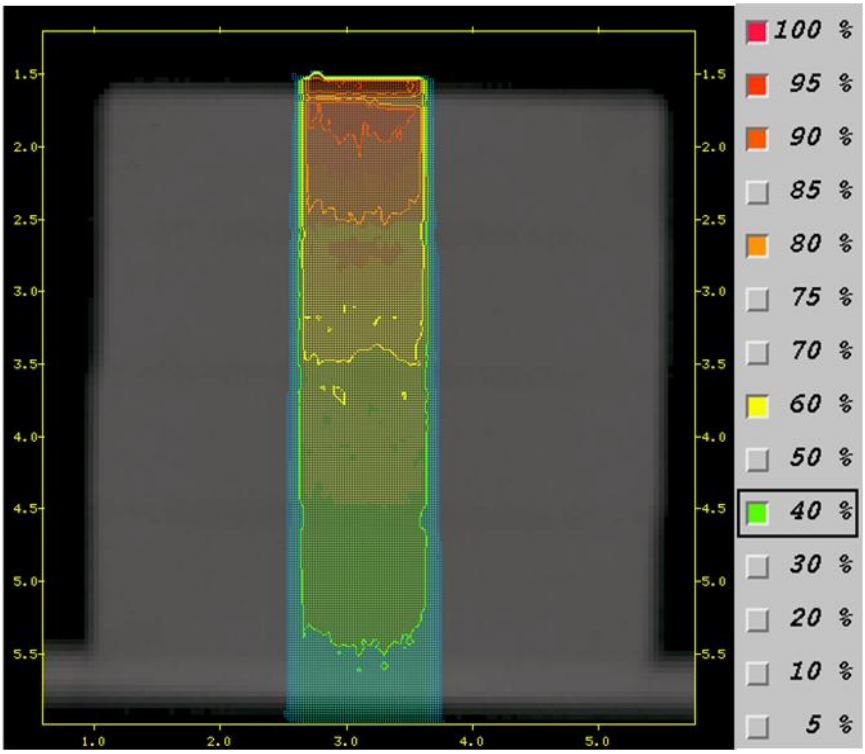

Figure 4.6: DOSXYZ CBCT homogenous solid water (4x4x4cm^3). Each dose point in 3D phantom is normalized to dose at the surface. Dose uncertainty for each point in simulation is 0.5 to 3.0 % with maximum uncertainty toward distal end of the phantom.

Dose profiles along two major planes horizontal and vertical plane are shown in Figures 4.9 and 4.10 for a 10 mm diameter field. Agreement within 1% was found for both the outer and inner beam regions. The gamma map shown in Figure 4.11 shows excellent agreement with measurements in the within selected region of interest where 98.69% of the calculated data met the gamma criteria of 3%/0.5 mm.

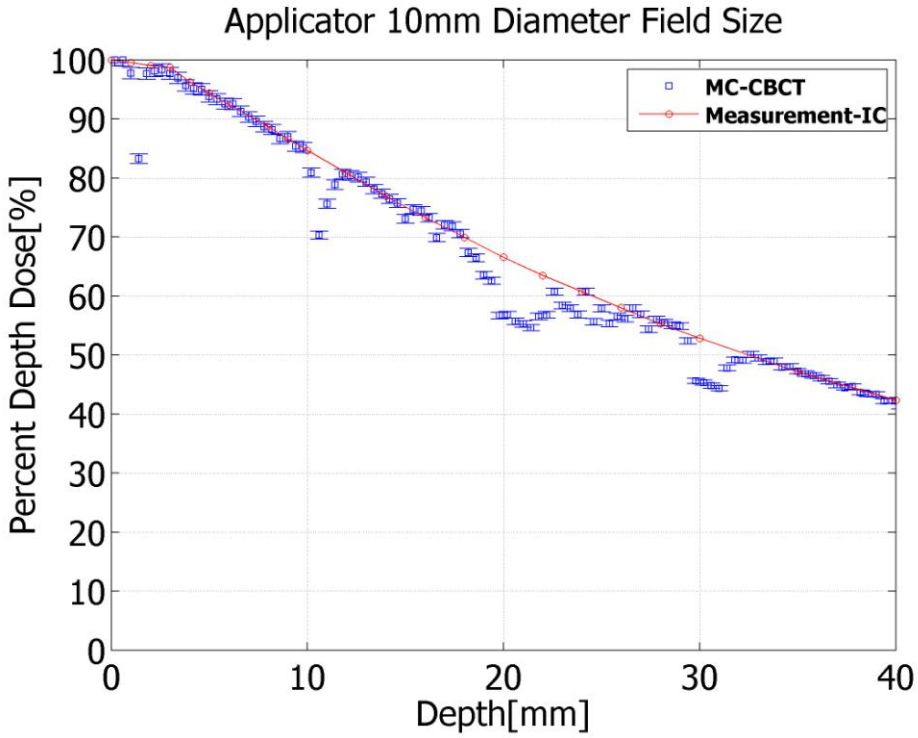

Figure 4.7: Monte Carlo calculated PDD curve in CBCT data and ionization chamber measurement curves in water phantom at 225 kVp for a 10 mm diameter circular field.

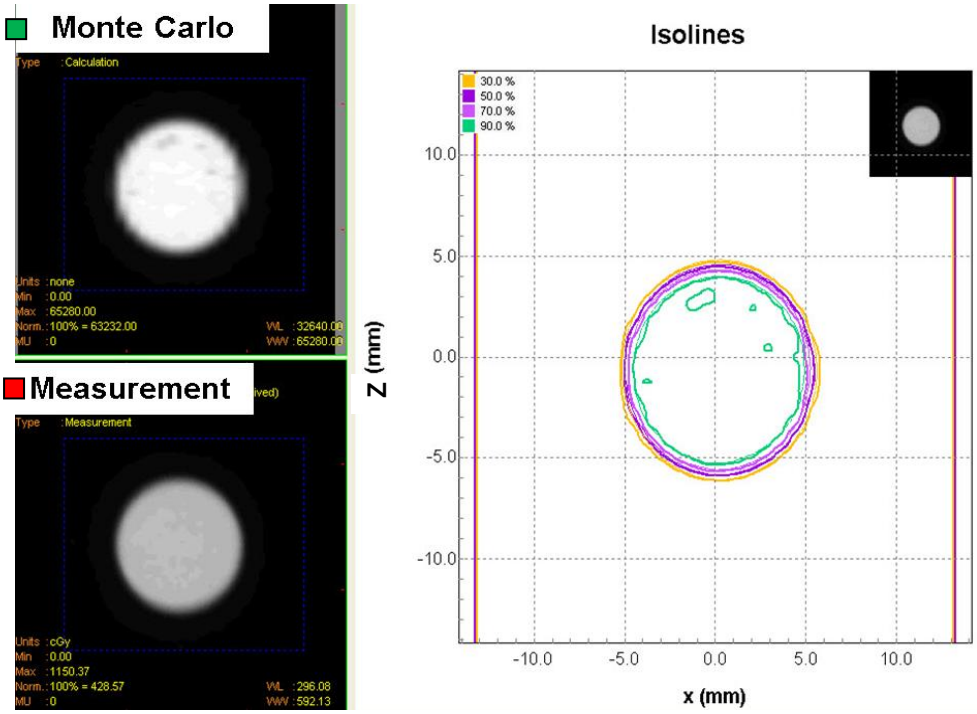

Figure 4.8**:** Calculated and measured isodose lines for a 10 mm diameter circular field at 1 cm depth. Thin isodose lines correspond to measurement and thick lines to Monte Carlo.

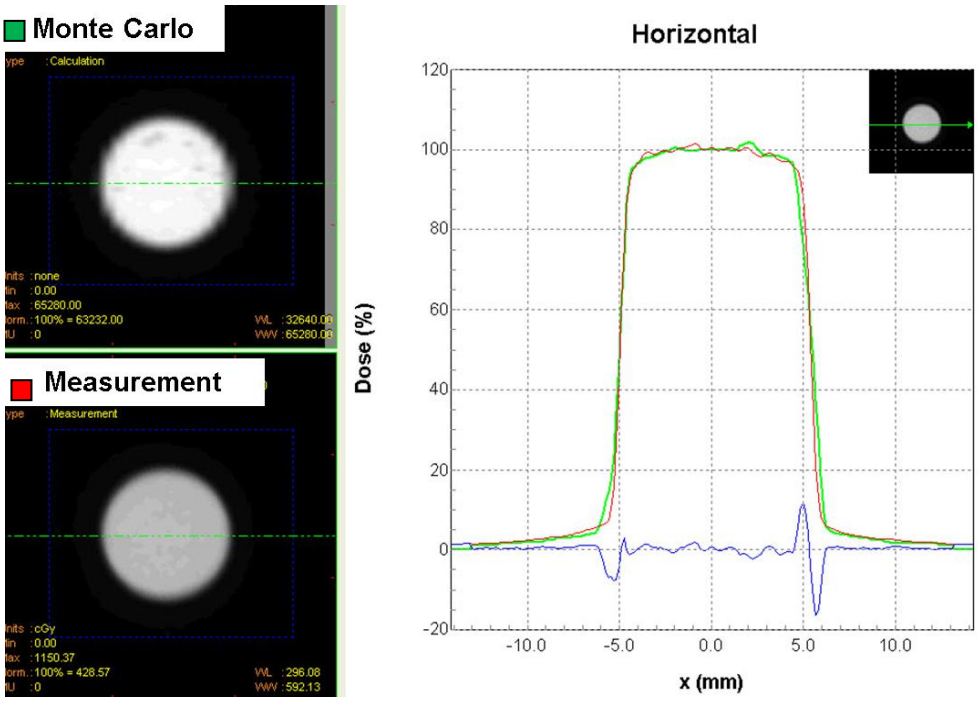

Figure 4.9**:** Calculated and measured horizontal dose profile for a 10 mm diameter circular field at 1 cm depth.

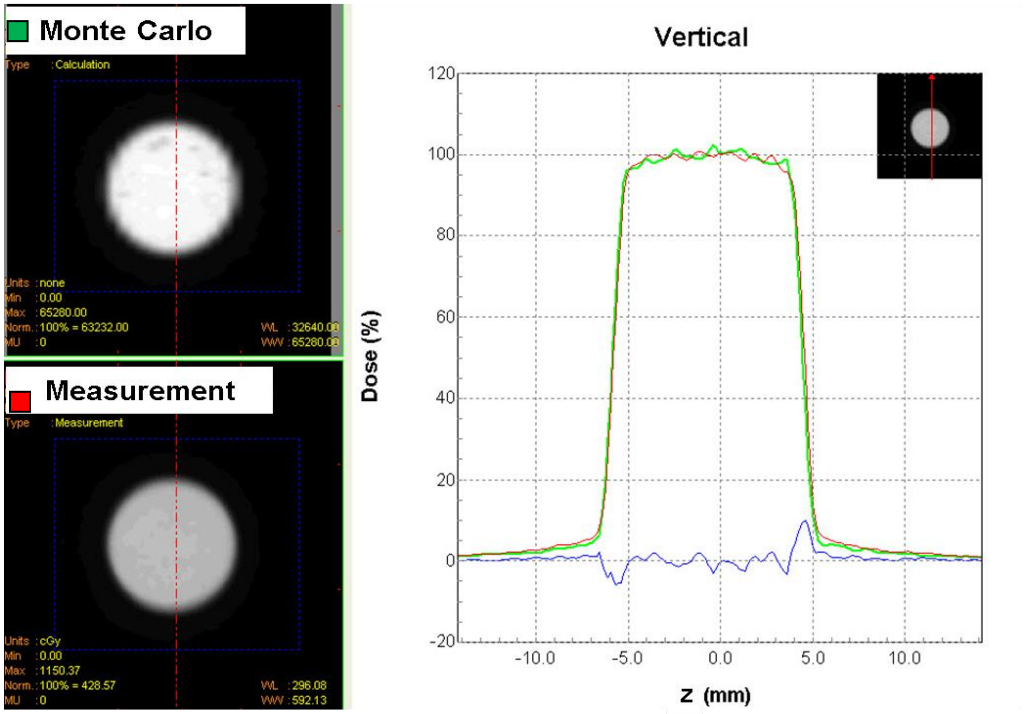

Figure 4.10**:** Calculated and measured vertical dose profile for a 10 mm diameter circular field at 1 cm depth.

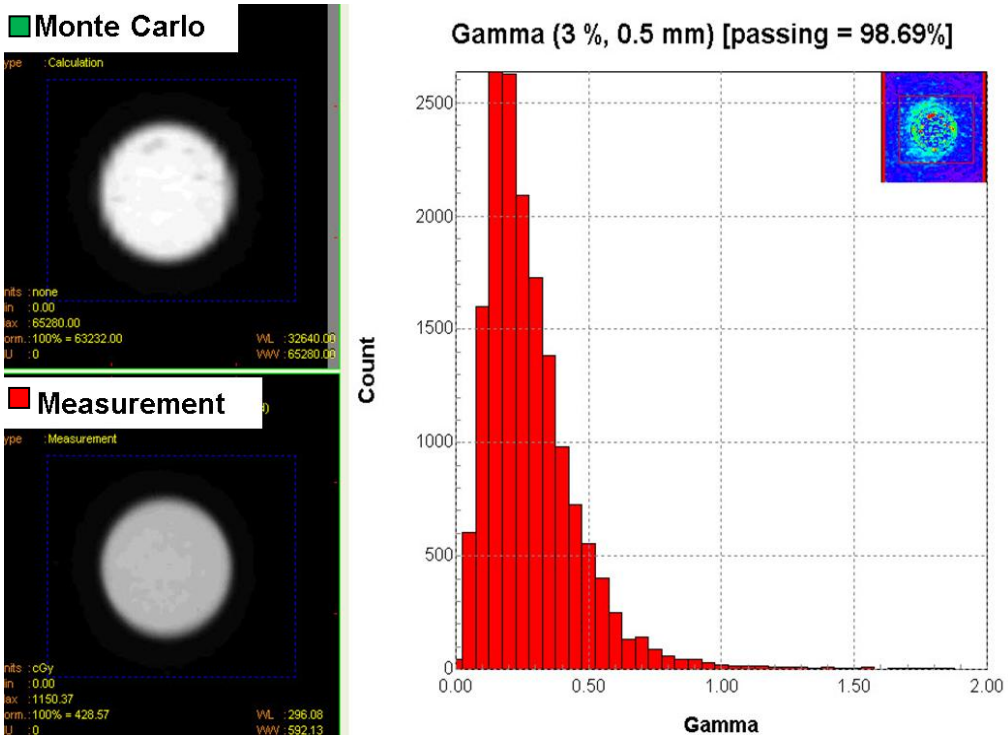

Figure 4.11: Anterior to posterior beam delivery single irradiation. Gamma map for 3%/0.5 mm criteria has 98.69 % passing rate.

4.3 Demonstration of Monte Carlo source model in a small animal CBCT Model

To demonstrate MC planning capabilities in a small animal model, a mouse was scanned with cone beam CT at 80 kVp, 0.3 mAs in XRAD 225Cx. The lung region was specifically chosen for scanning because of its heterogeneous nature. After the images were acquired, they were processed in MATLAB to create the 3D phantom for DOSXYZnrc as described in section 4.1.3. The DICOM images acquired from the XRAD 225Cx were converted to physical density and material assignment image as shown in Figure 4.12. The original phantom resolution of 0.1x0.1x0.1 mm^3 was reduced to 0.2x0.2x1.0 mm^3 in MATLAB. The corresponding density image on the central axis of the radiation beam is shown in Figure 4.13. Dose calculation was performed in DOSXYZnrc using a 10 mm diameter field phase space file. The dose was normalized to the maximum dose in the simulation result (the maximum dose occurs in bone). The isodose distribution on the central axis of the radiation beam is shown Figure 4.14.

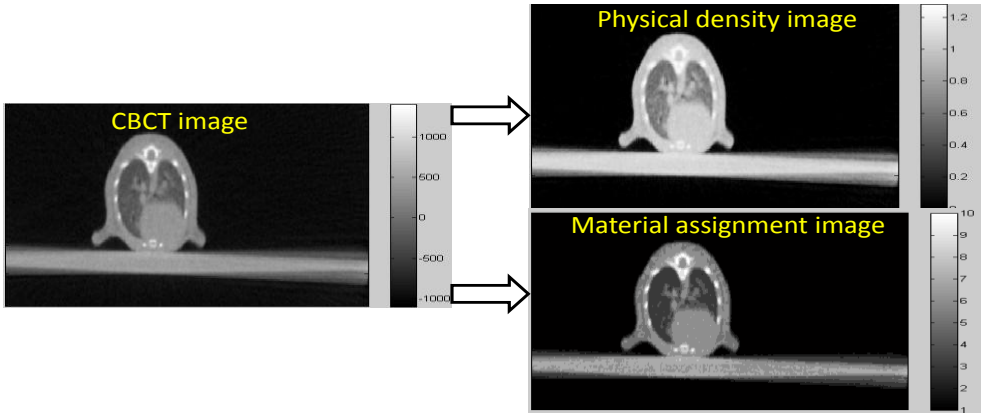

Figure 4.12: CBCT image conversion to physical density and material image

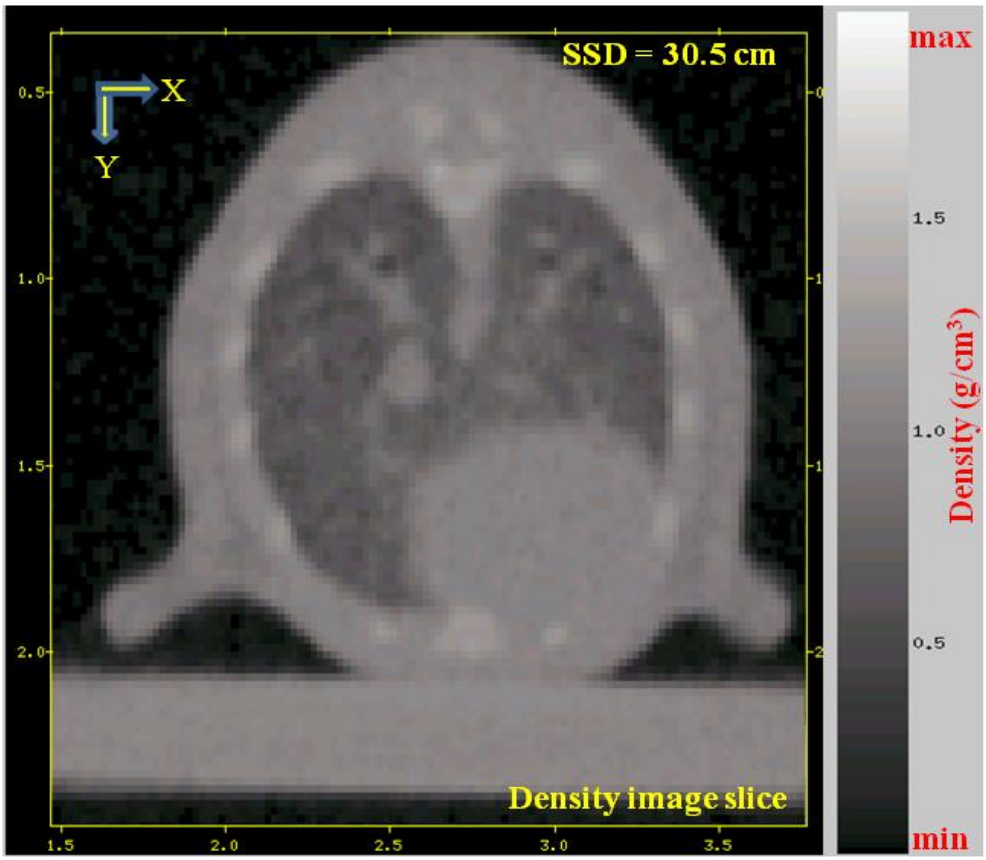

Figure 4.13: Mouse density image from dosxyz_show.

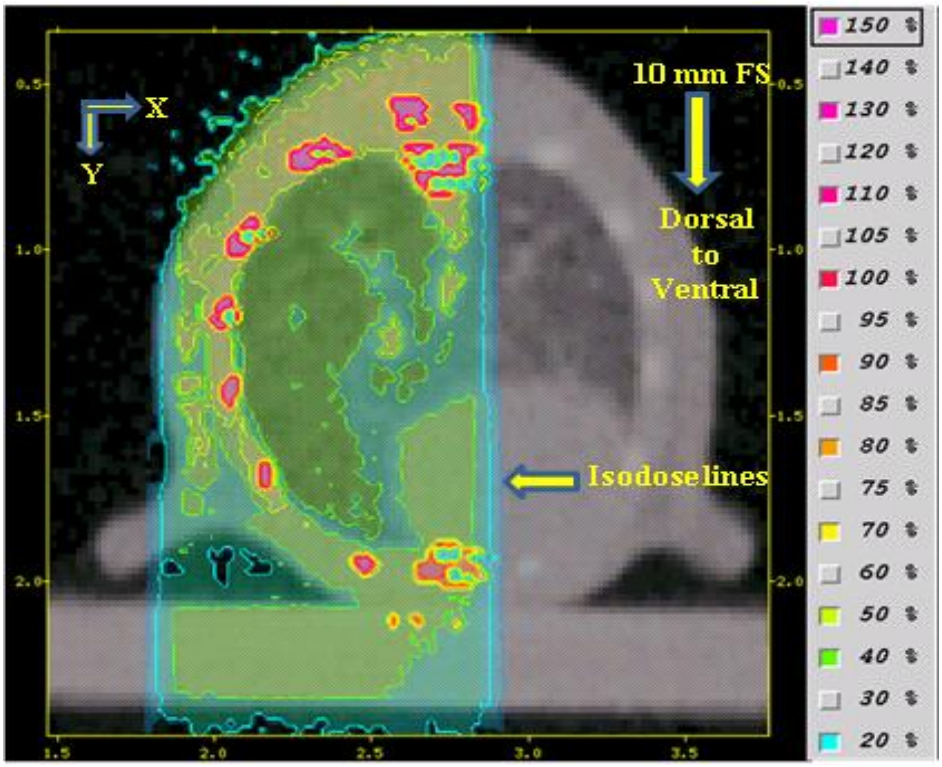

Figure 4.14: Central axis isodose lines of 10 mm diameter circular field size. Isodose lines are normalized to D_{max} (bone).

As shown in Figure 4.14 bone dose is greater compared to tissues such as muscle and adipose tissue. In lung tissue, dose is greater than in compared to air. Dose distributions demonstrate the necessity of a treatment planning system based on Monte Carlo for improved accuracy in small animals compared to present hand calculations reported in literature for the kV energy range.

4.4 Irradiation time calculation for Monte Carlo treatment planning

In this work, we propose formalism for time calculation in Monte Carlo treatment planning for the small animal irradiator. This formalism determines the time required to deliver a specified dose based on a Monte Carlo-calculated dose distribution. The detailed description and formula are given for various situations such as single and multiple beams for 3D conformal radiotherapy. The absolute dose rate $\overset{*}{D}_{\underset{ref}{M}}$ measured for a reference collimator under calibration conditions (central axis, depth of dose maximum, 40x40 mm^2 field defined at 30.5 cm source to surface distance) is 3.420 (Gy/min). Then the time (t) required to deliver a specified dose of radiation D_{P_d} at a depth d in a phantom is given by:

$$t(\min) = \frac{D_{P_d}}{\overset{\bullet}{D}_{\underset{ref}{M}}} \tag{4.1}$$

Similarly, the time required to deliver a specified dose of radiation D_{P_d} for any other field size is given by

$$t(\min) = \frac{D_{P_d}}{\overset{\bullet}{D}_{\underset{ref}{M}} * OF} \tag{4.2}$$

Where OF is the total scatter factor for that field size. The absolute dose rate for any field size (AF) is given by

$$\overset{\bullet}{D}_{\underset{AF.ref}{M}} = OF \bullet \overset{\bullet}{D}_{\underset{ref}{M}} \tag{4.3}$$

In this work, independent phase space files are created for each field size from Monte Carlo simulations. Using these phase space files, simulations under the reference condition were performed and the total dose per incident particle was determined on the central axis at depth of maximum ($D_{\underset{AF.ref_{\max}}{MC}}$) for each field size. These are given in Table 4.4. The relation between measurement and simulation is given by:

$$\dot{D}_{\underset{AF.ref}{M}} = k \bullet D_{\underset{AF.ref}{MC}} \tag{4.4}$$

Where k is a constant and it can be defined as number of incident particles (IP) per minute. For each field size, k values are calculated based on the MC calculated total dose per incident particle at D_{max} at an SSD of 30.5 cm using equation 4.4

Field size at isocenter	MC calculated total dose per incident particle at D_{max} at an SSD of 30.5 cm
1.0 mm	$5.067*10^{-19}$
2.5 mm	$6.145*10^{-19}$
3.5 mm	$6.432*10^{-19}$
5.0 mm	$6.360*10^{-19}$
10.0 mm	$6.624*10^{-19}$
15.0 mm	$6.541*10^{-19}$
20 .0 mm	$6.691*10^{-19}$
10x10 mm^2	$6.545*10^{-19}$
15x15 mm^2	$6.672*10^{-19}$
20x20 mm^2	$6.854*10^{-19}$
40x40 mm^2	$7.201*10^{-19}$

Table 4.4: MC simulated total dose per incident particle values for each field size with respective phase space file at a depth of D_{max} and SSD of 30.5 cm.

We define k as the ratio of the absolute dose rate from measurement $\dot{D}_{\underset{AF.ref}{M}}(Gy/\min)$ for each field to the reference condition for that same size field in Monte Carlo ($D_{\underset{AF.ref}{MC}}(\frac{Gy}{IP})$) and it is given by

$$k(\frac{IP}{\min}) = \frac{\dot{D}_{\underset{AF.ref}{M}}}{D_{\underset{AF.ref}{MC}}} \tag{4.5}$$

The absolute dose rate from Monte Carlo simulation at any SSD and depth in a MC distribution is calculated by

$$\dot{D}_d = k(\frac{IP}{\min}) * D_{MC_d}(\frac{Gy}{IP}) \tag{4.6}$$

The total time to deliver the prescription dose to a prescribed point is given by

$$t(\min) = \frac{D_{p_d}}{\dot{D}_d} \tag{4.7}$$

For weighted beams, then the total time to deliver the prescription dose to any point by each beam with weight is given by

$$t(\min) = \frac{W * D_{p_d}}{D_d} \tag{4.8}$$

4.4.1 Single beam

An example is demonstrated here using equation 4.7 to calculate the time to deliver a prescription of dose of 2 Gy to a point located at the isocenter of a 4x4x4 cm^3 phantom (x=2 cm ,y=,2 cm z=2 cm), with source to axis distance of 30.5 cm for 10 mm diameter circular field.

First, a MC simulation was performed using a 10 mm diameter circular field phase space file incident on a 4x4x4 cm^3 solid water phantom, with a source to axis distance of 30.5 cm and an isocenter located at x=2 cm ,y=,2 cm z=2 cm (Figure 4.15). The absolute dose rate from measurement for a 10 mm field at 30.5 cm SSD at d_{max} is calculated using equation 4.3 and it is given by.

$$\dot{D}_{\underset{10mm.ref}{M}} = OF \bullet \dot{D}_{\underset{ref}{M}} = 0.887 \bullet 3.420 \text{ (Gy/min)} = 3.0335 \text{(Gy/min)} \tag{4.9}$$

Using equation 4.5 the *k* value is calculated to relate measurement reference condition to Monte Carlo reference condition a 10 mm diameter applicator

$$k(\frac{IP}{\min}) = \frac{\dot{D}_{\underset{AF.ref}{M}}}{D_{\underset{AF.ref}{MC}}} = \frac{3.0335 \text{ (Gy/min)}}{6.624 * 10^{-19} \text{(Gy/IP)}} = 0.457 \ * 10^{19} \text{(IP/min)} \tag{4.10}$$

The MC simulated value at isocenter is D_{isoMC_d} $5.084*10^{-19}$ (Gy/IP) as shown in Figure 4.15.

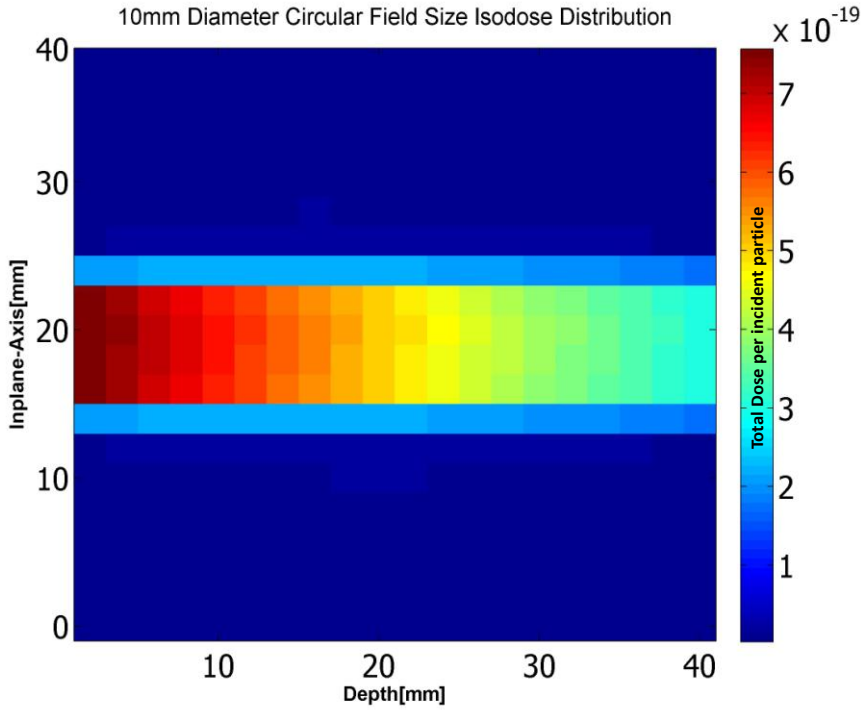

Figure 4.15: Isodose distributions for 10 mm diameter circular field in a homogenous medium of solid water ($4x4x4cm^3$) at a SAD of 30.5 cm and the isocenter for the phantom x= 2 cm ,y=2 cm and z=2 cm.

The absolute dose rate at the isocenter is calculated from the dose distribution using equation 4.6.

$$\dot{D}_d = k(\frac{IP}{\min}) * D_{MC_d}(\frac{Gy}{IP}) = 0.457 \ *10^{19} * 5.084 * 10^{-19} = 2.328(\text{Gy/min}) \quad (4.11)$$

Once the dose rate at isocenter is determined, the time required to deliver the prescribed dose can be calculated using equation 4.8

$$t(\min) = \frac{D_{p_d}}{\dot{D}_d} = \frac{2(\text{Gy})}{2.328(\text{Gy/min})} = 0.859\min \quad (4.12)$$

The MC simulated result yields a time of $0.859\,\text{min}$ (51.5 sec) to deliver a prescribed dose (2 Gy) to the isocenter. For comparison, the time to deliver 2 Gy calculated using the measured dosimetric parameters (Chapter 2) is given by Equation 4.9.

$$t(\text{min}) = \frac{D_{p_d * 100}}{\dot{D}_{\substack{M \\ ref}} * OF * (PDD) * \left(\frac{SCD}{SSD}\right)^2} \tag{4.13}$$

For reference conditions defined at a source to calibration distance=30.5 cm, the PDD value at 2 cm depth=66.56, the scatter factor (OF) =0.887 and the absolute dose rate=3.420 Gy/min. The phantom is located source to surface distance of 28.5 cm.

$$t(\text{min}) = \frac{2 * 100}{3.420 * 0.887 * 66.56 * \left(\frac{30.5}{28.5}\right)^2} = 0.864\,\text{min} \tag{4.14}$$

There is an excellent agreement between the Monte Carlo and measurement.

4.4.2 Multiple beam

In a second example, a dose of 1 Gy is prescribed to a point at the isocenter using three 10 mm beams with weights of 0.5 for beam 1 and 0.25 for beams 2 and 3. A 4x4x4 cm^3 solid water phantom is simulated with the phantom centered on the isocenter. First, the MC Isodose distribution for the three beams configuration was calculated (Figure 4.16). The absolute dose rate for the 10 mm field at 30.5 cm SSD at d_{max} is calculated using equation 4.3 and is given by.

$$\dot{D}_{\substack{M \\ 10mm.ref}} = OF \bullet \dot{D}_{\substack{M \\ ref}} = 0.887 \bullet 3.420\ (\text{Gy/min}) = 3.0335(\text{Gy/min}) \tag{4.15}$$

Using equation 4.5, the *k* value calculated to relate measurements under the reference condition to Monte Carlo the same condition for a 10 mm applicator is:

$$k(\frac{IP}{\min}) = \frac{\dot{D}_{\substack{M \\ AF.ref}}}{D_{\substack{MC \\ AF.ref}}} = \frac{3.0335\ (\text{Gy/min})}{6.624*10^{-19}(\text{Gy/IP})} = 0.457\ *10^{19}(\text{IP/min}) \tag{4.16}$$

The MC simulated value at isocenter is $5.042*10^{-19}$ (Gy/IP) (D_{isoMC_d}) (Figure 4.16).

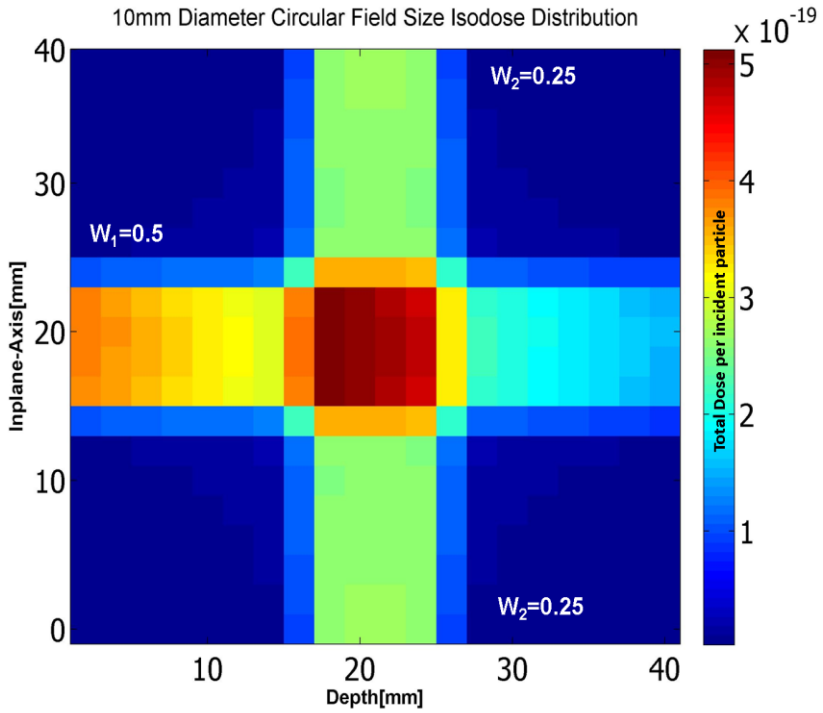

Figure 4.16: Isodose distributions for 10 mm diameter circular field in homogenous medium of solid water ($4x4x4cm^3$) with multiple beams.

The calculated MC dose rate at isocenter from multiple beams from equation 4.6 is:

$$\dot{D}_d = k(\frac{IP}{\min})*D_{MC_d}(\frac{Gy}{IP}) = 0.457\ *10^{19}(\frac{IP}{\min})*5.042*10^{-19}(\frac{Gy}{IP}) = 2.304(\text{Gy/min}) \tag{4.17}$$

Once the dose rate at isocenter determined, the time to deliver the prescribed dose is calculated from equation 4.7:

$$t(\min) = \frac{WD_{p_d}}{\dot{D}_d} = \frac{1*1(\text{Gy})}{2.304(\text{Gy/min})} = 0.433\min \tag{4.18}$$

Where W=1 is the total weight of all three beams MC simulated result yields a time of 0.433 min (26 sec) to deliver a prescribed dose (1 Gy) to the isocenter. The individual beam time is given by multiplying the weight of each beam: 13 seconds for beam 1 and 6.5 seconds each for and beams 2 and 3.

For comparison, the time to deliver 1 Gy calculated using the measured dosimetric parameters (Chapter 2) is:

$$t(\min) = \frac{W * D_{p_d * 100}}{\dot{D}_{M}_{ref} * OF * (PDD) * \left(\frac{SCD}{SSD}\right)^2} \tag{4.19}$$

Where W=1 is the total weight of three beams Reference conditions defined are source to calibration distance=30.5 cm, PDD value at 2 cm depth=66.56, total scatter factor (OF) =0.887 and absolute dose rate=3.420 Gy/min. The phantom is located source to surface distance of 28.5 cm.

$$t(\min) = \frac{1*1*100}{3.420*0.887*66.56*\left(\frac{30.5}{28.5}\right)^2} = 0.432\min \tag{4.20}$$

The measured result yield 0.432 min (25.92 sec) to deliver 1 Gy prescribed dose at isocenter. The individual beam time is given by multiplying the weight of each beam: 13 seconds for beam 1 and 6.5 seconds each for and beams 2 and 3**.**

4.5 Absolute dose comparison between MCTPS and measurement

A heterogeneous water phantom with solid water and lung (4x4x4 cm^3) was scanned at 80 kVp and 0.3 mAs in CBCT mode. DICOM images were imported into MATLAB and processed to create a 3D phantom to be used for MC dose computation. The phantom resolution was sub-sampled from 0.1x0.1x0.1 mm^3 to 0.8x0.8x0.8 mm^3 in MATLAB. Computation was performed using a 10 mm diameter circular field phase space file in the DOSXYZnrc package, with an SSD of 30.5 cm and virtual source to surface distance of 7.0 cm.; the input file is given in Appendix B. An uncertainty of less than 2 .5% was achieved using $1.9x10^9$ histories. Figure 4.x shows the calculated 3D dose distribution of this simulation. The MC simulated value at isocenter is $5.49*10^{-19}$ (Gy/IP) (D_{isoMC_d}) (Figure 4.16).

Calculated and measured absolute dose comparison was compared at a depth of 2 cm. The output 3D dose file from DOSXYZnrc was imported into MATLAB for data analysis. A 2D matrix containing the calculated dose at 2 cm depth was extracted from the "3D dose file". Next, an image file (TIF) was created representing a reference planar dose as input for Film QA analysis. The measured absolute dose was obtained by exposing EBT2 film at depth of 2 cm in a same heterogeneous phantom (4x4x4 cm^3) in three different gantry angles at 225 kVp, 13 mAs for one minute irradiator settings as shown in figure 4.17. The film was scanned using the EPSON 1000XL scanner and saved in TIF format. The scanned image was imported into Film QA software and converted to dose using a kV calibration curve. The absolute dose measured for three angles exposed equal time is 7.62 Gy

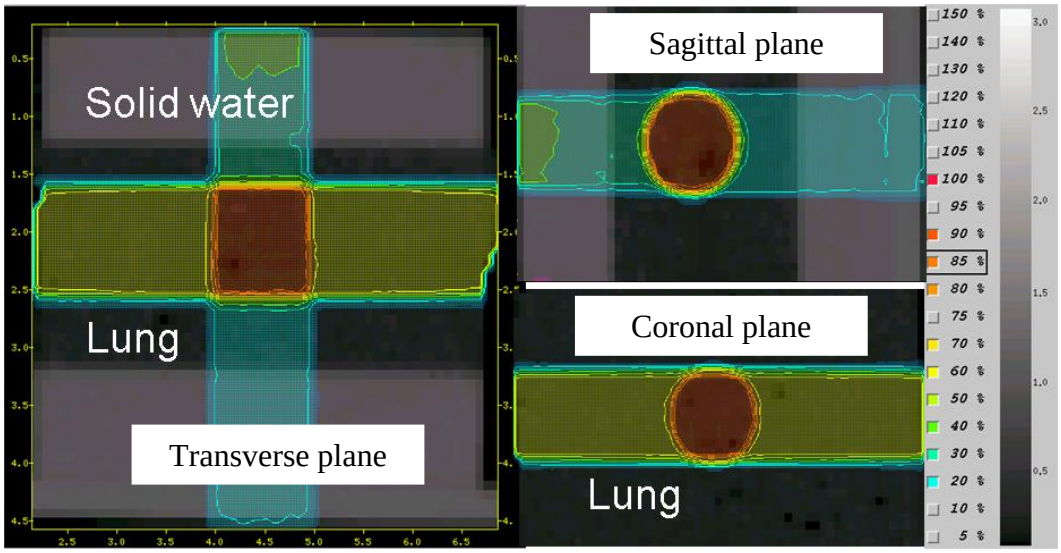

Figure 4.17: DOSXYZ CBCT heterogeneous solid water and lung phantom (4x4x4cm^3). Each dose point in 3D phantom is normalized to dose at the isocenter. Dose uncertainty for each point in simulation is 0.5 to 3.0 % with maximum uncertainty toward distal end of the phantom.

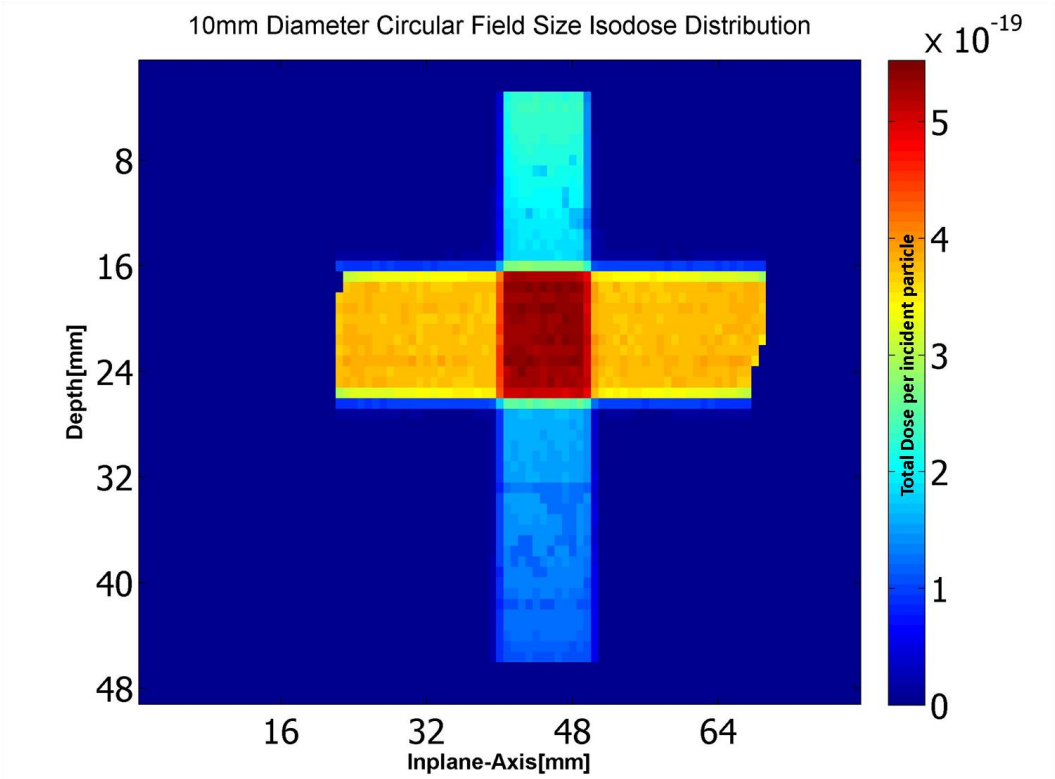

Figure 4.18: Isodose distributions for 10 mm diameter circular field in heterogeneous medium of solid water and lung ($4x4x4cm^3$) with multiple beams.

The absolute dose rate at the isocenter is calculated from the dose distribution using equation 4.6

$$\dot{D}_d = k(\frac{IP}{\min}) * D_{MC_d}(\frac{Gy}{IP})$$
$$= 0.4578 * 10^{19}(\frac{IP}{\min}) * 5.49 * 10^{-19}(\frac{Gy}{IP}) = 2.508(\text{Gy/min}) \quad (4.21)$$

The absolute dose from Monte Carlo at the isocenter is calculated from the MC dose distribution using equation 4.21

$$D_d = k(\frac{IP}{\min}) * D_{MC_d}(\frac{Gy}{IP}) * 3(\min)$$
$$= 0.457 * 10^{19}(IP/\min) * 5.49 * 10^{-19}(Gy/\min) * 3\min = 7.539(\text{Gy}) \quad (4.22)$$

The absolute dose difference between simulation and measurement is -1.07%

4.6 Conclusion

This study has investigated the feasibility of using the virtual source (phase space source from MC) in a CBCT data from the XRAD 225Cx irradiator. Various MATLAB scripts were written to streamline the conversion of CBCT numbers to physical densities. The MC dose calculation in CBCT data was validated in a homogenous medium. The comparison between MC and measured dose distributions was quantitatively validated using the gamma index method for 10 mm field sizes in CBCT data based homogenous medium. The MC dose calculation in small animal was also demonstrated. A relation was formed between the Monte Carlo dose distributions and irradiation absolute dose rate. The irradiation time was calculated based on the Monte Carlo dose distribution in homogenous medium. This was demonstrated for single and multiple beams and compared with hand calculations for homogenous medium. Finally Monte Carlo calculated absolute dose and measured absolute dose in heterogeneous medium are in good agreement.

Monte Carlo is the most robust dose calculation method, which has great significance for future development of any commercial treatment planning for small animal irradiator. The irradiator has already become an essential tool for scientists at UT Southwestern in conducting a broad spectrum of preclinical studies. Animal irradiation systems facilitate scientific testing of biomedical hypotheses in vitro (cell) and in vivo (live animals) with the ultimate aim of promoting translational research and providing novel protocols for human cancer treatments. A small animal irradiator system is an essential element for quantitative molecular-imaging studies and radiobiological experiments of tumor and healthy tissue response to radiation.

References

DEMARCO, J. 1997. A CT-based Monte Carlo dosimetry tool for radiotherapy treatment planning and analysis. University of California, Los Angeles.

DEMARCO, J. J., SOLBERG, T. D. & SMATHERS, J. B. 1998. A CT-based Monte Carlo simulation tool for dosimetry planning and analysis. Med Phys, 25**,** 1-11.

ICRP 1975. Report of the Task Group on Reference Man. International Commission on Radiological Protection. Oxford, Pergamon, 23.

ICRU. 1989. Tissue Substitutes in Radiation Dosimetry and Measurement. International Commission on Radiation Units and Measurements, Bethesda, MD, 44.

SPEISER, M. 2010. Development and Validation of a Virtual Monte Carlo Radiotherapy Source Model and Characterization of the Influence of Heterogeneities on Dose Calculation Accuracy. PhD Dissertation, UCLA.

WALTER, R. N. & HIDEO, H. 1995. PEGS4 User Manual.

WALTERS, B., KAWRAKOW, I. & ROGERS, D. W. O. 1996. DOSXYZ users manual. NRCC Report No. PIRS-0509B.

APPENDIX A

Absolute Calibration: In-phantom method

TG-61 protocol for kilovoltage X-ray beam dosimetry

UT SOUTHWESTERN MEDICAL CENTER AT DALLAS

In Water Calibration: Calculating Dose to Water at 2 cm Depth

Performed by:	R. Pidikiti S.Stojadinovic	Date & Time:	12-Jul-2012

1. Instrumentation

X-ray Unit Model	X-RAD 225	Electrometer Model		Keithley MK614EBS
Serial Number	1103-1747	Serial Number		688064
		Electrometer Scale		1.0E-08
		Elect. Corr. Factor	P_{elec} =	0.985 C/scale
		Date of report		10-May-12
Chamber Model				PTW N31010
Serial Number				4284
Exposure Calibration Coefficient, N_X			N_X =	3.140E+10 R/C
Air Kerma Calibration Coefficient, N_K [Gy/C] = 8.76·10^{-3} [Gy/R]·N_X [R/C]			N_K =	2.751E+08 Gy/C
Date of report (not to exceed 2 years)				1-Jul-11

3. Measurement Conditions:

Distance	SAD =	30.5	cm	Tube Potential	kVp =	225 kV
Field radius	r =	2.2	cm	Tube (mA)x(s)	(mA)x(s) =	13 mAs
Field Size, $FS=r^2\pi$	FS =	15.9	cm^2	Added Filtration	F =	0.3 mm Cu
Half Value Layer	HVL =	1.00	mm Cu	Exposure Time	t =	1.0 min

4. Temperature/Pressure Correction

Temperature, T [°C]	T =	23.0 °C
Pressure, P [mmHg]	P =	747.9 mmHg
P_{TP} [Eq.(8)]: $P_{TP}=[(273.2+T)/295.2]\cdot[760/P]$	P_{TP} =	1.0196

5. Polarity Correction

Readings	Rdg 1	Rdg 2	Rdg 3	Voltage
M^+_{raw}	0.867	0.869	0.868	[+300 V]
M^-_{raw}	0.863	0.863	0.863	[–300 V]

M_{raw} [C or rdg] for polarity of calibration

P_{pol} [Eq.(6)]: $P_{pol}=|(M^+_{raw}-M^-_{raw})/2M_{raw}|$

M^+_{raw} =	0.868	·10^{-8}C
M^-_{raw} =	0.863	·10^{-8}C
M_{raw} =	0.863	·10^{-8}C
P_{pol} =	1.003	

6. P_{Ion} Correction for Continuous Beams

Operating Voltage, V_H ‖ Lower Voltage, V_L

Readings	Rdg 1	Rdg 2	Rdg 3	Voltage
M^H_{raw}	0.863	0.863	0.863	[–300 V]
M^L_{raw}	0.864	0.863	0.863	[–150 V]

P_{Ion} [Eq.(5)]: $P_{Ion}=\{[1-(V_H/V_L)^2] / [M^H_{raw}/M^L_{raw}-(V_H/V_L)^2]\}$

V_H =	-300	V
V_L =	-150	V
M^H_{raw} =	0.863	·10^{-8}C
M^L_{raw} =	0.863	·10^{-8}C
P_{Ion} =	1.000	

7. Fully Corrected Ion Chamber Reading $M=M_{raw}\cdot P_{elec}\cdot P_{TP}\cdot P_{pol}\cdot P_{Ion}$

M = 0.869 ·10^{-8}C

8. End Effect, δt [Attix Eq.(13.23)]

Readings	Rdg 1	Rdg 2	Rdg 3	Voltage
$\Delta\tau_1$	0.863	0.863	0.863	[–300 V]
$\Delta\tau_2$	0.428	0.428	0.428	[–300 V]

δt [Eq.(7)]: $\delta t = (M_2\Delta\tau_1-M_1\Delta\tau_2) / (M_2-M_1)$

$\Delta\tau_1$ =	1.0	min
$\Delta\tau_2$ =	0.5	min
M_1 =	0.863	·10^{-8}C
M_2 =	0.428	·10^{-8}C
δt =	0.009	min

9. Chamber Correction Factor, $P_{Q,chamber}$ (Table VIII, Fig. 4)	$P_{Q,chamber}$ =	1.023
10. Sheath Correction Factor, P_{sheath} (Table IX)	P_{sheath} =	1.000
11. In-water Mass Energy Absorption Coefficient Ratio (Table VII, Fig. 3)	$(\mu_{en}/\rho)^w_{air}$ =	1.065
12. Dose to 2cm Water: $D_W = M\cdot N_K\cdot P_{Q,chamber}\cdot P_{sheath}\cdot[(\mu_{en}/\rho)^w_{air}]_{water}$	D_W(2cm) =	2.606 Gy
Dose to Water @ Phantom Surface: $D_W(0cm) = D_W(2cm)/PDD(2cm)$	D_W(0cm) =	3.391 Gy
13. Dose Rate $D_W/dt = D_W/(t-\delta t)$	D_W(0cm)/dt=	3.420 Gy/min

Absolute Calibration: In-air method

TG-61 protocol for kilovoltage X-ray beam dosimetry

UT SOUTHWESTERN MEDICAL CENTER AT DALLAS

In Air Calibration: Calculating Dose to Water on the Phantom Surface

Performed by:	R. Pidikiti S.Stojadinovic	Date & Time:	12-Jul-2012

1. Instrumentation

X-ray Unit Model	X-RAD 225Cx	Electrometer Model		Keithley MK614EBS	
Serial Number	1103-1747	Serial Number		688064	
		Electrometer Scale		1.0E-08	
		Elect. Corr. Factor	P_{eleo} =	0.985	C/scale
		Date of report		10-May-12	
Chamber Model				PTW N31010	
Serial Number				4284	
Exposure Calibration Coefficient, N_X			N_X =	3.140E+10	R/C
Air Kerma Calibration Coefficient, N_K [Gy/C] = $8.76 \cdot 10^{-3}$ [Gy/R]·N_X [R/C]			N_K =	2.751E+08	Gy/C
Date of report (not to exceed 2 years)				1-Jul-11	

3. Measurement Conditions:

Distance	SAD =	30.5	cm	Tube Potential	kVp =	225	kV
Field radius	r =	2.25	cm	Tube (mA)x(s)	(mA)x(s) =	13	mAs
Field Size, $FS=r^2\pi$	FS =	15.9	cm^2	Added Filtration	F =	0.3	mm Cu
Half Value Layer	HVL =	1.00	mm Cu	Exposure Time	t =	1.0	min

4. Temperature/Pressure Correction

Temperature, T [°C]	T =	24.4	°C
Pressure, P [mmHg]	P =	747.9	mmHg
P_{TP} [Eq.(8)]: $P_{TP}=[(273.2+T)/295.2]\cdot[760/P]$	P_{TP} =	1.0244	

5. Polarity Correction

Readings	Rdg 1	Rdg 2	Rdg 3	Voltage
M^+_{raw}	0.947	0.947	0.946	[+300 V]
M^-_{raw}	0.949	0.949	0.948	[–300 V]

M_{raw} [C or rdg] for polarity of calibration

P_{pol} [Eq.(6)]: $P_{pol}=|(M^+_{raw}-M^-_{raw})/2M_{raw}|$

M^+_{raw} =	0.947	$\cdot 10^{-8}$C
M^-_{raw} =	0.949	$\cdot 10^{-8}$C
M_{raw} =	0.949	$\cdot 10^{-8}$C
P_{pol} =	0.9990	

6. P_{Ion} Correction for Continuous Beams

Operating Voltage, V_H ‖ Lower Voltage, V_L

Readings	Rdg 1	Rdg 2	Rdg 3	Voltage
M^H_{raw}	0.949	0.949	0.948	[–300 V]
M^L_{raw}	0.950	0.947	0.946	[–150 V]

P_{Ion} [Eq.(5)]: $P_{Ion}=\{[1-(V_H/V_L)^2] / [M^H_{raw}/M^L_{raw} - (V_H/V_L)^2]\}$

V_H =	-300	V
V_L =	-150	V
M^H_{raw} =	0.949	$\cdot 10^{-8}$C
M^L_{raw} =	0.947	$\cdot 10^{-8}$C
P_{Ion} =	1.0004	

7. Fully Corrected Ion Chamber Reading $M=M_{raw}\cdot P_{eleo}\cdot P_{TP}\cdot P_{pol}\cdot P_{Ion}$: M = 0.957 $\cdot 10^{-8}$C

8. End Effect, δt [Attix Eq.(13.23)]

Readings	Rdg 1	Rdg 2	Rdg 3	Voltage
$\Delta\tau_1$	0.949	0.949	0.948	[–300 V]
$\Delta\tau_2$	0.468	0.468	0.468	[–300 V]

δt [Eq.(7)]: $\delta t = (M_2\Delta\tau_1 - M_1\Delta\tau_2) / (M_2 - M_1)$

$\Delta\tau_1$ =	1.0	min
$\Delta\tau_2$ =	0.5	min
M_1 =	0.949	$\cdot 10^{-8}$C
M_2 =	0.468	$\cdot 10^{-8}$C
δt =	0.013	min

9. Backscatter Factor, B_W (Table V or Table VI)	B_W =	1.2070
10. Stem Correction in Air, $P_{stem,air}$ (Section V.7)	$P_{stem,air}$ =	1.0000
11. In-air Mass Energy Absorption Coefficient Ratio (Table IV)	$(\mu_{en}/\rho)^w_{air}$ =	1.0730
12. Dose to Water $D_W = M\cdot N_K\cdot B_W\cdot P_{stem,air}\cdot[(\mu_{en}/\rho)^w_{air}]_{air}$	D_W =	3.408 Gy
13. Dose Rate $D_W/dt = Dw/(t\text{-}dt)$	$\check{D}_W$ =	3.454 Gy/min